LEVEL II

A STUDY OF TROPOSPHERIC REFRACTIVE INDEX, TEMPERATURE, HUMIDITY, AND VELOCITY FIELDS USING ELECTRO-MAGNETIC AND ACOUSTIC WAVE PROPAGATION METHODS SUPPORTED BY IN SITU MEASUREMENTS

BY

A G KJELAAS

NDRE REPORT No 67

78 10 16 005

6

A STUDY OF TROPOSPHERIC REFRACTIVE INDEX, TEMPERATURE, HUMIDITY, AND VELOCITY FIELDS USING ELECTROMAGNETIC AND ACOUSTIC WAVE PROPAGATION METHODS SUPPORTED BY IN SITU MEASUREMENTS,

10 av
A. G. Kjelaas

11 Oct 74

12 89 p.

14 NDRE ~~REPORT No~~ 67

D D C

RECEIVED

OCT 27 1978

B

142 120

78 10 16 095

PREFACE

The present work comprises three previously published papers and three papers which have been submitted and accepted for publication.

(1)	Kjelaas, A G	— Tropospheric structure deduced from electromagnetic and acoustic wave propagation experiments. *Submitted to Geophysica Norwegica.*
(2)	Kjelaas, A G G R Ochs	— Study of divergence in the boundary-layer using optical propagation techniques, J Appl Meteorol 13, 2, 242–8 (1974)
(3)	Kjelaas, A G E E Gossard J M Young W R Moninger	— Dispersion and spectra of gravity waves probably generated by a convective storm, Tellus 27, 1 (1975). *In press*
(4)	Kjelaas, A G D W Beran W H Hook B R Bean	— Observation of waves in the boundary-layer using an array of acoustic sounders, J Atmos Sci. *In press*
(5)	Gjessing, D T A G Kjelaas J Nordø	— Spectral measurements and atmospheric stability, J Atmos Sci 26, 3, 462–7 (1969)
(6)	Gjessing, D T A G Kjelaas E Golton	— Small-scale atmospheric structure deduced from measurements of temperature, humidity and refractive index, Boundary-Layer Meteorol 4, 475–92 (1973)

Paper 1 summarizes the potentials of different electromagnetic and acoustic wave propagation experiments as diagnostic tools in the study of the refractive-index, temperature, humidity and velocity fields in the troposphere.

Papers 2 and 3 discuss measurements of horizontal wind velocity using optical line-of-sight propagation techniques. Paper 2 deals with measurements of horizontal divergence while in Paper 3 the spectrum of the spatial wind together with the spectrum of air-pressure are used to deduce the propagation speed and direction of progressive gravity waves in the troposphere.

Paper 4 deals with the potentials of an array of vertically pointing acoustic echo sounders to study time-dependent structures, especially waves, in the boundary layer.

In Paper 5 a forward scatter technique (beam-swinging) is used to deduce the vertical spectra of refractive index and air velocity. The influence of atmospheric stability on these spectra is discussed.

Paper 6 discusses the spatial structure of refractive index, temperature and humidity in the lowest 2000 m of the troposphere as deduced from tethered balloon measurements.

With the exception of the work described in Papers 2, 3 and 4, the work has been carried out at the Norwegian Defence Research Establishment.

The work which is the basis for Papers 2, 3 and 4 was carried out during a stay as a visiting scientist at the Wave Propagation Laboratory, National Oceanic and Atmospheric Administration, Boulder, Colorado, and was sponsored by the Royal Norwegian Council for Scientific and Industrial Research.

GENERAL INTRODUCTION

The density both in time and space of our present meteorological observations are fairly well matched to the synoptic scale weather pattern.

For the study of micro- and meso-scale phenomena it is evident that we cannot rely upon ground-based in situ measurements and twice daily radiosondes.

As it is neither technologically nor economically feasible to achieve the desired resolution in time and space by conventional observation techniques, further advances in our knowledge about the atmosphere at micro- and meso-scales are strongly dependent on the development and application of new measuring techniques.

This requirement for better and more reliable measurements has led to great activity in the application of different remote sensing techniques which are based on the interaction between electromagnetic or acoustic waves and refractive index fluctuations in the troposphere.

The progress made by radio communication scientists in understanding the influence of atmospheric refractive index inhomogeneities on the scattering of radiowaves, has shown that radio tropospheric scatter techniques can provide important information about the fine-scale structure of the troposphere.

Highly sensitive radars, mainly developed for military purposes, have proved to be extremely valuable tools in the study of both atmospheric stratification and convection.

Based on the experience from line-of-sight communication, a variety of optical and microwave methods have been suggested for measuring winds and refractive index structures in the boundary layer.

More recently it has also been demonstrated that acoustic echo sounding can be a valuable tool both in the study of wind in the troposphere and for monitoring temperature inversion structures and convection.

The present work describes different applications of line-of-sight optical and micro wave propagation, Doppler radars, forward scatter, and acoustic echo sounding in the study of the tropospheric refractive index, temperature, humidity and velocity fields.

It is shown that carefully designed experiments involving different kinds of electromagnetic and acoustic wave propagation can give reliable and very useful information regarding the structure of the troposphere.

CONTENTS

TROPOSPHERIC STRUCTURE DEDUCED FROM ELECTROMAGNETIC AND ACOUSTIC WAVE PROPAGATION EXPERIMENTS

SUMMARY

This paper reviews briefly the potentials of the atmospheric remote sensing techniques where the refractive index inhomogenities play the dominant role in producing fluctuations in the received signal. The techniques discussed are optical and microwave line-of-sight propagation, acoustic echo sounding, and microwave back- and forward scattering.

Methods for measurements of variability of wind, temperature and water vapour are discussed and emphasis is laid on methods which have been proven through field experiments.

The theories of line-of-sight propagation and scattering are also reviewed briefly.

1 INTRODUCTION

Further advances in our knowledge about the atmosphere are strongly dependent on the development and application of new measuring techniques. The shortcomings of point measurements and radiosondes have become more and more evident.

For this reason there has been a rapid development of a series of new techniques during the last decade. The common feature of one group of these techniques is that they transmit an electromagnetic or acoustic wave, which interacts with the atmosphere. A portion of this energy is scattered and detected at the receiver. Information about the atmosphere is then derived from the characteristics of the received signal. The advantages of such a measuring technique are many (Little, 1973):

-- The measuring system does not significantly modify (or interfere with) the medium being measured

-- The measurements are taken remotely, i e no (in situ) instrumentation has to be brought to the region of the atmosphere to be measured

-- The relevant atmospheric parameters are measured in one, two or three dimensions, mostly with excellent resolution in both time and space

Further, this type of measurement may provide the following information about the atmospheric structure:

a) line integral — the integrated value of a parameter along a line through the atmosphere

b) line average — the average value of the parameter along some line of known length

c) line profile — the distribution of the parameter along some line of known length

d) 2-dimensional coverage — the distribution of the parameter over a plane

e) 3-dimensional coverage — the distribution of the parameter in space

f) spectrum — the spatial power spectrum of a parameter

g) flux — the rate at which mass, momentum or heat is transported

The success of the measuring technique is dependent on the strength and type of the interaction of the wave with the atmosphere. We may distinguish between:

a) a spectroscopic interaction, in which the radiation reacts with the molecules, i e an absorption and reradiation

b) a refractive index interaction, where the scattering of the incident wave is caused by inhomogenities in the refractive index field, or, more specifically, the three-dimensional spectrum of refractive index fluctuations

For this short report we shall only consider measuring techniques in which refractive index inhomogenities play the dominant role. The discussion is also narrowed to "sensors" which are located on or near the ground.

The techniques discussed are line-of-sight optical and microwave propagation, acoustic echo sounding, pulse Doppler and FM—CW radars, and forward scatter.

Scattering usually implies that no signal will be received in the absence of refractive index inhomogenities, while in the case of line-of-sight propagation the field at any point will be the sum of the direct wave and the many scattered waves, scattered and refracted by local variations in the refractive index field.

Each technique is discussed separately and emphasis is laid on capabilities which have been demonstrated through field experiments.

2   THE THEORETICAL BACKGROUND

In this section we shall derive the necessary equations governing EM and acoustic wave propagation in the atmosphere.

2.1   Refractivity and refractive index

The radio refractivity N for air is given in terms of refractive index n as

$$N = (n-1) \cdot 10^6 = \frac{77.6}{T} (p + 4810 \frac{e}{T}) \qquad (2.1)$$

where

T — temperature in degrees Kelvin

p — total pressure in mb

e — partial water vapour pressure in mb

For acoustic waves the refractivity N_a is given by

$$N_a = (n_a - 1) \cdot 10^6 \approx 10^6 \left[\frac{T_o - T}{2T_o} - 0.14 \frac{e}{p} - \frac{V \cos\phi}{c_o} \right] \qquad (2.2)$$

where

$c_o = 20.5 \, T_o^{1/2}$ is a reference sound velocity at a reference temperature T_o

ϕ — angle between the wave and wind vector

V — wind speed

The optical refractive index n_o can be written as

$$N_o = (n_o-1)10^6 \sim 79 \frac{P}{T} \tag{2.3}$$

MAGNITUDE CHANGES	CHANGES IN REFRACTIVITY IN N-UNITS		
	RADIO	OPTICAL	ACOUSTIC
$\Delta T = 1\ K$	1	1	$1.7 \cdot 10^3$
$\Delta V = 1\ ms^{-1}$	–	–	$3 \cdot 10^3$
$\Delta e = 1\ mb$	4	$4 \cdot 10^{-2}$	$1.4 \cdot 10^2$

Table 2.1   *Relative values of C_n for acoustic radio and optical waves*

The influence of small changes in the atmospheric parameters on the different refractive indexes is shown in Table 2.1. Thus, for example, acoustic waves are more than three orders of magnitude more sensitive to changes in temperature than either radio or optical waves. While acoustic waves are sensitive to wind fluctuations, the refractive index for electromagnetic, including optical, waves is independent of wind.

The refractive index can be decomposed into a mean $\bar{n}$ plus a fluctuating component n_1 as

$$n(\vec{r}) = \overline{n(\vec{r})} + n_1(\vec{r}) \tag{2.4}$$

Often it is very useful to represent the fluctuating component in terms of a covariance function and its associated spectrum or in terms of a stochastic Fourier–Stieltjes integral.

The covariance function is defined as

$$C(\vec{r}) = \overline{n_1(\vec{r}_1)\, n_1(\vec{r}_1 + \vec{r})} \tag{2.5}$$

and its associated spectrum as

$$\Phi_n(\vec{K}) = \frac{1}{(2\pi)^3} \iiint_{-\infty}^{\infty} C(\vec{r}) \exp(-i\vec{K}\cdot\vec{r}) d\vec{r} \tag{2.6}$$

In terms of a stochastic Fourier–Stieltjes integral, $n_1(\vec{r})$ can be represented as

$$n_1(\vec{r}) = \iiint_{-\infty}^{\infty} A(\vec{K}) \exp(i\vec{K}\cdot\vec{r}) d\vec{K} \tag{2.7}$$

and the spectrum $\Phi_n(K)$ can be obtained by evaluating $A(\vec{K})A^*(\vec{K})$, where the asterisk denotes the complex conjugate.

2.2 Propagation of radio and optical waves

We consider a medium where the refractive index is expressed by equation (2.4).

The propagation of an electromagnetic wave in this medium is governed mathematically by Maxwell's equations, which can be combined to give the vector wave equation

$$\nabla^2 \vec{E} + k^2 n^2(\vec{r})\vec{E} + 2\nabla\, \vec{E}\cdot\nabla(n(\vec{r})) = 0 \tag{2.8}$$

where it is assumed that the electric field $\vec{E}$ is sinusoidal, and k is the wavenumber.

The last term in Equation (2.8) describes the polarization of the field. If the scattered depolarized field is much smaller than the field in the original direction of polarization, Equation (2.8) reduces to the scalar wave equation

$$\nabla^2 E + k^2 n^2(r)\, E = 0 \tag{2.9}$$

Different approaches have been used to obtain an approximate solution of this equation when the medium is weakly inhomogeneous:

— Geometrical or ray optics

— Method of small perturbations or the first Born approximation

— Method of smooth or slowly varying perturbations (the Rytov method)

For details, the reader is referred to Strohbehn (1968).

In the case of large perturbations, techniques for solving the equation have not yet been satisfactorily developed.

2.2.1 Scattering of electromagnetic waves

Consider a volume element $d^3\vec{r}$ within a scatter volume V filled with a random medium with a refractive index as defined in Equation (2.4). If illuminated by an incident field E_o the element becomes polarized, giving rise to a dipole moment $d\vec{P} = n_1 E_o d^3 r$. At a distance R the dipole moment results in a polarization potential. If $R \gg V^{1/3}$ the scattered field E_S resulting from all the elementary scattering elements can be expressed as

$$E_S = \frac{k_s^2 E_o}{4\pi R}\, A(\vec{K}) \tag{2.10}$$

where $\vec{k}_o$ and $\vec{k}_s$ are the incident and scattered wave vectors, $\vec{K} = \vec{k}_o - \vec{k}_s$.

$A(K)$ is obtained from the inverse transform of Equation (2.7).

$k = |\vec{k}_o| = |\vec{k}_s| = 2\pi/\lambda$, where λ is the wavelength.

R is the distance from the scattering volume to the observation point at which the field is equal to E_S. Figure 2.1 shows the scattering geometry.
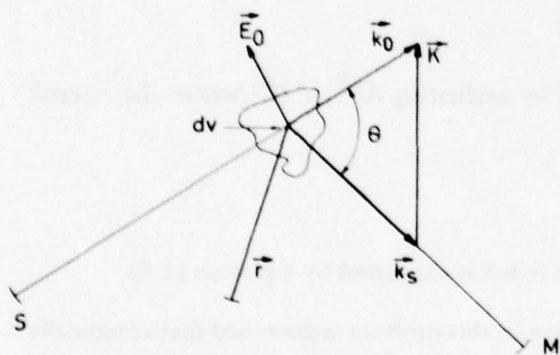
Figure 2.1 Scatter geometry

The magnitude of the scattering vector $\vec{K} = \vec{k}_o - \vec{k}_s$ is

$$K = 2k \sin\frac{\theta}{2} \tag{2.11}$$

where θ is the angle between $\vec{k}_o$ and $\vec{k}_s$, i e the scattering angle.

The scattering cross-section σ which is a measure of the fraction of the incident power scattered in a given direction, can be obtained by evaluating $E_S \cdot E_S^*$ (Gjessing, 1962). In terms of the refractive index fluctuations the following expression of the scattering cross-section can be given

$$\sigma = 2\pi k^4 \sin^2\chi\Phi_n(K) \tag{2.12}$$

where χ — polarization angle

          $\Phi_n(K)$ — three-dimensional power spectrum of the refractive index fluctuations n_1

From Equation (2.12) we observe that the intensity of the scattered wave for a given geometry and a given wavelength is determined by one spectral component in the three-dimensional refractive index spectrum, corresponding to a scale ℓ of

$$\ell = \frac{2\pi}{K} = \frac{\lambda}{\sin\frac{\theta}{2}} \tag{2.13}$$

which is Bragg's condition for diffraction from a spatial structure.

For pure backscatter ($\theta = 180°$) the intensity of the scattering is determined by the refractive index inhomogenities of a scale size corresponding to $\lambda/2$.

2.2.2 Line-of-sight propagation, radio and optical

The scalar wave equation can be solved by one of the techniques listed in section 2.2. Instead of using one of these approaches, we will apply a method described by Lee and Harp (1969). This method, which is based on phase screens, leads to an easier physical understanding of the problem than do the more mathematical approaches.

In line-of-sight propagation it is useful to decompose the refractive index field n_1 into a plane normal to the propagation direction z, expressed in terms of a two-dimensional stochastic Fourier—Stieltjes integral, i e

$$n_1(x,y,z) = \int\int_{-\infty}^{\infty} \exp(i\vec{K}\cdot\vec{\rho})\, \nu(z,\vec{K})d^2K \tag{2.14}$$

where $\vec{\rho}$ is a position vector in this plane, $\vec{\rho}=(x,y)$ and $\vec{K}=(K_x,K_y)$. $\nu(z,\vec{K})$ is the Fourier component in the same plane.

This Fourier component will cause a small phase change in the incident wave as it passes through the plane. This phase perturbation produces perturbation in the phase of the received field. The field in the receiver plane due to all the Fourier components of the refractive index and all of the layers of thickness dz between transmitter and receiver is then for a spherical wave (Lee and Harp, 1969)

$$E = 1-ik \int_0^L dz \int\int_{-\infty}^{\infty} \nu(z,\vec{K}) \exp[i\frac{K^2z(L-z)}{2kL}]\cos(\vec{K}\cdot\vec{\rho}\frac{z}{L})d^2K \tag{2.15}$$

where L is the length of the path.

Assuming $E = A \exp(iS)$ where $A = 1+A_1$ and $S = kL+S_1$ we can express the amplitude and phase fluctuations in the receiving plane in terms of spatial covariance functions as defined in Equation (2.5).

The spatial covariance functions can also be derived by evaluating $\overline{A_1 A_1^*}$ and $\overline{S_1 S_1^*}$ (Tatarski, 1961).

Assuming that the refractive fluctuations are statistically homogeneous, the two-dimensional spectrum $F(z,\vec{K})$ of the refractive index field can be obtained by evaluating $\nu(z,\vec{K})\, \nu^*(z,\vec{K})$.

For the case of isotropy, the two-dimensional spectrum is related to the covariance function as

$$F(z,K) = \frac{1}{2\pi} \int_0^\infty C(z,\rho) \, J_0(K\rho)\rho d\rho \tag{2.16}$$

where J_0 is a Bessel function of zero order.

Assuming isotropy, the spatial covariance function of amplitude and phase can then be expressed in terms of the three-dimensional refractive index spectrum as

$$C_s(\rho) = 4\pi^2 k^2 \int_0^L \int_0^\infty K \Phi_n(K) \cos\left[\frac{K^2 z(L-z)}{2kL}\right] J_0\left(\frac{K\rho z}{L}\right) dK dz \tag{2.17}$$

$$C_a(\rho) = 4\pi^2 k^2 \int_0^L \int_0^\infty K \Phi_n(K) \sin\left[\frac{K^2 z(L-z)}{2kL}\right] J_0\left(\frac{K\rho z}{L}\right) dK dz \tag{2.18}$$

If the refractive index fluctuations are homogeneous over the path, the integration over z may be carried out.

Under the assumption of Taylor's hypothesis, the temporal power spectrum of the phase and amplitude fluctuations can be obtained by substituting into Equations (2.17) and (2.18) $\rho = v_x\tau$, where v_x is the cross-wind component, and taking the Fourier transform of $C_s(v_x\tau)$ and $C_a(v_x\tau)$. τ is the time.

2.3 Propagation of acoustic waves

Similar to the discussion of propagation of radio and optical waves, we consider a turbulent medium where the refractive index is composed of a mean, $\bar{n}_a$, plus a fluctuating component n_{a_1}

$$n_a = \bar{n}_a + n_{a_1} \tag{2.19}$$

where the fluctuating part n_{a_1} may be written as

$$n_{a_1} = -\frac{u_1}{c_0} - \frac{1}{2}\frac{T_1}{T_0} \tag{2.20}$$

when $\quad |n_{a_1}| \ll |\bar{n}_a|$

where c_0 is the velocity of sound, corresponding to the average temperature T_0. T_1 is the temperature fluctuation from this average value and u_1 is the perturbation velocity of zero mean.

The propagation of sound in this medium is described by the equations of hydrodynamics, from which a perturbated Helmholtz equation analogous to Equation (2.8) (Clifford and Brown, 1970; Monin, 1962) can be written as

$$\nabla^2 P_s + k^2 P_s + 2k^2 n_{a_1} P_0 - 2ikP_0 \frac{\delta n_{a_1}}{\delta z} = 0 \tag{2.21}$$

where $\quad P_s \quad$ – scattered acoustic field (acoustic pressure)

$P_0 = A_0 e^{ikz}$ – incident field

The fourth term in Equation (2.21) is analogous to the polarization term in EM propagation.

While the polarization term was very small in the EM case, it has to be included in acoustic propagation since the acoustic wave is essentially longitudinally polarized and accordingly will be affected by wave motion parallel to gradients of refractivity.

2.3.1 Scattering of acoustic waves

The scattering of sound waves in a turbulent medium is analogous to scattering of electromagnetic waves. The scattered acoustic field P_s can be expressed in terms of the three-dimensional Fourier transform of the refractive index as

$$P_s = \frac{k_s^2 P_o}{2\pi r} \int_v [n_{a_1}(r) - \frac{i}{k} \frac{\delta n_{a_1}}{\delta z}] e^{i\vec{K}\cdot\vec{r}} d^3\vec{r} \qquad (2.22)$$

The scattering cross-section is found analogously to the EM case by evaluating $P_s \cdot P_s^*$. In terms of the refractive index fluctuations the following expression of the scattering cross-section can be given (Tatarski, 1971)

$$\sigma_a = \frac{\pi}{2} k^2 \cos^2\theta \; [\frac{\Phi_T(K)}{T_o^2} + \frac{\cos^2\frac{\theta}{2}}{\pi} \frac{\Phi_V(K)}{c_o^2}] \qquad (2.23)$$

with the same definition of σ as in the EM case.

$\Phi_T(K)$ and $\Phi_V(K)$ are the three-dimensional power spectral densities of temperature and wind fluctuation, respectively. The expression for K is similar to the EM case, i e, $K = 2k \sin \theta/2$, where k is the wavenumber of the sound, and T_o is the temperature corresponding to the sound velocity c_o. From Equation (2.23) we see that the back-scatter ($\theta = 180°$) is produced by temperature inhomogenities since the factor $\cos^2 \theta/2$ is zero. For forward scatter we have contributions from both temperature fluctuations and turbulence. That the velocity fluctuations do not contribute to the backscatter, but only in the forward scatter case, is a direct consequence of the incompressibility of the turbulent flow.

2.4 Doppler techniques

For both EM and acoustic wave propagation, Doppler techniques can be used. With a scatter geometry as shown in Figure 2.1, the Doppler shift is given by

$$\Delta f = \frac{1}{2\pi} (\vec{k}_s - \vec{k}_o) \cdot \vec{V} \qquad (2.24)$$

or (Ottersten et al, 1973)

$$\Delta f \approx \frac{2}{\lambda} \sin \frac{\theta}{2} \cos\beta V$$

if we neglect the difference in wavelength between the incident and scattered wave.

The angle β is the angle between the wind vector $\vec{V}$ and dir $(\vec{k}_s - \vec{k}_o)$. In the case of backscatter ($\theta/2 = 90$), the Doppler shift is a measure of the radial velocity.

Since the obtained velocity is not observed at a point in space but over a volume, we will observe a Doppler spread or a Doppler spectrum due to fluctuations in the wind velocity throughout the volume and also from the fact that $\vec{k}_o - \vec{k}_s$ varies through the volume (for forward scatter). The first moment of this spectrum gives the average wind velocity, while the variance of the wind velocity can be derived from the second moment.

By scanning a radar in azimuth, several radial components of the wind can be obtained. This technique, which is called VAD (Velocity–Azimuth Display), was first proposed by Lhermitte and Atlas (1961). The geometry of the VAD technique is shown in Figure 2.2.

12

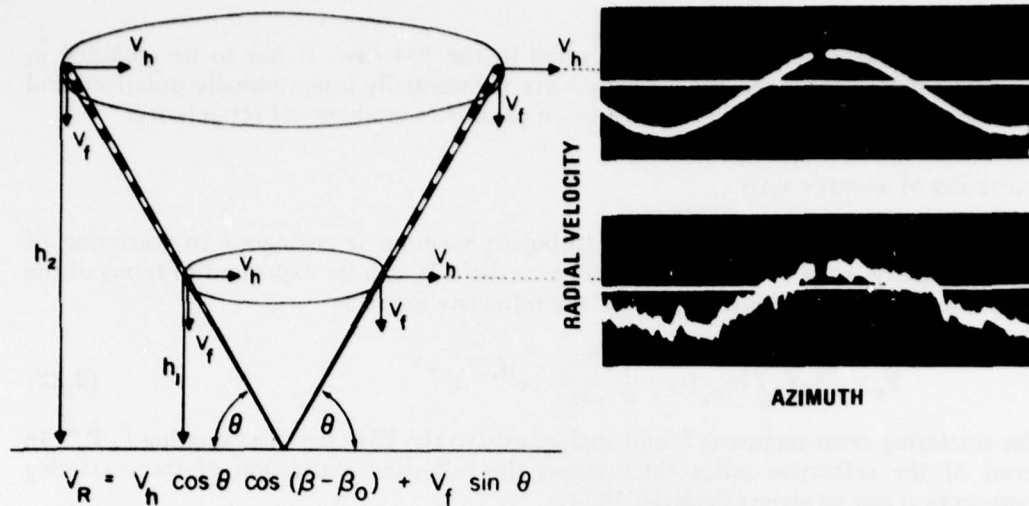$$V_R = V_h \cos\theta \cos(\beta-\beta_o) + V_f \sin\theta$$

Figure 2.2 Geometry of the VAD technique (from Lhermitte and Atlas, 1961)

The mean wind direction and speed as obtained from the VAD technique can be written as

$$V_R = V_H \cos(\beta-\beta_o) + V_f \sin\theta \qquad (2.25)$$

where

V_R — radial velocity

V_A — horizontal wind

θ — elevation of the scan

$V_f \sin\theta$ — DC component due to vertical wind

Browning and Wexler (1968) have shown that by expanding the radial velocity $V_R(a)$ as a function of azimuth in Fourier series

$$\overline{V}_k(a) = A_o + \sum_{k=1}^{2} (A_k \cos ka + B_k \sin ka) \qquad (2.26)$$

the Fourier coefficients are related to the mean wind components $\overline{u}_o$, $\overline{v}_o$, to the horizontal divergence $\partial\overline{u}/\partial x + \partial\overline{v}/\partial y$, to the stretching deformation $\partial\overline{u}/\partial x - \partial\overline{v}/\partial y$ and to the shearing deformation $\partial u/\partial y + \partial v/\partial x$ as

$$\overline{v}_o = A_1/\cos\theta$$

$$\overline{u}_o = B_1/\cos\theta$$

$$\frac{\partial\overline{u}}{\partial x} + \frac{\partial\overline{v}}{\partial y} = \frac{2}{R\cos^2\theta}(A_o - \overline{V}_f \sin\theta) \qquad (2.27)$$

$$\frac{\partial\overline{u}}{\partial x} - \frac{\partial\overline{v}}{\partial y} = -\frac{2A_2}{R\cos^2\theta}$$

$$\frac{\partial\overline{u}}{\partial y} + \frac{\partial\overline{v}}{\partial x} = \frac{2B_2}{R\cos^2\theta}$$

If we want to determine the three-dimensional wind, three radars at different locations observing the same volume of the air are needed.

Lhermitte and Miller (1971) have proposed a system where two Doppler radars are scanned in such a way that the two radar beams stay in the same plane during a given time interval. This method, which they called COPLAN-scanning, gives the two-dimensional wind in a horizontal plane.

2.5   Description of the atmosphere in terms of EM and acoustic wave propagation parameters

The influence of the atmosphere enters into the equation for scatter- and line-of-sight propagation of electromagnetic waves through the refractive index spectrum $\Phi_n(K)$ and the cross-path wind component v_x. For acoustic waves, the scattering is determined by the temperature spectrum $\Phi_T(K)$ and the turbulence spectrum $\Phi_V(K)$.

Assuming isotropy and incompressible turbulence, these spectra are usually expressed as (Tatarski, 1961)

$$\Phi_T(K) = 0.033 \, C_T^2 \, K^{-11/3} \tag{2.28a}$$

$$\Phi_n(K) = 0.033 \, C_n^2 \, K^{-11/3} \tag{2.28b}$$

$$\Phi_V(K) = 0.061 \, C_V^2 \, K^{-11/3} \tag{2.28c}$$

where C_T^2, C_n^2 and C_V^2 are the so-called structure constants for temperature, refractive index and wind, respectively.

The structure constants are a measure of the intensity of the fluctuations and they are defined by

$$C_T^2 = \overline{\left[\frac{T(x) - T(x+r)}{r^{1/3}} \right]^2} \tag{2.29a}$$

$$C_n^2 = \overline{\left[\frac{u(x) - u(x+r)}{r^{1/3}} \right]^2} \tag{2.29b}$$

and

$$C_V^2 = \overline{\left[\frac{u(x) - u(x+r)}{r^{1/3}} \right]^2} \tag{2.29c}$$

u is the wind speed and r is a distance measured along the x-axis. The x-axis may be chosen in any arbitrary direction to suit the experiment. The structure constant can also be expressed in terms of the energy dissipation ϵ as (Tatarski, 1961)

$$C_V^2 = a^2 \, \epsilon^{2/3} \tag{2.30}$$

where a is a constant. Equations (2.28a,b,c) are valid within some range of K which is called the inertial subrange. The inertial subrange is defined by an outer scale L_o and an inner scale ℓ_o, shown schematically in Figure 2.3.

INPUT RANGE   INERTIAL SUBRANGE

$\Phi(K) \sim K^{-11/3}$

$K_0 = 2\pi/L_0$

$L_0 \sim 1\text{–}100 \text{ m}$

$K_m = 2\pi/\ell_0$

$\ell_0 \sim \text{mm}$

DISSIPATION RANGE

$\Phi(K)$

K_0 K (m^{-1}) K_m
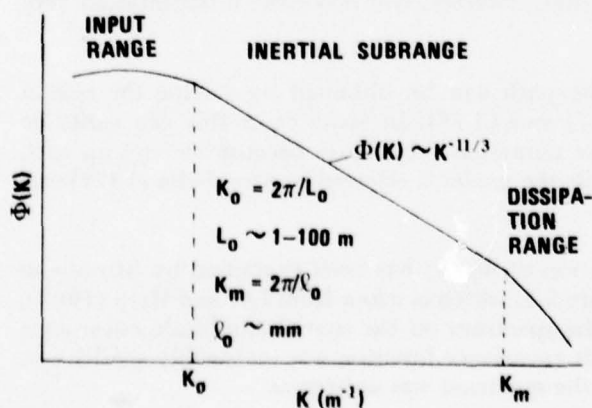
Figure 2.3 A schematic diagram of the inertial subrange

The inner scale ℓ_o which is where the dissipation starts, is in the atmosphere assumed to be of order mm, while the outer scale L_o which is the scale of energy input, is for isotropic turbulence assumed to be comparable with the height above ground, but very little information exists on the outer scale.

If the magnitude of the wave-number vector lies inside the inertial subrange, i e

$$\frac{2\pi}{L_o} < 2k \sin \frac{\theta}{2} < \frac{2\pi}{\ell_o}$$

then the expression for the different spectra given in Equation (2.28) can be substituted in the expressions describing the scatter and line-of-sight propagation.

3 THE POTENTIALS OF WAVE PROPAGATION EXPERIMENTS IN DERIVING INFORMATION ABOUT THE ATMOSPHERE

In the previous section we discussed briefly the theoretical framework for both EM and acoustic wave propagation. We observed that the atmospheric structures which enter the different propagation equations are:

— the refractive index spectrum $\Phi_n(K)$
— the temperature spectrum $\Phi_T(K)$, and
— the turbulence spectrum $\Phi_V(K)$, in addition to
— the cross beam component of mean wind velocity

In this section we shall discuss the diagnostic potentials of each of the techniques described in the previous section.

3.1 Line-of-sight propagation

We have shown that line-of-sight propagation is affected by the cross beam wind velocity and by the refractive index spectrum. These factors will now be discussed in some detail.

3.1.1 Determination of the refractive index spectrum $\Phi_n(K)$

The observed fluctuations in amplitude and phase of a radio wave or an optical wave over a line-of-sight path are determined by the refractive index spectrum.

The intensity of the refractive index fluctuations, C_n^2, averaged over the transmission path can be obtained by measuring the amplitude of the received signal. This line average of C_n^2 is a weighted average — weighted both along the path and in the wavenumber K. The amplitude fluctuations are most sensitive to scale sizes corresponding to the first Fresnel zone $\sim \sqrt{\lambda L}$. Phase fluctuations are sensitive to all scale sizes. But since most of the energy in the spectrum is associated with wavenumbers $K \approx 2\pi/L_o$, phase fluctuations are mostly determined by the outer scale.

A spatial distribution of C_n^2 along the path may be taken into consideration by assuming a series of step functions along the path (Harp, 1971). Any non-uniformity in the form of the refractive index spectrum, however, will make the interpretation very difficult.

The form of $\Phi_n(K)$ averaged over the path can be obtained by solving the spatial covariance function in Equations (2.17) and (2.18). In some cases this can easily be done, but in most cases we have to use numerical techniques because we end up with non-linear integral equations. For details the reader is referred to Strohbehn (1973) and Lee (1969).

The influence on line-of-sight propagation of $\Phi_n(K)$ has been examined by Strohbehn (1970) and Lee and Harp (1969). Figure 3.1, which is taken from Lee and Harp (1969), shows the influence of the form of the spectrum on the spatial amplitude covariance function. They found that the amplitude covariance function was reasonably sensitive to the exponent n (spectrum slope) when the spectrum was written as

$$\Phi_n(K) \sim K^{-n}$$

Any non-uniformity along the path of the refractive index spectrum will again complicate the picture and we may conclude that line-of-sight propagation is not specifically well suited for determining the refractive index spectrum.
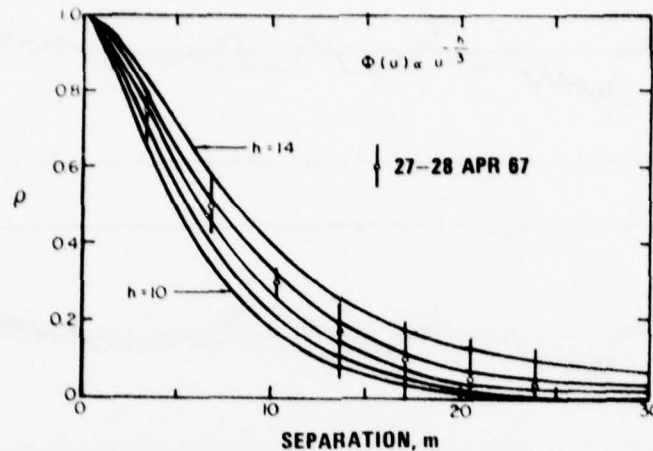

Figure 3.1   *Amplitude covariance functions for different spectra $\Phi(K)$ with experimental data ($L=28\ km$, $k=716\ m^{-1}$) (from Lee and Harp, 1969)*
Note that u means wavenumber.

3.1.2   Determination of wind speed from line-of-sight experiments

Contrary to the case of determining the refractive index spectrum, line-of-sight seems to be a very useful sensor in determining the average cross path wind speed.

Two different methods have been used:

a)   *The slope method* discussed by Shen (1970) and Lawrence et al (1972).
This method uses the slope at zero lag of the lagged cross-covariance function of the scintillation at two points in a receiving plane normal to the path as a measure of the wind speed across the path.

b)   *The delay method* which uses the time lag corresponding to the maximum of the same cross-covariance function.

The concept of these techniques is schematically shown in Figure 3.2. Figure 3.3 shows a comparison between the transverse wind obtained from the slope method and a simple average from seven propellor-type anemometers spaced along the path. By using three such systems arranged to form a triangle, horizontal divergence has been successfully measured (Kjelaas and Ochs, 1974). The same technique has been used in a study of the spatial horizontal wind in connection with gravity wave induced wind fluctuations (Kjelaas et al, 1974b).

Figure 3.2

A schematic diagram of the normalized covariance function, showing delay to the peak and the slope at zero lag. While the former is frequently used to measure pattern drift velocities, the latter is more suitable in the optical case where the pattern decays rapidly (from Lawrence et al, 1972)
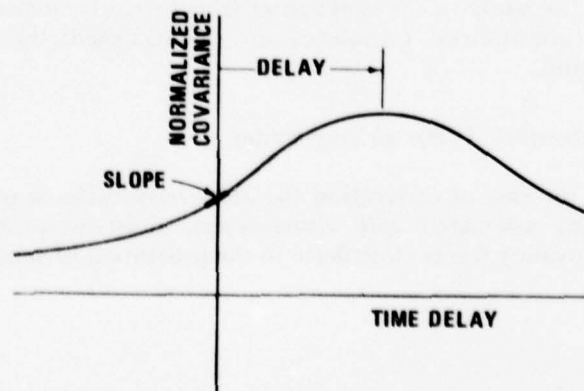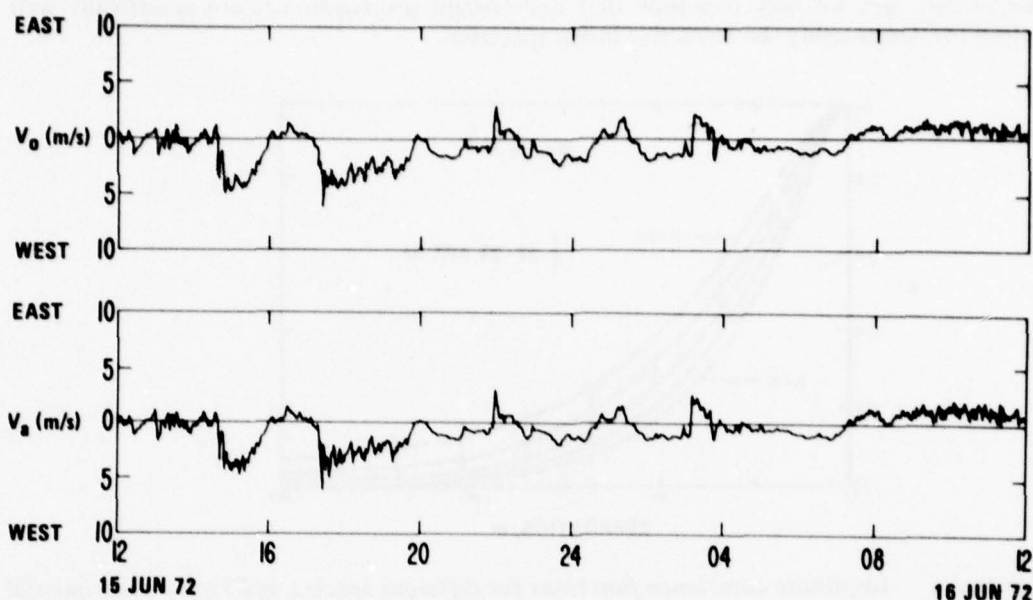
Figure 3.3 A comparison of the average wind speed (V_o) measured optically, with the average of the readings of six Gill anemometers (V_a) uniformly spaced along the optical path (from Kjelaas and Ochs, 1974)

Both the anemometers and the optical system measure the component of wind which is horizontal and at right angles to the path. The path is 300 m long, oriented north–south, and 3 m above the ground.

Measurement of vertical wind profiles using scintillations of light from stars has been attempted, but this technique is not sufficiently well developed to give detailed results. It probably requires detailed information about the refractive index spectrum as a function of height, which is difficult to obtain. Gossard (1960) and Gjessing et al (1973) have found that the form of the spectrum varies in a complicated manner with height.

3.2 Radars

According to Equation (2.12) the backscattered signal is determined by the refractive index spectrum, i e by the spectral density at the wave number corresponding to one half wavelength, $K = 4\pi/\lambda$. The direction of K is in the radar radial direction.

In the study of the backscatter from refractive index fluctuations, two different regimes of atmospheric turbulence are distinguished: the convection regime and the stable regime.

3.2.1 Detection of clear air convection

In the case of convection the radar backscatter is produced by refractive index fluctuations associated with rising, warm, moist air produced by surface heating. Positive buoyancy forces contribute to the generation of small-scale turbulence.

If the wavenumber $K = 4\pi/\lambda$ falls within the inertial subrange, the radar cross-section for a region of refractive index fluctuations will be proportional to C_n^2 averaged over a volume determined by the beamwidth and the pulse length. As the structure constant C_n^2 is connected with dissipation of energy and refractivity fluctuations through Equation (2.30), radar measurements may provide a complete description of the microstructure in the inertial subrange. For more details, the reader is referred to Ottersten (1969).

Atlas and Hardy (1966) and Konrad (1970), among many others, have observed free convection using highly sensitive radars.

Recently Noonkester et al (1973) have demonstrated that also FM−CW radars are capable of detecting clear-air convective patterns.

3.2.2 Radar detection of stable regimes

In stable air the turbulence and also the refractive index fluctuations are suppressed by negative buoyancy forces. In this stable regime the scatter is caused by refractive index fluctuations associated with turbulence generated by mechanical energy extracted from the mean flow. Inside regions of large transfer of kinetic energy from windshear into turbulent motion, the C_n^2 can according to Ottersten (1969) be expressed in terms of the potential refractive index gradient $d\phi/dz$, the gradient of horizontal wind du/dz and the flux Richardson number R_f as

$$C_n^2 = a^2 \epsilon^{2/3} \left(\frac{d\phi}{dz}\right)^2 \left(\frac{du}{dz}\right)^{-2} [1 - R_f]^{-1} \tag{3.1}$$

From Equation (3.1) we see that the profiles of refractive index and wind may create conditions with large C_n^2 and enhanced backscatter.

3.2.3 Measurement of wind field using radars

The wind field can be studied using Doppler radars, but mainly under precipitation conditions using the precipitation particles as tracers.

In clear, cloud-free air, a release of man-made targets is usually needed. Such targets might be thin aluminium-coated fiberglass needles cut to one-half of the radar wavelength employed.

With one fixed radar only, the radial wind component can be obtained. From a VAD scan both the horizontal wind and the mean profile can be calculated.

From information about the Doppler spectral variance, information on the turbulent kinetic energy may be derived under restricted conditions. The variance σ_V^2 of the Doppler spectrum can be written as

$$\sigma_V^2 = \sigma_S^2 + \sigma_F^2 + \sigma_B^2 + \sigma_T^2$$

where the individual terms are the variances of wind shear, σ_S^2; the fall speed, σ_F^2; the finite beamwidth, σ_B^2; and the turbulent kinetic energy, σ_T^2. To separate σ_T^2 from this equation is not always a simple problem. For details the reader is referred to Lhermitte (1968) and Wilson (1970).

An example of an analysis of both the mean wind field and the turbulence field is shown in Figure 3.4.
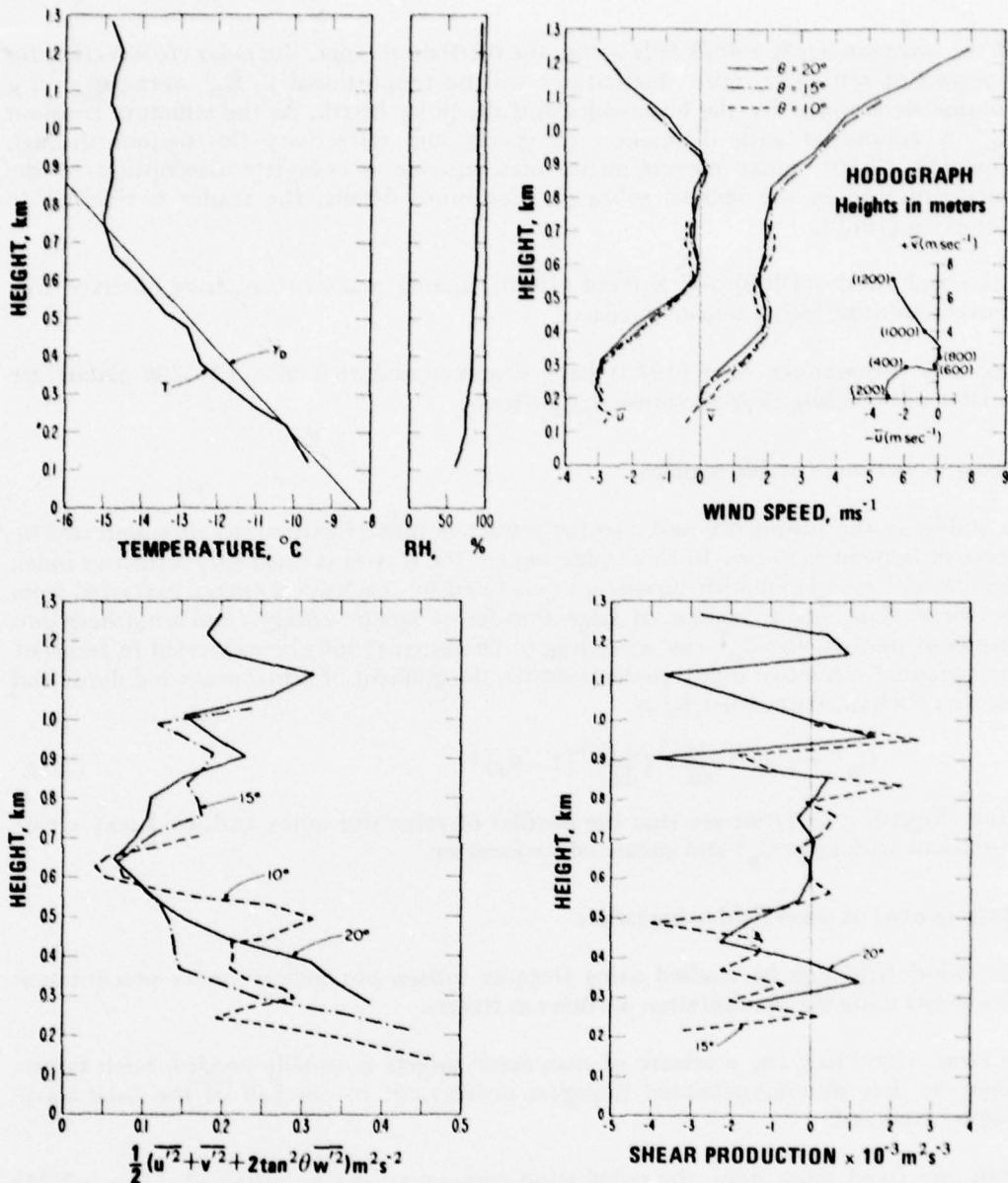
Figure 3.4 Mean wind field and turbulence field as determined from VAD Doppler information in snow (from Wilson, 1970)

    a) temperature sounding
    b) mean wind profiles
    c) turbulent kinetic energy profiles
    d) mechanical production rate

The velocity resolution is better than 0.25 ms^{-1}

To overcome the restrictive time stationarity and homogeneity assumptions which have to be made in VAD, two or three radars can be used (COPLAN scanning).

An example of the potential of the COPLAN-scanning in obtaining two-dimensional wind is shown in Figure 3.5. This technique is powerful in examining the detailed structure of the windfield in convective storms.

It can be concluded that Doppler radar is a powerful tool in the study of atmospheric motion.
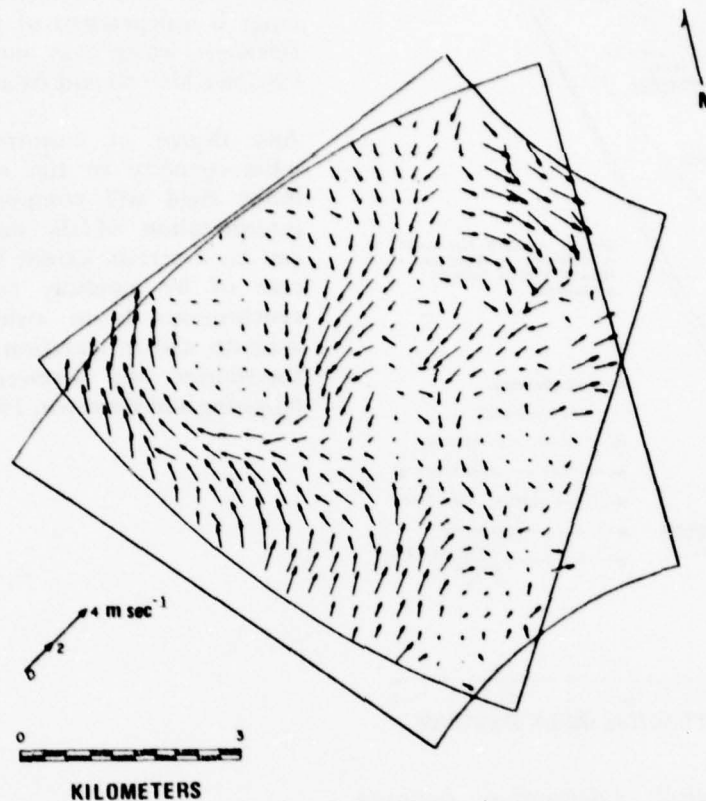
Figure 3.5 *Two-dimensional vector eddy flow field obtained from the radial velocity fields measured by two Doppler radars operated in the COPLAN scanning mode*
(Data taken by the radar group at the Wave Propagation Laboratory in Boulder.)

3.3 Beyond the horizon EM scatter

3.3.1 Determination of the refractive index spectrum $\Phi_n(K)$

Of the techniques discussed so far, forward scatter experiments are the only group which has been successfully used to deduce the three-dimensional refractive index spectrum.

Gjessing (1969) has discussed the sensitivity of different forward scatter methods to the form of the refractive index spectrum. His results are shown in Figure 3.6, where he concludes that two-frequency and vertical beamswing experiments are the most sensitive to the form of the refractive index spectrum.

In a later paper (Gjessing, 1973) he has tried to interpret the variability in the form of the measured refractive index spectra assuming atmospheric stratifications. The steeper spectra may be explained by this assumption. His calculations are based on the
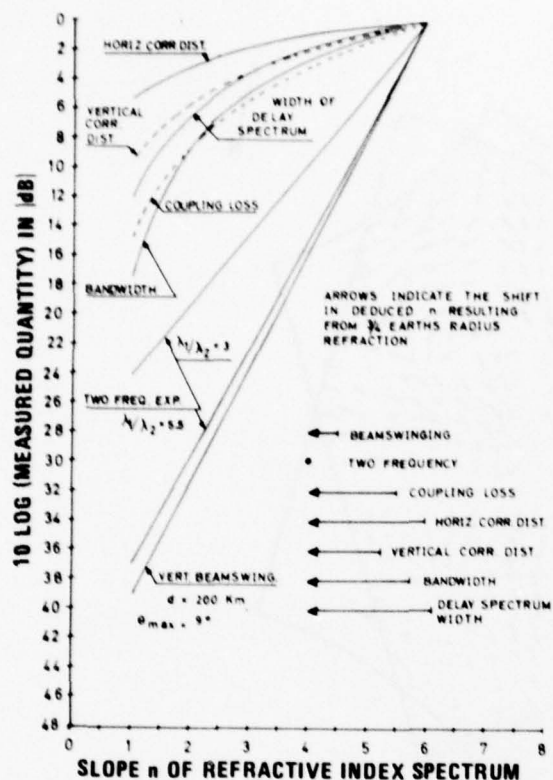
Figure 3.6 Theoretical relationship between measured quantity and the slope n of the refractive-index spectrum $(\Phi(K) \sim K^{-n})$

Length of the arrows shows the effect of radiation on the n deductions (from Gjessing, 1969)

assumption that the inertial sub-range is independent of the layer thickness, which may not be the case (see Metcalf and Atlas, 1973).

Any degree of anisotropy and inhomogeneity in the refractive index field will complicate the interpretation of the data. This can to a certain extent be taken care of by carefully controlled synchronous beam swinging in azimuth and in elevation of both transmitter and receiver beams (Gjessing and Børresen, 1967).

3.3.2 Measurements of wind by forward-scatter techniques

When discussing wind measurements using forward scatter Doppler, one must distinguish between the post-detection intensity fluctuation spectrum S(F), which is a measure of the Doppler spread, and the pre-detection spectrum S(f) which includes the Doppler shift (Atlas, 1969).

The Doppler spread is affected by a combination of the cross-path component of the wind and the spatial variation of the wind within the scattering volume.

If we have access to the absolute Doppler frequency at the receiver, we can obtain information about the cross-path wind. Doppler shift (i e the mean cross-path wind) can in principle be measured with rake delay techniques (Birkemeier, 1972).

Recently Olsen and Lammers (1973) have clearly demonstrated the capability of a troposcatter system for measuring wind velocity. Some of their results from a 500 km long scatter link are shown in Figure 3.7.

For further details regarding the use of EM forward scatter as a remote sensing technique the reader is referred to Cox (1969).
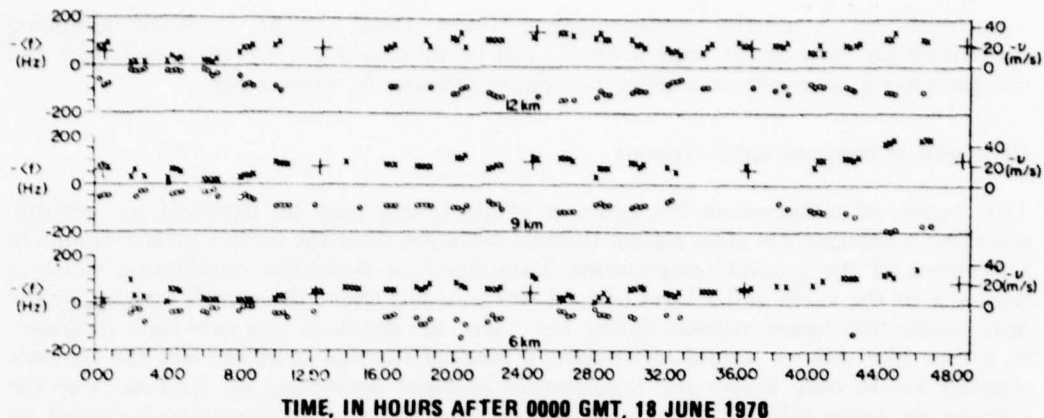
TIME, IN HOURS AFTER 0000 GMT, 18 JUNE 1970

Figure 3.7 Comparison of scatter and radiosonde measurements of cross-path wind speed at 6.9 and 12 km using rake technique(from Olsen and Lammers, 1973)
Scatter measurements at 10 km off path:
o windward side, x leeward side, + radiosonde measurements

3.4 Probing the atmosphere with acoustic sounders

The backscattered acoustic signal is determined by the spectrum of the acoustic refractive index, i e by the spectral density at the wavenumber corresponding to one half acoustic wavelength. This is directly analogous with the radar case.

For pure backscatter, only temperature fluctuations will contribute, while in the case of forward scatter (bistatic mode) both the wind and temperature spectra will contribute to the scattering.

Because of the strong influence on acoustic waves of air temperature, acoustic sounding technique is a powerful tool for studying atmospheric structure in which temperature fluctuations can be used as tracers.

As in the case of radars, two different regimes of atmospheric turbulence are distinguished; the convection regime and the stable regime.

3.4.1 Detection of clear air convection
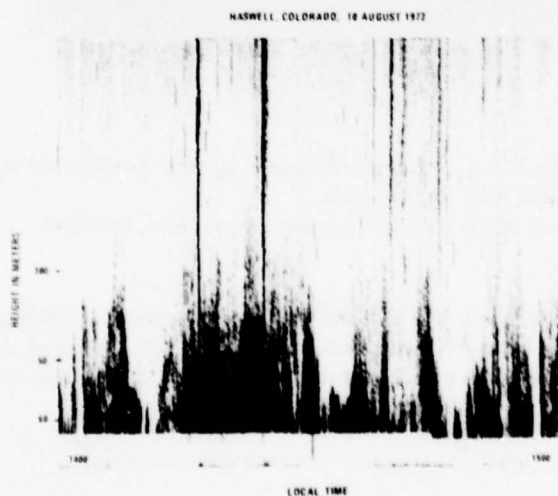
Figure 3.8 Facsimile recording of backscatter acoustic intensity from convective plumes (from Kjelaas and Ochs, 1974)

Acoustic echo-sounding is specially well suited for studies of thermal activities in the troposphere. As an example, a typical recording obtained during unstable conditions is shown in Figure 3.8. The dark portions of this recording correspond to thermal plumes. The different grey tones on the facsimile recordings can be interpreted as C_T values, which again are a measurement of the temperature fluctuations. Rather good agreement (within 50%) has been found between sounder measurements of C_T and C_T calculated from measurements of temperature differences over a distance equal to one-half acoustic

wavelength on a nearby meteorological tower (Hall, 1973). Acoustic sounding techniques are now at the stage were C_T can be measured as a function of height and comparison can be made with different existing theories for convection.

3.4.2 Detection of temperature inversions

Two types of temperature inversion or stable layers may be detected by acoustic sounding technique. On clear nights, thermal radiation from the earth's surface results in a lowering of the ground temperature. Turbulence or molecular conduction causes a heat loss to the earth and a layer of cold air forms just above the earth's surface. As the heat conduction losses increase during the night, the depth of this cold layer increases. In a case like this we would not expect a random thermal structure and the acoustic sounder would only detect the temperature gradient separating the cold air from the warmer air above (Hall, 1973). A second type of temperature inversion is caused by subsidence.

A typical facsimile display illustrating the potential of the technique under stable conditions is shown in Figure 3.9. The dark portions of the picture are regions from which echoes were received. In this figure different types of atmospheric structures are illustrated. The lowest dark portion of the records is the nocturnal inversion. At about 0600 hours this radiation inversion starts lifting and finally at about 1000 hours free convection is more or less developed. Above this inversion we observe a wavy structure which is probably caused by wind shear induced instabilities or Kelvin–Helinholtz billows. Hook et al (1972) have reported an excellent agreement between the observed K–H waves or gravity waves, and the corresponding pressure fluctuation observed on a microbarograph. Kjelaas et al (1974a) have demonstrated the capability of an array of acoustic sounders in determining phase velocities of gravity waves.

HASWELL COLORADO, 23 JULY 1972
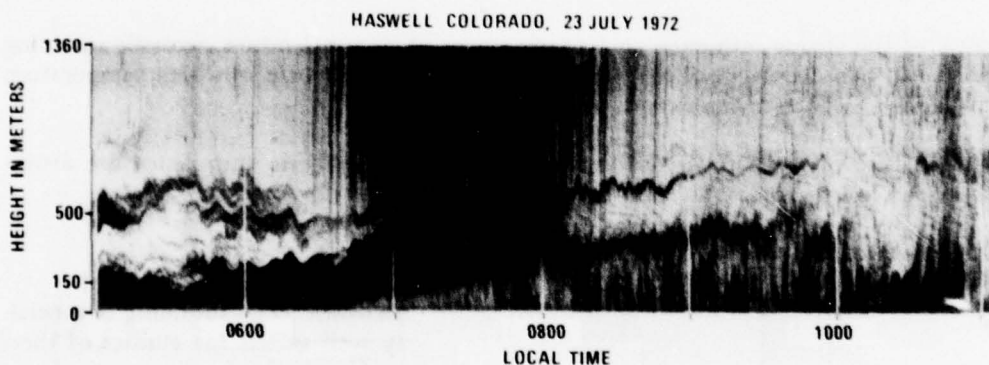
Figure 3.9 Facsimile recording of backscatter acoustic intensity during conditions of nocturnal inversion and breaking up of the same
(Data taken by the Acoustic Group of the Wave Propagation Laboratories, Boulder.)

Under stable conditions the agreement between the C_T derived from acoustic sounding measurements and C_T calculated from temperature measurements is not as good as when the atmosphere is convectively unstable. This may be due to reflection or enhancement of the returned signal because of focusing effects.

3.4.3   Measurements of wind velocity using acoustic sounding technique

As in the case of EM propagation, the Doppler frequency shift can be used to determine the wind component along the dir.$(\vec{k}_S - \vec{k}_O)$, which is the bisector of the angle formed by the incident beam and the scattered beam. For acoustic waves, refraction of the beam may be a problem and can lead to misinterpretations. An analysis of the influence of beam bending is therefore important for every experimental configuration of acoustic soundings (Beran and Clifford, 1972). A typical Doppler-derived vertical velocity pattern for a convective plume is shown in Figure 3.10. On the left-hand side of the figure is the corresponding backscatter intensity.

ERIE, COLORADO, 9 OCTOBER 1970
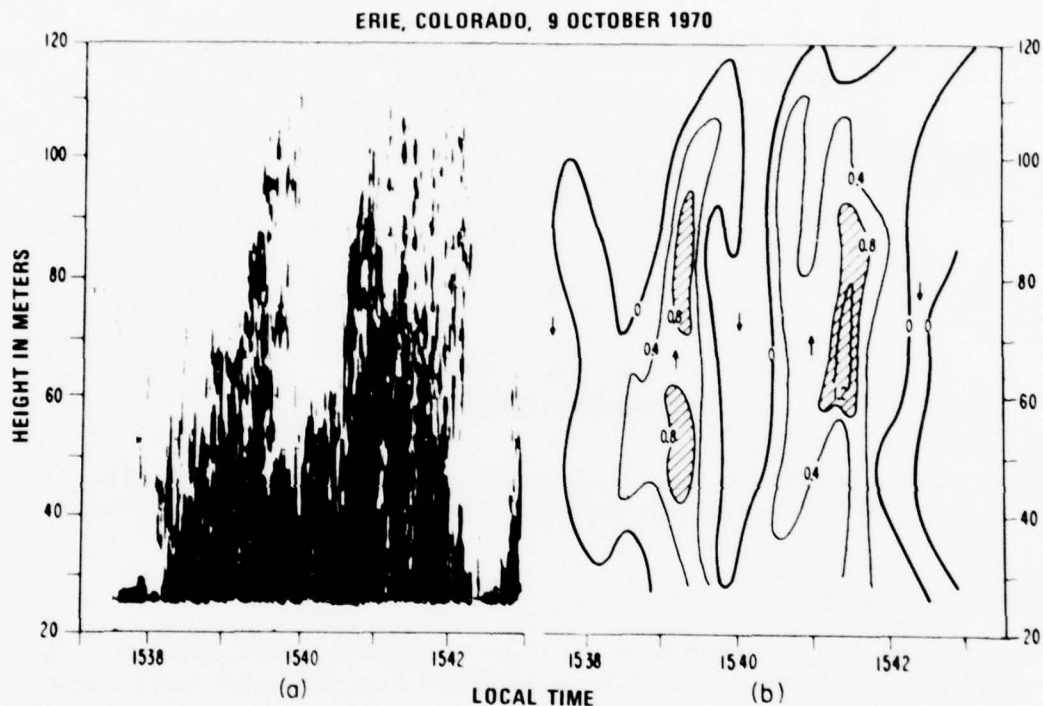
Figure 3.10   Acoustic echoes (left) and Doppler derived vertical velocity field during thermal plume activity (from Beran et al, 1971)
Contour interval is 0.4 ms^{-1}; regions of vertical velocity > 0.8 ms^{-1} are shaded; arrows indicate direction of vertical component.

Figure 3.11 shows an example of the total wind vector determined by employing three inclined acoustic echo sounders. The agreement with the radiosonde derived wind velocity is convincing; the technique has great possibilities as a wind sensor in the lower troposphere.

Figure 3.11 *Comparison between wind profile measured with radiosonde and the one derived from acoustic Doppler measurement (from Beran et al, 1974)*

3.4.4 Flux measurements

Using similarity theory, which seems to model free convection well, heat flux can be related to C_T^2; accordingly heat flux can be gained from the backscattered acoustic energy.
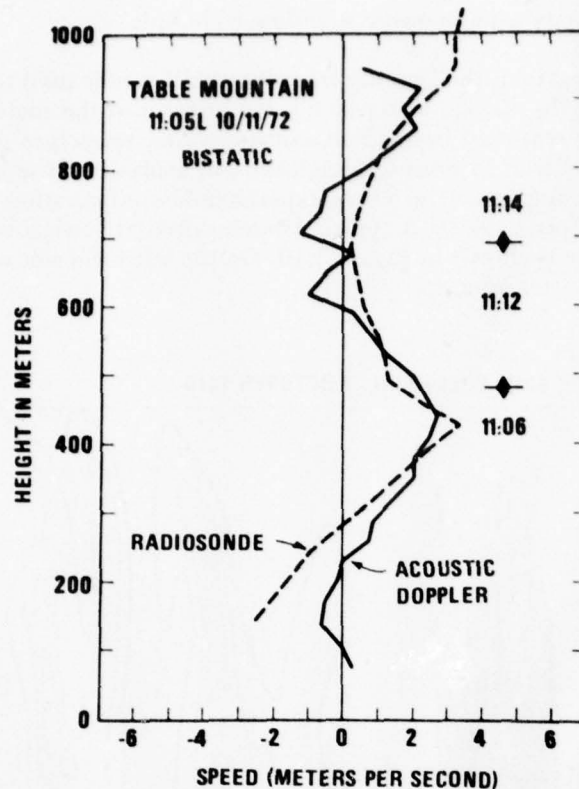
Using intersecting beams from three sounders, the wind vector can be measured. When velocity changes from pulse to pulse are computed, thus yielding $u'w'$ and $v'w'$, a measure of the vertical momentum flux or stress is derived (Hall, private communication, 1973).

Further, the dissipation may be measured by analyzing pulse to pulse velocity differences, the second moment of the Doppler spectra, or alternatively from bistatic scattering measurements, where C_V^2 contributes to the acoustic scatter.

3.5 Summary of experimental techniques

Table 3.1 summarizes the relative merits of the techniques discussed in the previous sections. Again we want to emphasize that only the techniques where the received signal is determined by refractive index inhomogenities are discussed. Thus factors such as absorption and molecular scattering where the signal reacts with individual molecules are excluded.

From Table 3.1 we see that no single technique provides information about all the listed parameters for describing the atmospheric structure. If more than one technique is used simultaneously, we shall have to remember that the various techniques may be sensitive

SENSING TECHNIQUE	WIND — MEAN — HORIZONTAL TRANS	WIND — MEAN — HORIZONTAL LONGT	WIND — MEAN — VERTICAL	WIND — TURBULENCE STRUCTURE CONSTANT	WIND — DIVERGENCE	WIND — FLUX	TEMPERATURE — MEAN	TEMPERATURE — STRUCTURE CONSTANT	TEMPERATURE — $\Phi_T(K)$	TEMPERATURE — HEAT FLUX	HUMIDITY — MEAN	HUMIDITY — STRUCTURE CONSTANT	REFRACTIVE INDEX — MEAN	REFRACTIVE INDEX — STRUCTURE CONSTANT	REFRACTIVE INDEX — $\Phi_n(K)$
LINE-OF-SIGHT															
OPTICAL	LA				2D			LA	LA						
MICROWAVE	LA						LA	LA	LA		LA		LA	LA	LA
RADAR															
SINGLE DOPPLER RADAR†		LA LP[1]	LP[2]												
MULTI-STATION DOPPLER RADARS††	LP[1]	2D[1]													
FM—CW RADAR														LP[4]	
PULSE RADAR														LP[4]	
ACOUSTIC															
SINGLE MONOSTATIC	LP		LP					3D LP		LP[3]					
BISTATIC + MONOSTATIC WITH DOPPLER	LP	LP	LP	LP		LP		3D LP		LP[3]					
FORWARD SCATTER															
SYNCHRONOUS VERTICAL BEAM SWINGING															
DOPPLER MEASUREMENT WITH RAKE SYSTEM	LP														3D[4]

METEOROLOGICAL VARIABLES TO BE MEASURED

COMMENTS:

† A SINGLE SCANNING DOPPLER RADAR WILL GIVE 2D PLOTS OF RAD VEL

†† 2D VECTOR WIND FROM TWO RADARS SCANNING IN COPLAN

ALL THE RESULTS FROM RADAR, ACOUSTIC AND FORWARD SCATTER ARE AVERAGED OVER SOME PULSE VOLUME.

LA – LINE AVERAGE
LP – LINE PROFILE
2D – TWO-DIMENSIONAL
3D – THREE-DIMENSIONAL

[1] HAVE TO USE CHAFF
[2] RADIAL VELOCITIES
[3] FROM C_T MEASUREMENTS
[4] THREE-DIMENSIONAL SPECTRUM FOR $\vec{K} = \vec{k}_0 - \vec{k}_s$

Table 3.1 Status of line-of-sight propagation, radar, acoustic echosounding and forward scatter techniques in the study of tropospheric structure.

to different portions of the refractive index wavenumber spectrum, i e different scale size of the refractive index inhomogenities, viz

—	radar and acoustic	$\sim 1-10$ cm	$(\lambda/2)$
—	optical line-of-sight	$\sim$ cm	(first Fresnel zone)
—	microwave line-of-sight	$\sim$ a few m	(first Fresnel zone)
—	forward scatter	$\sim 1-20$ m	$(\lambda/2 \sin \theta/2)$

In addition to being sensitive to different scale sizes, the variables measured may be averaged over different distances and volumes.

For line-of-sight the average volume is determined by the length of the path and some weighting along the path, and by the beamwidth.

In the case of radar and acoustic backscattering devices, the volume over which the variable is averaged is determined by the beamwidth and by the length of the transmitted pulse.

For forward scatter the volume is given by the beam width, scattering angle and distance between transmitter and receiver.

We shall now briefly discuss Table 3.1.

3.5.1 Wind

From Table 3.1 we see that mean wind and wind fluctuation can be measured in several different ways, although in the absence of refractive index fluctuations of sufficient intensity a tracer such as snow, rain or chaff must be employed in the radar backscatter case. This has been the case for Doppler radar studies, where a two-dimensional coverage of the wind field has been obtained. This is not the case with forward scatter when the sensitivity is $(\sin \theta/2)^{-11/3}$ better than for backscatter.

A line average of the transverse wind can be obtained from both microwave and optical line-of-sight propagation. The two-dimensional horizontal wind has also been successfully measured with optical line-of-sight propagation methods. The vertical profile of the three-dimensional wind can be obtained using acoustic sounding Doppler techniques. From acoustic sounding some knowledge about C_V^2, the turbulence structure constant, can be gained. As acoustic technique also gives the three-dimensional wind, momentum flux can also be derived. Profiles of transverse wind can also be measured from EM forward scatter techniques, providing absolute Doppler can be measured.

From optical line-of-sight propagation techniques, horizontal divergence has been successfully derived.

3.5.2 Temperature

Because of the strong dependence of humidity rather than of temperature on the radio refractive index, available techniques for temperature probing are limited to optical and acoustic waves. A line average of the mean temperature as well as of the intensity of the temperature fluctuation, C_T^2, can be derived from optical line-of-sight propagation measurements. In some cases also information about the shape of the temperature spectrum can be obtained.

Acoustic sounding techniques can also give a line profile of the C_T^2 averaged over some volume (pulse volume). During adiabatic conditions the vertical heat flux can be derived from the C_T^2 and the vertical wind velocity.

3.5.3 Humidity

Measurements of humidity are difficult to perform because the optical and acoustic refractive indexes are insensitive to humidity and the microwaves are influenced both by temperature and humidity. By assuming the temperature more or less constant over a path, microwave line-of-sight technique has been used to measure a line average of the water vapour pressure.

3.5.4 Refractive index

As discussed in section 2.1, the refractive indexes for optical, micro, and acoustic waves are mostly dependent on temperature, humidity and temperature, and temperature and wind velocity, respectively. Microwave line-of-sight will give a line average of both the mean and the fluctuations C_n^2 of the radio refractive index, and in some cases information about the form of the refractive index spectrum.

For backscatter, both microwave and acoustic, the intensity of the refractive index fluctuations C_n^2 can be measured as a function of height. Microwave forward scatter has been used to derive the three-dimensional refractive index spectrum.

As noted earlier, different techniques are sensitive to different scale sizes, averaging distances and volumes and in most cases are suitable for only limited regions of the atmosphere. In Table 3.2 we have divided the atmosphere into three regions and listed the techniques which may be used within each region:

Line-of-sight — mainly suitable for measurements within a few meters above the ground, although paths from sea-level to mountain-top have been used, and earth—satellite measurements are becoming available.

Radars — different radars have been used from a few meters above ground to many kilometers, both vertical and slant.

Acoustic sounding — greatest potentials from a few meters up to a few kilometers.

Forward scatter — since generally beyond horizon, usable region from a few kilometers above ground to many kilometers.

HEIGHT ABOVE GROUND		
~10 km	FORWARD SCATTER	A) FORM OF THE THREE-DIMENSIONAL REFRACTIVE INDEX SPECTRUM $\Phi_n(K)$ B) MEAN WIND VELOCITY WITHIN THE SCATTERING VOLUME C) TURBULENCE INTENSITY D) LINE PROFILE OF TRANSVERSE WIND
	PULSE AND DOPPLER RADARS	A) INTENSITY OF REFRACTIVE INDEX FLUCTUATION, C_n^2 B) RADIAL VELOCITIES
~1000–2000 m	ACOUSTIC SOUNDERS	A) WIND PROFILE TRANSVERSE AND LONGITUDINAL COMPONENTS B) INTENSITY OF TEMPERATURE FLUCTUATIONS, C_T^2 C) VERTICAL TRANSPORT OF MOMENTUM AND HEAT D) VORTICITY
	PULSE AND FM–CW RADARS	A) TWO-DIMENSIONAL WIND (USING CHAFF) B) INTENSITY OF REFRACTIVE INDEX FLUCTUATION, C_n^2
~10 m	LINE-OF-SIGHT	A) LINE AVERAGE TRANSVERSE WIND B) INTENSITY OF TEMPERATURE FLUCTUATIONS, C_T^2, REFRACTIVE INDEX, C_n^2 C) FORM OF THE TEMPERATURE SPECTRUM, REFRACTIVE INDEX SPECTRUM D) CONVERGENCE/DIVERGENCE IN HORIZONTAL WIND E) LINE AVERAGE OF WATER VAPOUR

Table 3.2 Height intervals over which different remote sensing techniques may be used

4 CONCLUSION

It can be concluded that carefully designed wave propagation and scatter experiments can provide information about the atmospheric structure otherwise not readily obtainable. Some of the techniques discussed in this paper are in a formative rather than a productive stage. This is particularly the case with forward scatter and line-of-sight experiments, although optical line-of-sight seems to be a very useful remote wind-sensor. Acoustic sounding techniques are in a stage of rapid development and it has been demonstrated that this technique has very great potentials in sensing both wind and the thermal structure of the atmosphere. High resolution radars, such as the FM—CW radar, have revealed the existence of thin, undulating layers and waves in the atmosphere which have not been known before. These waves (K—H waves) may be of importance for a further understanding of the transport of momentum in the boundary layer.

The high power pulse-radars contribute to the understanding of clear air echo (CAT) and the study of gravity waves. Multistation pulse Doppler radars scanning in a plane (COPLAN) are used to study the horizontal wind field within thunderstorms, snowstorms and also in the clear air when employing chaff (artificial tracer). These experiments add new and useful information to the knowledge about the cell structure of such storms.

Acknowledgements

References

(1) Atlas, D — Tech Rep 10, Laboratory of Atmospheric Probing, University of Chicago (1969)

(2) Atlas, D
K R Hardy — Proc XV, General Assembly of URSI, Munich (1966)

(3) Beran, D W
S F Clifford — Proc AMS Second Symposium on Meteorological Observations and Instrumentations, San Diego, California, 100, (1972)

(4) Beran, D W
B C Willmarth
F C Carsey
F F Hall — J Acoust Soc Am (*In press*)

(5) Birkmeier, W P — Tech Rep 10, Laboratory of Atmospheric Probing, University of Chicago (1972)

(6) Browning, K A
R Wexler — J Appl Meteorol, 7, 105 (1968)

(7) Clifford, S F
E H Brown — J Acoust Soc Am 48, 5, 1123 (1970)

(8) Cox, D C   — Atmospheric Exploration by Remote Probe
                                     s, Proc Scientific Meetings of the Panel on
                                     Remote Atmospheric Probing (1969)

(9) Gjessing, D T   — Proc IEE, London, **109**, 446 (1962)

(10) Gjessing, D T   — Radio Sci 4, 12, 1195 (1969)

(11) Gjessing, D T   — Bound-Layer Meteorol 4, 376 (1973)

(12) Gjessing, D T   — Structure of the Lower Atmosphere and
     J A Børresen   Electromagnetic Wave Propagation, NATO
                                     Advanced Study Institute, Wales (1967)

(13) Gjessing, D T   — Bound-Layer Meteorol 4, 475 (1973)
     A G Kjelaas
     E Golton

(14) Gossard, E E   — IRE Trans **AP**–8, 186 (1960)

(15) Hall, F F Jr   — Remote Sensing of the Troposphere, *ed
                                     V E Derr*, US Department of Commerce
                                     (1973)

(16) Harp, J C   — Statistical Methods and Instrumentation in
                                     Geophysics, *ed A G Kjelaas*, Teknologisk
                                     Forlag, Oslo, 213 (1971)

(17) Hook, W H   — Bound-Layer Meteorol 2, 371 (1972)
     J M Young
     D W Beran

(18) Kjelaas, A G   — J Atmos Sci (1974a) (*In press*)
     D W Beran
     W H Hook
     B R Bean

(19) Kjelaas, A G   — Tellus (1974b) (*In press*)
     E E Gossard
     J M Young
     W R Moninger

(20) Kjelaas, A G   — J Appl Met (1974) (*In press*)
     G R Ochs

(21) Konrad, T G   — J Atmos Sci 27, 1138 (1970)

(22) Lawrence, R S   — Appl Opt 11, 239 (1972)
     G R Ochs
     S F Clifford

(23) Lee, R W   — Radio Sci 4, 1211 (1969)

(24) Lee, R W   — Proc IEEE 57, 375 (1969)
     J C Harp

(25) Lhermitte, R M   — Proc 13th Radar Meteorology Conference,
                                     498 (1968)

(26) Lhermitte, R M
D Atlas
— Proc 9th Weather Radar Conference, 218 (1961)

(27) Lhermitte, R M
L J Miller
— Proc 14th Radar Meteorology Conference, 133 (1971)

(28) Little, C G
— Remote Sensing of the Troposphere, *ed V E Derr*, US Department of Commerce (1973)

(29) Metcalf, J I
D Atlas
— Bound-Layer Meteorol 4, 7 (1973)

(30) Monin, A S
— Soviet Physics-Acoustics 7, 370 (1962)

(31) Noonkester, V R
D R Jensen
J H Richter
— NELC/TR1849, US Naval Electronics Laboratories Center US (1972)

(32) Olsen, R L
U H W Lammers
— Propagation of Radio Waves at Frequencies above 10 GHz, Proc IEEE Conf, London, 197 (1973)

(33) Ottersten, H
— Radio Sci 4, 1179 (1969)

(34) Shen, L
— IEEE Trans AP–18, 4, 493 (1970)

(35) Strohbehn, J W
— Proc IEEE 56, 8, 1301 (1968)

(36) Strohbehn, J W
— J Geophys Res 75, 1067 (1970)

(37) Strohbehn, J W
— Bound-Layer Meteorol 4, 397 (1973)

(38) Tatarski, V I
— Wave Propagation in a Turbulent Medium, McGraw-Hill, New York (1961) *Translated from Russian*

(39) Tatarski, V I
— The Effects of the Turbulent Atmosphere on Wave Propagation, US Department of Commerce (1971) *Translated from Russian*

(40) Wilson, D A
— Proc 14th Radar Meteorology Conference, 191 (1970)

(41) Beran, D W
C G Little
B C Willmarth
— Nature 230, 160 (1971)

(42) Ottersten, H
K R Hardly
C G Little
— Bound-Layer Meteorol, 4, 47 (1973)

Study of Divergence in the Boundary Layer Using Optical Propagation Techniques

A. G. KJELAAS
Norwegian Defence Research Establishment, Kjeller

G. R. OCHS
Environmental Research Laboratories, NOAA, Boulder, Colo. 80302

Study of Divergence in the Boundary Layer Using Optical Propagation Techniques[1]

A. G. KJELAAS

Norwegian Defence Research Establishment, Kjeller

G. R. OCHS

Environmental Research Laboratories, NOAA, Boulder, Colo. 80302

(Manuscript received 25 July 1973, in revised form 27 November 1973)

ABSTRACT

A wind-measuring system using three separate optical systems, each consisting of a 3 mW He-Ne laser and two photodiode receivers, forming an equilateral triangle 300 m on a side, has successfully measured the divergence over the area of the triangle, and the space-averaged horizontal wind vector. Good correlation was found between the flow into the triangle and occurrences of thermal plumes seen by an adjacent acoustic sounder. The flow into the triangle was proportional to the vertical velocity. During large convective activity, there was a certain periodicity in the occurrence of plumes.

1. Introduction

Reliable measurements of the divergence of the horizontal wind are difficult to achieve. Many attempts have been made to develop methods based on point measurements of wind. On the synoptic scales, Bellamy (1949) developed a technique that used a triangle of wind reports to calculate the divergence for the enclosed area; Endlich and Clark (1963) calculated divergence by linear interpolation between wind components at the vertices of the triangle of observation. Eddy (1964) improved Bellamy's triangle technique by using a computer model. He also applied a correlation technique to establish the space correlation and time persistence.

On smaller scales (i.e., those scales comparable with plumes and on up to a few hundred meters), no reliable techniques for measuring the horizontal divergence exist. Many laboratory experiments have formed the basis for different theories for entrainment into plumes. Morton *et al.* (1956) have described a model assuming that the rate of entrainment into the plumes is proportional to the vertical velocity inside the plume. Telford (1966) has developed a model assuming that the entrainment should not be related to the mean velocity but to the local level of turbulence.

Due to lack of suitable wind-measuring techniques these theories have been difficult to check in the atmosphere. Recently, remote sensing of space-averaged wind has progressed, making it possible to calculate the

divergence for a small enclosed area. Lawrence *et al.* (1972) have described an optical wind sensor that uses the naturally occurring density fluctuations to obtain a spatially averaged wind. By using a correlation technique at the receiver, they are able to extract a path-averaged transverse wind speed.

This paper discusses field measurements of divergence and wind velocity based on an extension of the optical technique. A He-Ne laser triangle path (300 m on a side) was set up near a 150 m tower. The results are compared with wind velocity measured at five levels on the tower and with the occurrence of plumes as seen by an acoustic sounder located inside the triangle.

2. The optical measuring equipment

The optical technique used for wind measurement is described fully in Lawrence *et al.* (1972); however, a brief discussion is included here for completeness, since it is a recent development. The technique may be used over ranges from 300 m to more than 15 km, so that it is particularly useful for obtaining spatially averaged wind measurements. In addition, it is effective for measuring low mean wind flow in the presence of large fluctuating components.

The technique uses the drifting scintillation pattern arising from wind-transported refractive-index irregularities in the atmosphere. This drifting scintillation pattern is the cause of the twinkling, or scintillation, of starlight. With a very small, bright light source, such as a laser shining through the atmosphere, the moving scintillation pattern can be seen clearly on a screen at night. The sizes of the irregular patches of light in the pattern are determined by the diffraction of the incident beam; they result from refractive-index irregularities

(almost entirely the result of temperature differences) at various positions along the propagation path. At each position, the diffraction process selects a most effective scale of irregularity, or eddy, whose size is sufficient to cause a half-wavelength difference in path-length to the receiver for two extreme rays passing through its edges. The diffraction effects of this particular eddy dominate over those of other eddies at the same location.

If a diverging laser beam is effectively a point source, geometric magnification increases the size of the received eddy image by the factor L/z, where z is the position along a beam of length L. The image drift rate at the receiver caused by the local eddy drift velocity, depending on the wind at position z, is also increased by the same factor. Therefore, the received optical disturbance is larger and moves faster than the eddy that produced it. Since different portions of the path contribute to the total scintillation pattern, that pattern will be continuously evolving because of the relative speeds of the different sized features it contains.

To measure the average component of the wind across an optical path, we look at fluctuations in light intensity in two small apertures spaced along the direction of movement of the pattern, as shown in Fig. 1. A function like that shown in Fig. 2 results if the normalized covariance of the logarithms of these signals is computed. For the conditions of a uniform wind at right angles to the optical path and parallel to the separation of the detectors, and for uniform refractive-index structure constant (C_n^2) along the path, some measure of the time scale of the function, e.g., the time delay to the peak or the slope of the function at zero delay, could be used to derive wind speed. For the real case, with winds of arbitrary direction and speed along the path, and with a non-uniform distribution of C_n^2 along the path, this function changes not only in time scale, but also in shape. It can be shown (Lawrence et al., 1972), for uniform C_n^2 along the path, that the slope of the function at zero delay has a known relationship to the average horizontal wind across the path, even though the wind along the path is non-uniform in direction and speed. Thus, we measure the slope at zero delay to determine the average wind. The weighting function of the wind measurement for various receiver separations is shown in Fig. 3 as a function of $\beta = \rho(\lambda L)^{-\frac{1}{2}}$, where ρ is the detector spacing, λ the laser wavelength, and L the path length. For the divergence

FIG. 2. A schematic diagram of the normalized covariance function, showing the delay to the peak and the slope at zero time lag. While the former is frequently used to measure pattern drift velocities, the latter is more suitable in the optical case where the pattern decays rapidly.

measurement reported here, $\beta = 0.46$. This separation, and the use of apertures 6 mm in diameter, gave a nearly symmetrical weighting function around the center of the path.

There are several limitations to the present optical system, but we no not believe that they affected the wind measurements reported here. The wind weighting function is strictly correct only when the wind measurement is averaged over enough time so that C_n^2 is statistically uniform over the path. This can be satisfied for a horizontal path, but if, for example, a slant path is used C_n^2 will tend to be higher at the lower end of the path, and the wind in this portion will be weighted more heavily. Random variations of C_n^2 will distort the measured average wind speed only if they are correlated with the variations in wind speed. A reasonable supposition is that turbulence is strongest at locations of maximum wind shear, not at locations of maximum wind speed. If so, the turbulence tends to be uncorrelated with the wind, and the average obtained by the

FIG. 3. The relative weights of the different portions of the path in determining the optically measured wind. The parameter $\beta = \rho(\lambda L)^{-\frac{1}{2}}$ is the separation of the sensors. These curves are calculated for point sensors; the finite area of a real sensor will tend to remove the negative weights near the receiver.
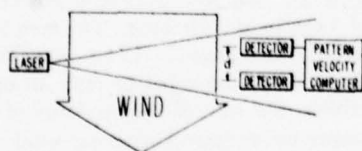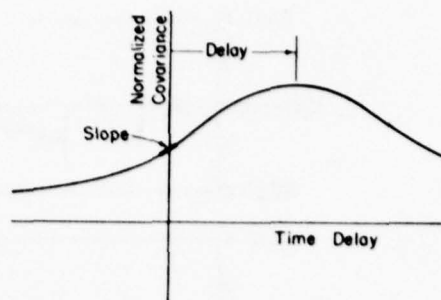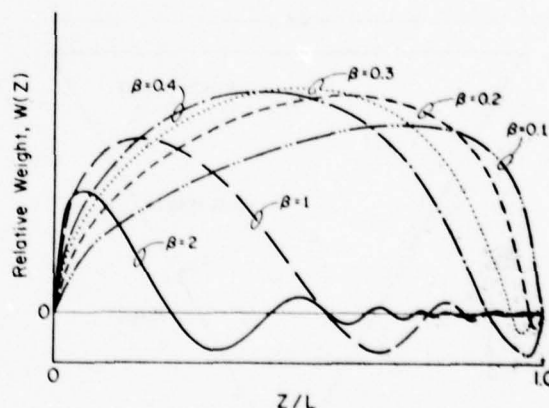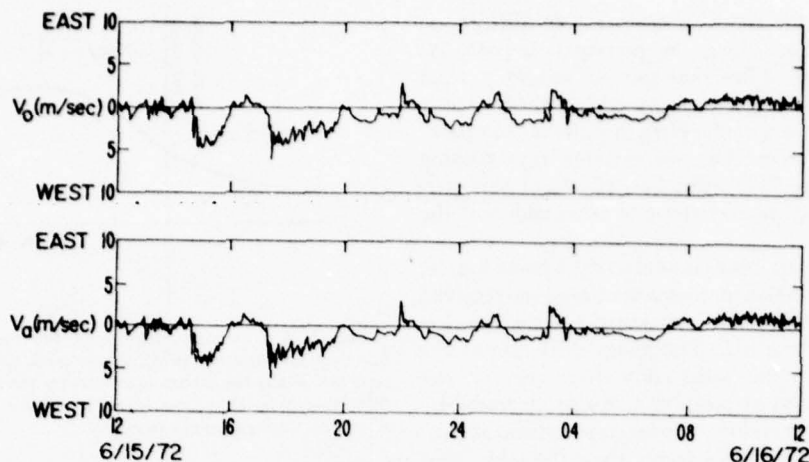

FIG. 1. The general arrangement used to measure the average component of the wind, across a laser beam, parallel to the (usually horizontal) spacing of two detectors.

FIG. 4. A comparison of the average wind speed (V_0) measured optically, with the average of the readings of six Gill propellor anemometers (V_a) uniformly spaced along the optical path. Both the anemometers and the optical system measure the component of wind that is horizontal and at right angles to the path. The path is 300 m long, oriented north–south, and 3 m above the ground.

optical system is unbiased. A second source of error may occur when there is a combination of high refractive-index fluctuations and long path. Under these conditions, a so-called saturation effect occurs, in which the optical scintillation no longer increases with $C_n{}^2$. When this condition occurs, the spherical propagation equations upon which the optical wind measurement is based are no longer correct. The result is that the optical measurement will underestimate the true wind, and in severe saturation this may be by a factor of 2 or more. Saturation may be easily detected by the optical system and did not occur on the 300 m paths used in our divergence experiment.

Before undertaking the divergence experiment, we

FIG. 5. The layout of the laser triangle, 150 m meteorological tower, and the acoustic sounder.

compared the average wind speed reading of one of the three optical systems, over the same height and path length that was later used, with the average of the readings of six Gill propellor anemometers uniformly spaced along the optical path. The anemometers were oriented to read the component of wind that was horizontal and at right angles to the optical path. The result for a 24-hr period is shown in Fig. 4 and appears to offer full proof of satisfactory performance.

3. Measurement and data reduction

The measurements were made at Haswell, Colo., during a two-week period in the beginning of August 1972. The Haswell area has a typical high-plain meteorological regime with strong radiative cooling during the night and strong solar heating and convective activity during the day.

Three separate optical systems, each consisting of a 3-mW He-Ne laser, two photodiode receivers, and a small specialized computer providing a real-time read-out of average wind speed, were used in the experiment. The optical paths formed an equilateral triangle, 300 m on a side and 2.3 m above the ground. Fig. 5 shows the location of the laser triangle relative to the meteorological tower and the acoustic sounder. The terrain near the triangle is flat and free from any obstacles for a minimum of 3 km in any direction. The area is covered with clumps of buffalo grass ($\sim$15 cm in height). Since each optical path was arranged to read an outflowing wind as positive, the sum of the readings of all three paths represents the average horizontal wind speed out of the triangle. The individual wind readings for each optical path, smoothed with a 10-sec running average, as well as the scalar sum of all three, were recorded
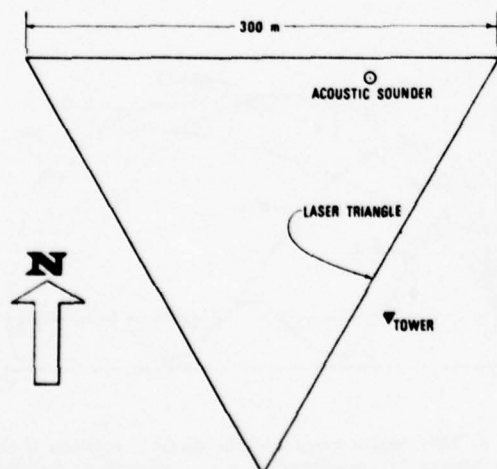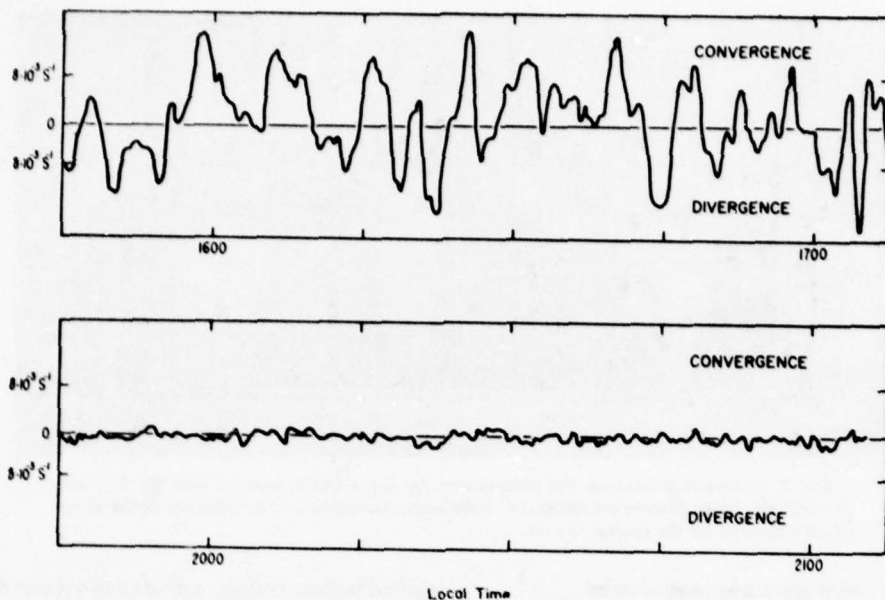
FIG. 6. Ten-second average divergence recordings for typical afternoon and night periods.

simultaneously on strip chart recorders and on a digital tape recorder.

The horizontal wind divergence is given by

$$\nabla_A \cdot \mathbf{V} = \frac{L(v_0 + v_{120} + v_{240})}{A},$$

where v_0, v_{120}, v_{240} are the wind components transverse to the east-west, 30°-210° and 150°-330° triangle sides, respectively; L is the side of the triangle; and A the area of the triangle.

Typical recordings of divergence during periods of large convective activity and stable conditions are shown in Fig. 6. Convergence of 10^{-2} sec^{-1} over periods of minutes is common during daytime. During the night, values of 5×10^{-4} sec^{-1} are normal. This value may be considered the upper limit of the noise level of the divergence measurement. In the comparison between divergence and vertical velocity, a 100-sec running average was used. The space-time average wind velocity was computed by using the wind components measured over two of the triangle sides. This, of course, gives a redundant estimate of the velocity as we have three pairs of legs on a triangle.

Using, for example, the east-west and 30°-210° pair, the horizontal space average wind speed $\bar{V}_s$ can be expressed in terms of the two components v_0 and v_{120} as

$$\bar{V}_s = \left[\left(\frac{2v_{120} + v_0}{\sqrt{3}} \right)^2 + v_0^2 \right]^{\frac{1}{2}},$$

and the direction α from which the wind is blowing as

$$\alpha = \tan^{-1} \left(\frac{v_0 \sqrt{3}}{2V_{120} + v_0} \right) + 180°.$$

Using the other pairs of the triangle, similar expressions are obtained.

The meteorological tower was instrumented to measure vector wind by the use of bivanes at five fixed levels: 31, 62, 93, 124 and 149 m. The acoustic sounder inside the triangle was pointing vertically, and its records were compared with the measured inflow into the triangle. All data, except the acoustic sounder data, were sampled once per second and recorded on digital tapes. The acoustic sounder data were recorded (both) on facsimile and analog tapes.

4. Results

a. Comparison of divergence and the acoustic sounder

Considerable evidence now exists that plume-like structure can be seen by an acoustic sounder (McAllister et al., 1969; Beran, 1971). Fig. 7 shows an acoustic sounder record and a divergence for predominately large convective activity. The dark portions on the sounder record correspond to thermal plumes and their height indicates the height of the plumes, while the white "gaps" are interpreted as area between plumes. The solid line is the divergence measured by the optical system. Convergence is upward on the figure.

The correspondence between the measured convergence and the plumes as seen by the acoustic sounder is mostly good, although some discrepancies can be seen especially after 1440 local time. Note that while the divergence is measured at a height of about 2 m above ground, the lowest height seen by the acoustic sounder is about 50 m, making an absolute comparison between the two systems difficult.
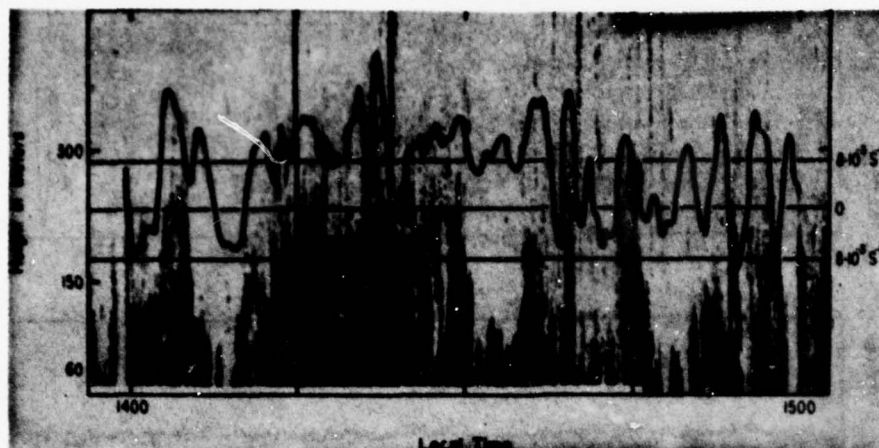
FIG. 7. Comparison between the plumes seen by the acoustic sounder and the flow into the triangle. Large plumes are associated with large convergence. The solid line is the divergence measured by the optical system.

b. Correlation of divergence and vertical wind

The vertical velocity is related to the divergence field through the equation of continuity as

$$\nabla_A \cdot V = -\frac{\partial w}{\partial z}.$$

Fig. 8 shows a typical set of cross-correlation curves between the divergence and the vertical wind and gradient on the tower during strong convective activity.

Because the tower is outside the triangle, the peak in the cross correlations does not occur at zero lag but is
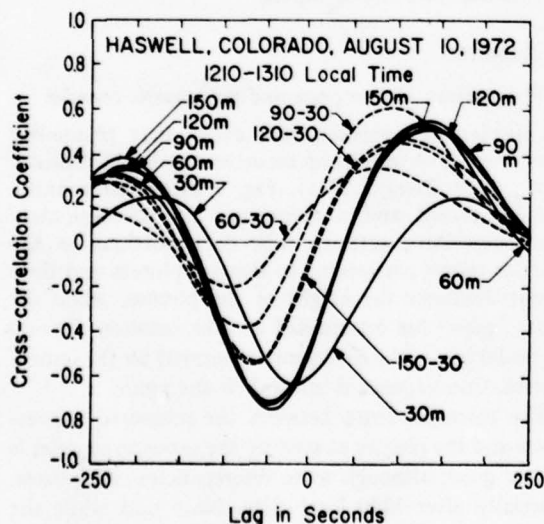

FIG. 8. Cross-correlation curves between divergence and vertical wind, and divergence and vertical wind gradient for the different levels on the tower. Solid lines are divergence vs vertical velocity and dotted lines divergence vs vertical wind gradient.

shifted in time corresponding to the travel time between the tower and the center of the triangle. For the case chosen the wind direction was along a line between the center of the triangle and the tower. The negative lag means that the divergence is lagged behind the vertical wind on the tower.

One of the interesting features in Fig. 8 is the difference in correlation between $\nabla_A \cdot V$ and $-\partial w/\partial z$, and between $\nabla_A \cdot V$ and w. From these curves, we see that in the case of plumes, the convergence into the plumes is more determined by the vertical wind than by the gradient of the same. These results seem to agree with Morton et al. (1956), who assumed that the entrainment into plumes was proportional to the upward velocity. It might be argued that this picture might have been different if we had had a measurement of the vertical wind at the same height as the divergence measurement. Due to the 100-sec running average, however, we are looking at a large population of plumes which should not differ much from 5 to 30 m, so we believe that our results give a reasonably correct picture.

Another interesting feature of these curves is the relative time shift between the peaks in the cross correlations for the vertical wind at the different levels indicating that the plumes or convective currents are tilted. The tilt is in the downwind direction. This corresponds to what Kaimal and Businger (1970) have reported for a single plume. The plumes are passing the four upper levels on the tower at about the same time but some 20–30 sec earlier than the lowest level (30 m).

In all the cases we have analyzed, the plumes were tilted in the lowest 60 m, whereas from 60 to 150 m almost no tilting was observed.

The third feature that should be observed in Fig. 8 is the periodicity in the cross-correlation curves indicating that there is a periodicity in the development of con-

vective currents in the boundary layer. The time between the two cross-correlation maxima, which might be interpreted as the period between a set of plumes, is 360 sec.

Panofsky (1973) has recently shown that the plumes seem to move with a speed close to the local wind. In this case the wind was about 1.5 m sec^{-1} at the height of the triangle, giving us a separation in space of about 540 m between every major set of plumes. This scale size seems to agree with what Ackerman (1967) has reported for convective clouds. She found scale sizes of 400–900 m. This periodicity was only found during large convective activity. During the morning and the evening hours correlation curves like curve B shown in Fig. 9 are typical. The magnitude of the correlation between $\nabla_h \cdot \mathbf{V}$ and w seems to change very little during the day, but the plumes are released more randomly with no outstanding size contributing to the cross correlation during the morning and evening hours.

c. Daily variation of the divergence

As shown in Fig. 6, a great difference exists between the divergence during day and night. In the morning and evening, we found that the flow was out of the triangle about 60% of the time. During heavier convective activity in the middle of the day, the flow was into the triangle 60% of the time. In the middle of the day peak values in convergence (10^{-2} sec^{-1}) were found over periods of 1–2 min. The standard deviation was normally in the order of 4×10^{-3} sec^{-1}.

d. Space average of wind velocity

As shown in Fig. 4, this technique measures the transverse space-averaged wind component. By com-
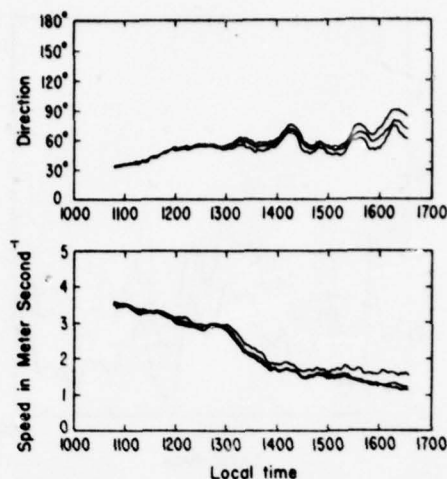
FIG. 10. A comparison of the three values of the wind vector determined from the laser triangle. Wind direction and speed are shown in the upper and lower parts of the figure, respectively. A 20-min running average has been applied to the data to smooth out the effect of convective activity.

bining two components as shown in Eqs. (2) and (3), we get the total horizontal wind vector. Since three components are available, these can be combined to give three values of the wind vector. By applying a 20-min running average to the data to smooth out convective activity and comparing these three values, we have a measure of the ability of the system to obtain the space-time averaged horizontal wind vector.

Fig. 10 shows plots of the three values of the wind vector for nearly 6 hr, with direction and speed shown in the upper and lower parts of the figure, respectively. For a wind speed higher than about 2 m sec^{-1}, we see that it makes little difference which two of the three components are used to calculate the horizontal wind vector. When the wind speed drops below about 2 m sec^{-1} the differences increase, very likely from several causes. Due to slight differences in the terrain along the triangle legs, irregular wind patterns can persist over the triangle and be more pronounced during light wind conditions. In addition, instrumental errors appear as a fraction of the full-scale wind setting chosen, which was 10 m sec^{-1} for the case shown. Recent modifications to the instrumentation have reduced this source of error.

Figs. 11 and 12 compare the wind speed and direction calculated from the component measurement and the same quantities measured at the 30-m level on the tower. All recordings are 10-sec averages. The wind recordings at the tower are shifted 40 sec in time to compensate for the travel time from the triangle to the tower. The differences in the wind speed magnitude are expected because of the difference in height above ground. Using the logarithmic wind profile to calculate the wind speed at the 30 m level from the wind speed measured with the optical technique, we obtain the
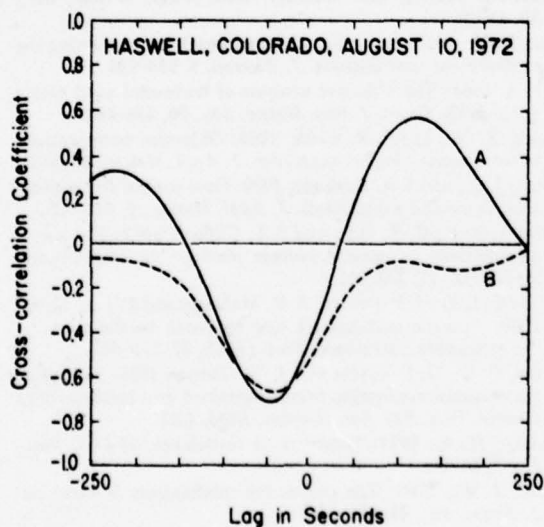

FIG. 9. Cross-correlation curves between divergence and vertical wind. The solid line is for high convective activity, and the dotted line for low convective activity.
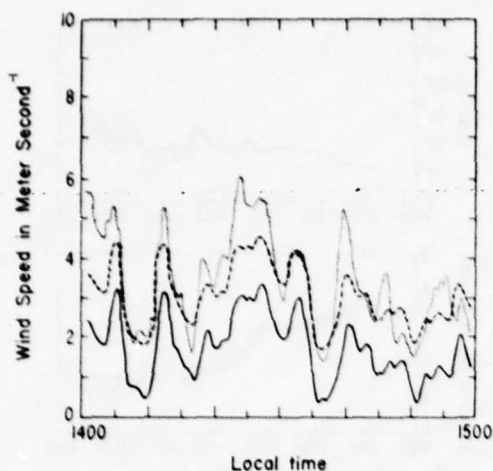
FIG. 11. Comparison of wind speed measured at the 30 m level on the tower (dotted line) with the wind speed calculated from the triangle measurement (solid line). The dashed line is the calculated logarithmic wind profile using a roughness parameter z_0 of 4 cm, and a friction velocity u_* of 20 cm sec^{-1}.

dashed line curve shown in Fig. 11. A roughness parameter z_0 and a friction velocity u_* of 4 cm and 20 cm sec^{-1}, respectively, were used. These values are regarded as reasonable for the type of ground cover and wind speed we encountered.

The correlation between the two types of measurements is very good. The larger variance of the wind measured at the tower is expected because this is a point measurement, while the optical wind measurement is an average both in time and space.
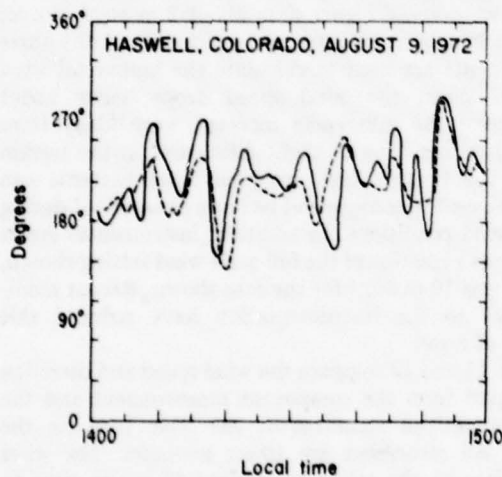

FIG. 12. Comparison of wind direction measured at the 30 m level on the tower (dotted line) and that calculated from the laser wind measurement (solid line).

5. Conclusion

It has been shown that a wind measuring system using three separate optical systems, each consisting of a 3 mW He-Ne laser and two photodiode receivers, forming a equilateral triangle, is successful in measuring the divergence over a small enclosed area. By using two of the optical systems, we can get a space-averaged horizontal wind vector. The thermal plumes as seen by the acoustic sounder and the convergence compare well. The correlation between the divergence and the vertical wind measured on the tower shows that the entrainment into plumes is proportional to the vertical velocity.

During periods with large convective activity a certain periodicity in the development of plumes is found.

REFERENCES

Ackerman, Bernice, 1967: The nature of the meteorological fluctuations in clouds. *J. Appl. Meteor.*, **6**, 61–71.
Bellamy, J. C., 1949: Objective calculations of divergence, vertical velocity and vorticity. *Bull. Amer. Meteor. Soc.*, **30**, 45–49.
Beran, D. W., 1971: Acoustics: a new approach for monitoring the environment near airports. *J. Aircraft*, **8**, 934–936.
Eddy, A. 1964: The objective analysis of horizontal wind divergence fields. *Quart. J. Roy. Meteor. Soc.*, **90**, 424–440.
Endlich, R. M., and J. R. Clark, 1963: Objective computations of some meteorological quantities. *J. Appl. Meteor.*, **2**, 66–81.
Kaimal, J. C., and J. A. Businger, 1970: Case studies of a convective plume and a dust devil. *J. Appl. Meteor.*, **9**, 612–620.
Lawrence, R. S., G. R. Ochs and S. F. Clifford, 1972: The use of scintillations to measure average wind across a light beam. *Appl. Opt.*, **11**, 239–243.
McAllister, L. G., J. P. Pollard, A. R. Mahoney and P. J. R. Shaw, 1969: Acoustic sounding—a new approach to the study of the atmospheric structure. *Proc. IEEE*, **57**, 579–587.
Morton, B. R., G. I. Taylor and J. W. Turner, 1956: Turbulent gravitational convection from maintained and instantaneous sources. *Proc. Roy. Soc., London*, A234, 1–23.
Panofsky, H. A., 1973: Structure of turbulence. *IFYGL Bull.*, No. 7, 48–49.
Telford, J. W., 1966: The convective mechanisms in clear air *J. Atmos. Sci.*, **23**, 652–666.

DISPERSION AND SPECTRA OF GRAVITY WAVES PROBABLY GENERATED BY A CONVECTIVE STORM[†]

By

A G Kjelaas[*]
Norwegian Defence Research Establishment
P O Box 25 — N-2007 Kjeller, Norway

E E Gossard, J M Young
NOAA/ERL, Wave Propagation Laboratory
Boulder, Colorado, USA

and

W R Moninger
Coe College
Cedar Rapids, Iowa, USA

DISPERSION AND SPECTRA OF GRAVITY WAVES PROBABLY GENERATED BY A CONVECTIVE STORM

By

A G Kjelaas, E E Gossard, J M Young and W R Moninger

ABSTRACT

In this paper we describe a case study of progressive gravity waves in the troposphere. We deduce their propagation speed and direction, and their dispersive characteristics, from surface spectra of wind and pressure. We compare the results with direct measurements of the waves made over an array of spaced pressure sensors using cross spectrum techniques and an algorithm developed by one of us (Young). The agreement is very satisfactory and demonstrates the feasibility of monitoring atmospheric wave conditions in almost real time using only sensors (high quality) in use at standard weather observation stations.

The waves in the case we describe were highly dispersive and apparently were generated by a violent thunderstorm some 100 km west of the site of observation.

1   INTRODUCTION

Atmospheric gravity waves and convective activity are important contributors to the atmospheric pressure spectrum in the band of periods from about 1 minute to 1 hour (Gossard, 1960). The form of the spectrum of displacement of the density surfaces (or isentropes), and the dispersion characteristics of propagating disturbances reveal much about the mechanism of their generation (Gossard, 1974). In this paper we measure the spectrum and the dispersion of gravity waves apparently generated by a severe convective storm on 8 August 1972 in southeastern Colorado. The wave spectra and the dispersion of the waves we will discuss are dramatically different from the spectra and dispersion of waves analyzed by Gossard and Sweezy (1974) which they concluded were generated by dynamic instability associated with shear in the middle troposphere.

A method devised by Gossard and Sweezy (1974) will be used for determining the dispersive characteristics of the observed waves, and we will compare it with direct measurements of the speed and direction of wave components across an array of spaced pressure sensors. For the latter analysis we use the digital techniques and computer algorithm devised by one of us (Young) to carry out a cross spectral analysis between spaced sensors in such a manner that the "beam" of the array is effectively steered, or swept, continuously through 360 deg of azimuth.

In addition to the usual temporal filtering commonly used to extract mesofrequency information, we have used sensors capable of spatially filtering the atmospheric spectrum, and in this paper we will discuss the merits of such spatial filtering for sorting out the contribution of atmospheric waves for analysis. We will show that by use of such a spatial averaging of the wind field, the large mesoscale features in the wind spectrum can be effectively extracted from the turbulence "noise".

2   ANALYTICAL TECHNIQUES

In the method of Gossard and Sweezy (1974), the spectra of surface pressure and wind are combined to obtain the "spectrum" of intrinsic phase velocity of waves in the mid-frequency band of the spectra of atmospheric properties. Within the constraints of

the linearized theory and the Boussinesq approximation, they point out that (e g, see Gossard and Hooke, 1974)

$$P = \rho_s \left(\frac{\omega}{k}\right)^2 \frac{\partial \zeta}{\partial z} \qquad \text{and} \qquad \frac{\omega}{k} = \frac{1}{\rho_0} \frac{P}{U} \tag{1a,b}$$

In these equations

$$U, \zeta = [\rho_0(z)/\rho_s]^{1/2} u, \eta \qquad \text{and} \qquad P = [\rho_0(z)/\rho_s]^{-1/2} p$$

where u, p, and η are, respectively, wave perturbations of the horizontal wind, pressure and isentropic surfaces; $\rho_0(z)$ is the unperturbed density and ρ_s is the density at some reference level such as the earth's surface. The wave frequency relative to an observer moving with the mean flow is ω (the intrinsic frequency) and the wavenumber $k = 2\pi/\lambda$ where λ is wavelength. Then the displacement spectrum at height H within a surface layer of constant Väisälä Brunt frequency N and constant wind is related to the pressure spectrum at the surface by

$$E_{\zeta_H}(f) = \left[\frac{H}{\rho_s\left(\frac{\omega}{k}\right)^2}\right]^2 B^2 E_{P_0}(f) \tag{2}$$

where B is $\sin n_1 H/n_1 H$ or $\sinh \gamma_1 H/\gamma_1 H$ depending on whether N_1/ω is greater than or less than unity. The dispersion equation for waves of infinitesimal amplitude relating n to the wave frequency ω and wavenumber k through the Väisälä-Brunt frequency $N = \sqrt{(g/\theta) \, d\theta/dz}$ (where θ is the potential temperature) is essentially (see Gossard and Hooke, 1974)

$$n = i\gamma = k \left[\left(\frac{N}{\omega}\right)^2 - 1\right]^{1/2} \tag{3}$$

for waves whose vertical wavelength is small compared with the atmospheric scale height.

Also, the relation

$$\left[\frac{\omega}{k}(f)\right]^2 = \rho_0^{-2} \frac{E_P(f)}{E_U(f)} \tag{4}$$

provides a measure of the wave dispersion when the spectra contain an important wave contribution. The wind component U must be extracted vectorially from fluctuations of the total wind as illustrated in Figure 1. This is accomplished by choosing a suitable numerical low-pass filter to apply to wind speed and direction, thus separating the mean wind from the total wind. The same low-pass filter is applied to the pressure record. However, our pressure sensing system had its own high-pass filter, with a time constant of 50 sec, whose effect had to be removed from the final spectrum. A low-pass numerical filter was chosen such that a perturbation of 15 min period would have its
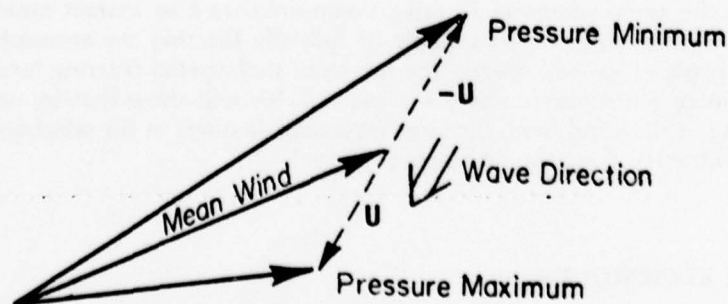

Figure 1   Vector diagram for extracting the wind component U along the wave from fluctuations of the total wind

amplitude reduced to one-third the true value. The time series of wind and pressure were sampled every second and then averaged over 20 sec intervals.

Young's method of processing data from spaced sensors is to azimuthally steer the array beam in either the time or frequency domains. It differs from other algorithms such as that of Mach and Smart (1972) primarily in having greater flexibility in choice of bandwidth when signal velocity is approximately independent of frequency as in the case of acoustic waves. This is accomplished by processing in terms of the wave "slowness" (defined as the inverse of velocity) rather than processing in frequency-wave-number space. Varying the frequency bandwidth has little influence on the average within the band when "slowness" is relatively constant over the band, so the algorithm is adaptive in choosing an optimum trade-off between confidence and spectral resolution. When applied to gravity waves, the assumption of little dispersion is no longer necessarily valid as we shall see when results are discussed.

3 OBSERVATIONAL TECHNIQUES

The pressure sensors used in this study were essentially like that described by Bedard (1971), except that the filter amplifiers producing the various bandpasses shown in his figure 3 were not employed. Therefore the high frequency response was practically unlimited (as far as gravity waves are concerned) and the high-pass characteristic can be described by the single time constant of 50 sec. Each presssure sensor had 30 m of hose attached, into which hypodermic needles, used as orifices, were inserted at intervals of 1.5 m. The hose serves to spatially filter out small scale turbulent inhomogeneities in the pressure field. The total pressure array consisted of a small array within a larger array as shown in Figure 2. The small array was designed primarily to look at relatively small
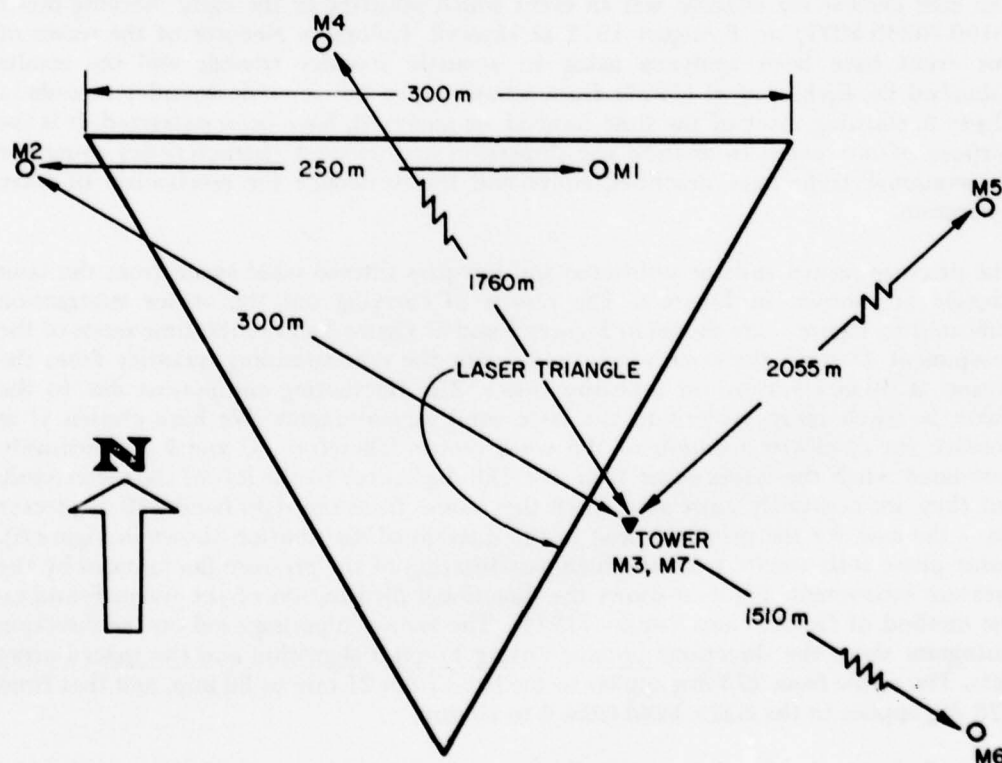

Figure 2 *Layout of the experimental configuration*
   The solid triangle is the laser triangle. Points marked M1, M2, M3 are the small microbarograph array, while M4, M5, M6, M7 denote the larger array. M7 is 20 m from the tower base.

scale features within the boundary layer, and the large array was designed to observe larger scale features such as infrasound or long waves higher in the atmosphere. In the present study, additional spatial filtering of the pressure field was achieved by averaging pressure over the small array of sensors to obtain the spectrum of pressure for use in Eqs (2) and (4).

The anemometers used in the present study were bivanes with a high frequency response limited to approximately one Hz. However, our primary source of wind data was a unique system designed and built by G Ochs and more completely described by Lawrence *et al* (1972) and Kjelaas and Ochs (1974). The system uses a laser path to measure the average wind (somewhat weighted toward the center of the path) transverse to the path by measuring the velocity of the scintillation pattern at the receiver end. Clearly, only two such paths are needed to obtain a value of the total horizontal wind. However, the system was used in a triangular configuration so that horizontal mass convergence and divergence could be measured (Kjelaas and Ochs, 1974). This is also a suitable configuration for obtaining wind spatially averaged over the area of the triangle. The laser triangle is shown in Figure 2.

The results of the analysis, using the spatially averaged pressure and winds as described above, were compared with results using point sensors. The advantage of using the laser winds was especially evident, and values of U obtained from bivane and from the laser triangle are shown for comparison in Figure 4. Apparently the removal of small scale turbulence "noise" by the spatial filtering, accomplished by laser path averaging of the wind field, significantly improves the wave signal-to-noise.

4   EXPERIMENTAL RESULTS

The case chosen for analysis was an event which occurred in the early morning hours (0100–0230 MDT) on 8 August 1972 at Haswell, Colorado. Records of the waves of this event have been analyzed using an acoustic sounder triangle and the results published by Kjelaas *et al* (1974) from whose paper the acoustic sounder records in Figure 3, showing most of the time interval we analyzed, have been extracted. It is the purpose of our paper to analyze the dispersion and spectral characteristics using the observational techniques described above and try to deduce the mechanism of wave generation.

The pressure record and the unfiltered and low-pass filtered wind speed from the laser triangle are shown in Figure 4. The results of carrying out the vector subtraction indicated in Figure 1 are shown in Figures 5 and 6. Figure 5 shows the time series of the component U from the laser winds along with the corresponding quantity from the bivane at 30 m elevation on a nearby tower. The fluctuating component due to the waves is much more evident in the laser wind measurements. We have chosen U as positive for clockwise rotation of the wind vector. Therefore, U and P are positively correlated when the waves come from the 180 deg sector to the left of the mean wind, but they are negatively correlated when they come from the right-hand 180 deg sector (as is the case for the principal peak in the directional distribution shown in Figure 6). Some phase shift results from the high-pass filtering of the pressure fluctuations by the pressure instrument. Figure 6 shows the directional distribution of the waves found by the method of Gossard and Sweezy (1974). The arrows superimposed on the direction histogram show the directions obtained using Young's algorithm and the spaced array data. The arrow from 270 deg applies to the band from 21 min to 80 min, and that from 225 deg applies to the entire band from 4 to 80 min.

Figure 7 shows the dispersion plot of phase velocity vs frequency by the method of Gossard and Sweezy, together with the results of Young's analysis from spaced array data shown for frequency bands indicated by the bars. The spacing of elements in the array produces a high-frequency cut-off in the array spectra. The excellent agreement
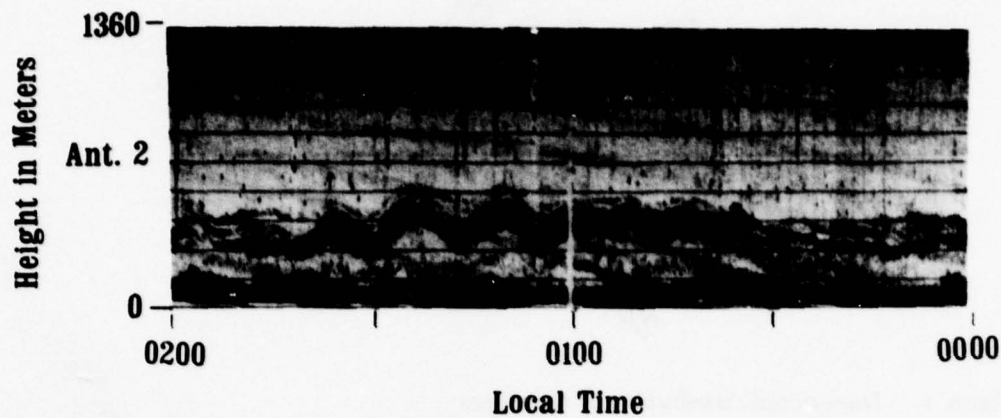
HASWELL, COLORADO
August 8, 1972

Figure 3   *Acoustic sounder record of part of the event analyzed in this paper*
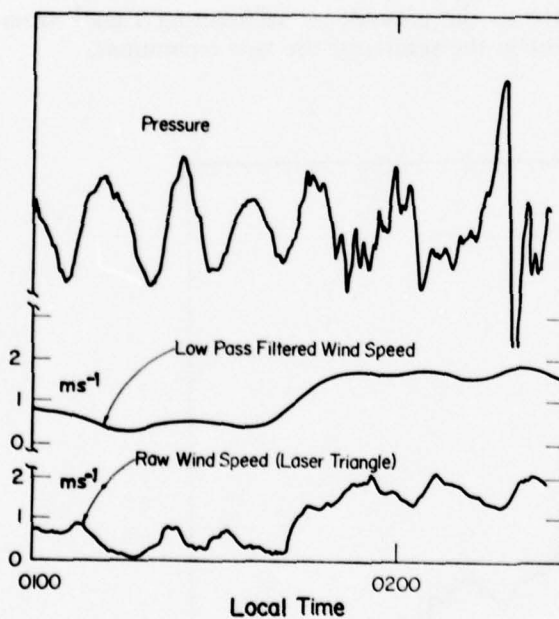LT is Mountain Daylight Time. To convert to UT add 6 hours to LT. (From Kjelaas *et al* (1974)).

Figure 4 *Pressure recording together with the low-pass filtered and unfiltered laser wind*
No scale is included for pressure since the instrument's filter characteristic has not been removed.
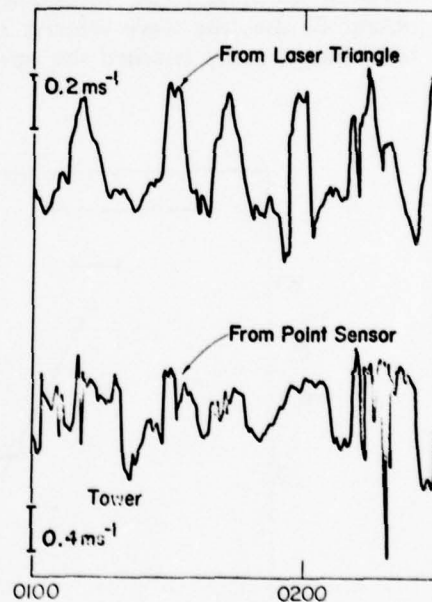
Figure 5 *Wind component U along the wave direction*
Upper curve is obtained using the laser triangle, while lower curve is from the bivane at 30 m on a nearby tower. Power density of frequencies greater than $\sim 2 \times 10^{-3}$ Hz is about two orders of magnitude down from the peak in the power spectrum, so such points probably have no significance.
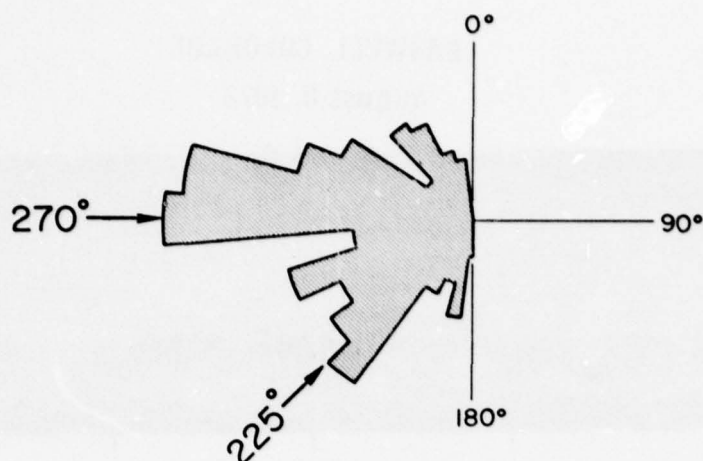
Figure 6   Directional distribution of the waves

is a very convincing argument for the validity of both techniques. At a frequency of 2×10^{-3} Hz, the power in the spectrum (see Figure 10) has diminished by two orders of magnitude from the peak power. Thus we do not consider the velocities in Figure 7 to be significant at frequencies higher than about 2×10^{-3} Hz. During this wave event, the average surface winds were very light (about 1 ms^{-1}) and were mostly between north and east in opposition to the wave direction. We have attempted to obtain C, the true wave velocity relative to the ground, by subtracting 1 ms^{-1} from ω/k. This actually lessened the agreement in the results of the two techniques.
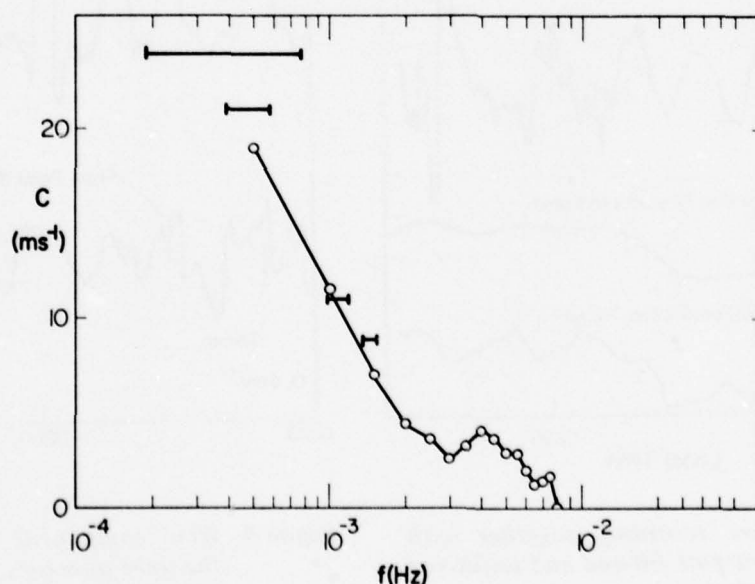

Figure 7   Phase velocity vs frequency
The horizontal bars are the phase velocities for different frequency bands found by applying Young's technique to the large microbarograph array.

Figure 8 shows the plot of ω vs k. On this plot the slope of the line from the origin to any point on the curve represents the intrinsic phase velocity, and the slope of the tangent to the curve is the group velocity given by $d\omega/dk$.
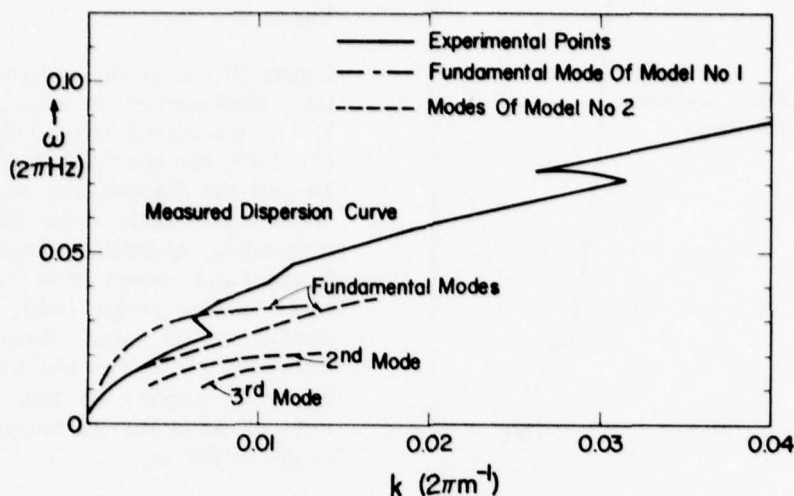

Figure 8   *Intrinsic frequency as a function of the wavenumber*
Only the fundamental mode is shown for model no.1.

Figure 9a,b,c shows the RAWINSONDE data obtained at 0457 MDT (the sounding nearest in time to the wave event). Unfortunately, the sounding does not well represent the lowest layers at the time of the waves, because a high surface wind sprang up at about 0400 MDT apparently due to outflow from the cool downdraft of a thundershower occurring locally at about that time. The high wind at the surface mixed the air within the radiation inversion and elevated it. We have used the surface wind and temperature data at the time of the wave event and the temperature and wind data at the top of a nearby 151 m tower (see Figure 2) to attempt to correct the sounding data
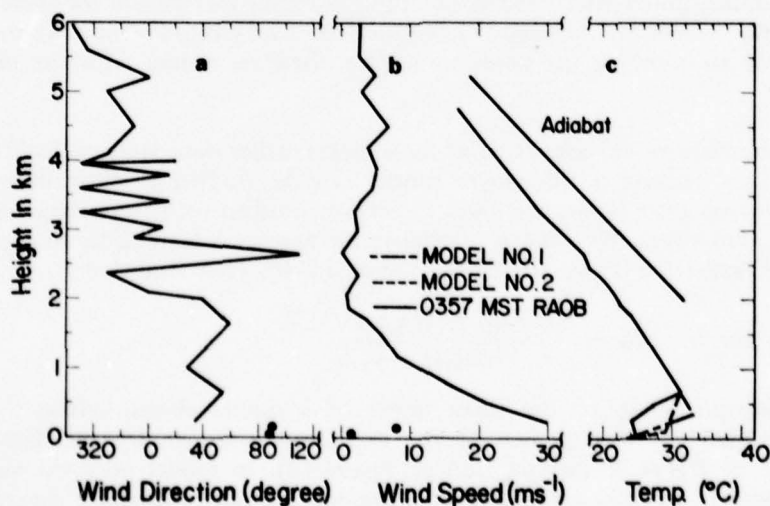

Figure 9   *Radiosonde at 0457 MDT*
The circles shown are the wind and temperature data from the tower at the time of the wave event. The various atmospheric models discussed are shown as dashed curves.
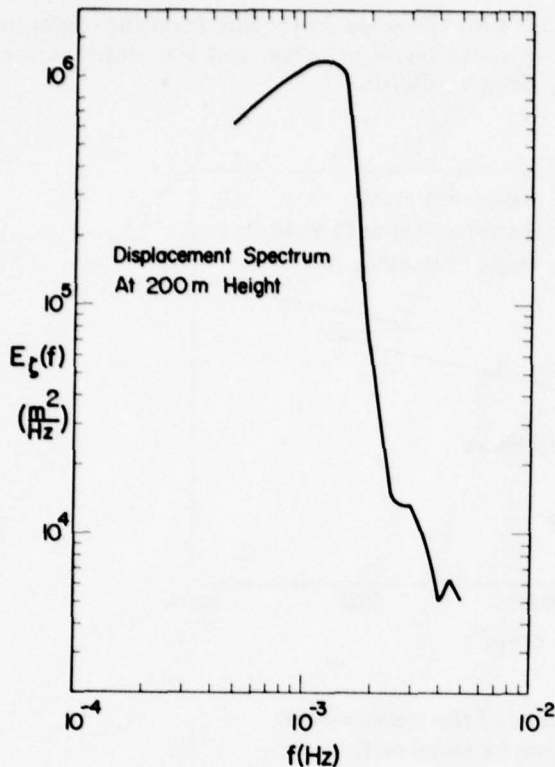
Figure 10 shows the spectrum of layer displacement at a height of 200 m calculated from equation (2). Both the spectrum in Figure 10 and the dispersion in Figure 8 differ significantly from the corresponding quantities found by Gossard and Sweezy from the data taken at San Diego, Calif, under conditions of wind shear and instability aloft. The spectrum in Figure 10 implies an rms amplitude of 38 m for the waves at a height of 200 m.

back to the time of the event. The values are shown as circles, and two atmospheric models we analyze in the next section are shown as dashed and dash-dot curves in Figure 9c.

Figure 10   Spectrum of layer displacement at a height of 200 m

5   COMPARISON WITH MODELS

The light winds aloft shown in Figure 9 and the relatively low surface and tower winds at the time of the event (compared with the wave velocity of about $10 \, ms^{-1}$ at the spectrum maximum) imply that shear is not the generating mechanism for these waves. Furthermore, the waves are propagating against the background winds. Therefore it seems reasonable to compare the predictions of a shearless model with the observed dispersion.

We adopted a shearless model consisting of three layers rather than more realistic models with many layers because a three-layer model can be studied analytically whereas models with four or more layers are more effectively studied using numerical methods on high speed computers. We used a normal mode approach leading to an eigenvalue equation whose derivation is given by Gossard *et al* (1970). They find that

$$n_2 \cot 2n_2 \, \Delta H = \frac{n_2{}^2 - n_1 \, \gamma_3 \, \cot n_1 H}{n_1 \, \cot n_1 H + \gamma_3} \tag{5}$$

where the subscripts apply to the three layers of a model shown schematically in Figure 12. Equation (5) was applied to the two models shown by the dashed and dash-dot curves in Figure 9c (see caption of Figure 12). In model no. 1 the thickness $2\Delta H$ of the middel layer is zero so it is a two-layer model for which equation (5) becomes (see Gossard and Hooke, 1974)

$$\tan\left(kH\sqrt{\left(\frac{N_1}{\omega}\right)^2 - 1}\right) = -\frac{\sqrt{\left(\frac{N_1}{\omega}\right) - 1}}{\sqrt{1 - \left(\frac{N_3}{\omega}\right)^2}} \tag{6}$$

The resulting dispersion curves for the two models are shown plotted on Figure 8 for comparison with the observed values. To avoid confusion from too many curves on the plot, only the fundamental mode of model no. 1 has been plotted, but the second and third modes are shown for the three-layer model.

Model no. 1 provides the best fit to the gross features of the observed dispersion curve, but model no. 2 fits the low frequency portion of the curve ($\omega < 0.02$) almost exactly. In actual fact, if the waves have propagated some 100 km from the storm area, the path was undoubtedly variable, representing combinations of the various models here considered. For frequencies $\omega < N_3$, real roots to equation (5) do not exist. This means that such waves "leak" energy upward away from the stable layers.

The important fact to note is that the observed waves are strongly dispersive as would be expected from the shearless models. If the waves had been generated by dynamic instability at a shear layer, the unstable irregularities would all travel with the mean wind speed at the center of the shear layer if the model is symmetrical with infinite upper and lower layers. If we consider a three-layer model in which the lower layer is not of infinite depth, those wave lengths long compared with its depth will no longer travel with exactly the speed of the mean wind (see Gossard, 1974), but the effect is
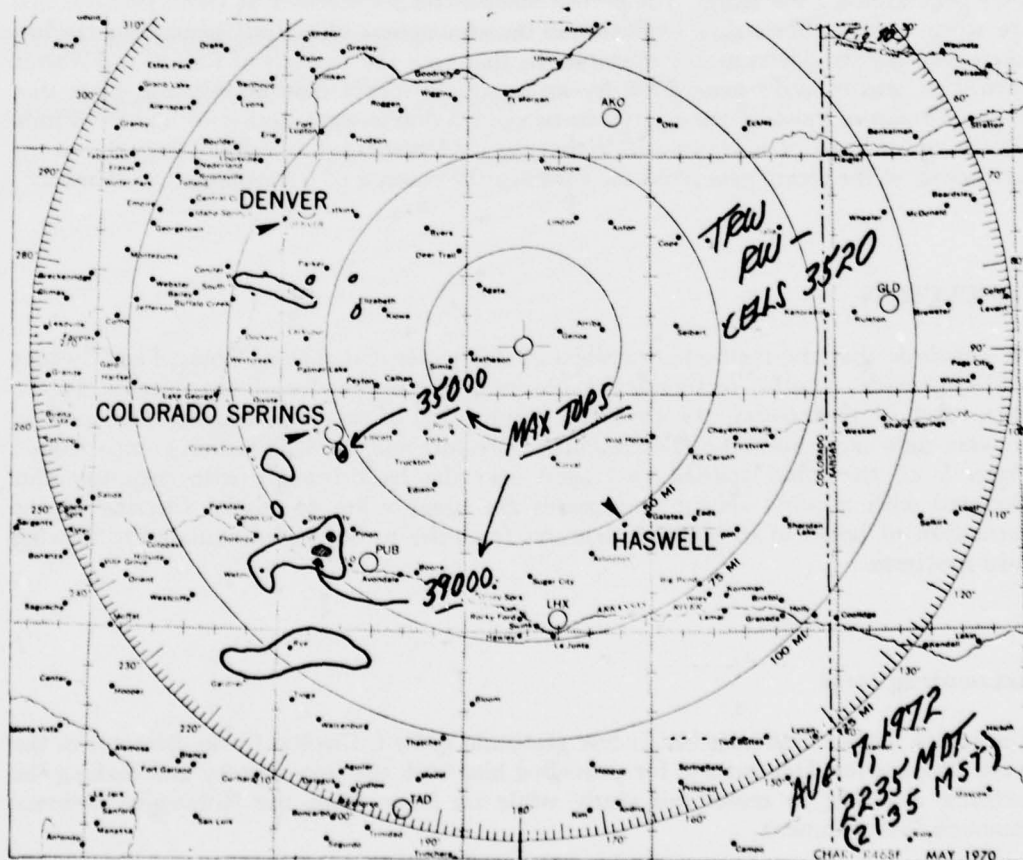

Figure 11 Radar weather map at 2135 MST (2235 LT) obtained using the radar at Limon, Colorado
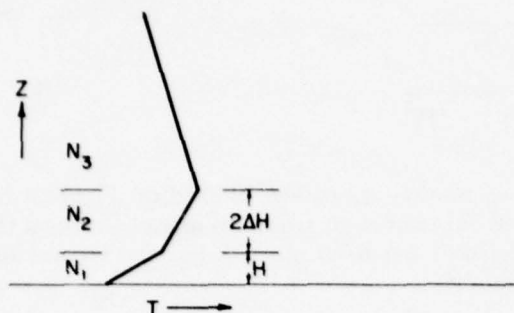
Figure 12 *The three-layer model*

Model no. 1 (dash-dot curve in Figure 8c) is a two-layer model, i e, $\Delta H = 0$, in which $N_1 = 0.0354$, $N_3 = 0.0111$ and $H = 200$ m. In model no 2 (dashed curve in Figure 8c), $N_1 = 0.050$, $N_2 = 0.0202$, $N_3 = 0.0111$, $H = 100$ m, $2\Delta H = 600$ m.

small for the wavenumber range we consider here. The waves studied by Gossard and Sweezy (1974) displayed the non-dispersive character to be expected of wave generation by shear. The highly dispersive nature of the waves we have studied in this paper implies a different mechanism of generation. In addition, Figure 9 shows that the small shear that might exist during the period of the event would lead to waves propagating from the north-easterly direction. They were actually propagating from the west through south-west sector (as seen in Figure 6) with a group velocity of about 6 ms^{-1} at frequencies corresponding with the maximum in energy of the spectrum shown in Figure 10. If we look 100 km to the west of Haswell on the radar weather map shown in Figure 11 taken at 2135 MST (2235 MDT) obtained by the NWS using the WSR 57 radar at Limon, Colorado, we find a violent thunderstorm near Pueblo, Colorado, extending above 39 000 ft (11.9 km). By 2337 MDT the tops exceeded 41 000 ft (12.5 km). It seems very likely that the waves discussed in this paper were generated by the storm. The precise mechanism is uncertain. It seems possible that the storm may act like a slow explosion in the atmosphere effectively generating the low frequency gravity waves in our example. In that case the analysis of Ramm and Warren (1963) of gravity wave generation by an impulsive source may be relevant. Note that Figure 10 shows most of the energy to be centered at a wave period of about 14 min. On the other hand, it is very possible that the cool gust front associated with the strong downdraft of the storm generated the waves in the manner of a travelling disturbance.

6 CONCLUSION

We conclude that the methods described in this paper and that of Gossard and Sweezy (1974) provide a useful technique for observing the properties of waves in the atmosphere and of diagnosting the probable mechanism of wave generation. The method requires only single station measurements of pressure and wind. However, comparison in Figure 5 of the wind spatially averaged over the laser triangle with measurements obtained with a point sensor emphasizes the great value of spatial filtering in the extraction of large (or meso) scale features from the turbulence dominated total wind field spectrum.

References

Bedard, Alfred J, Jr, 1971. Seismic response of infrasonic microphones, *J of Res Natl Bu of Stand,* 75C(1), 41–45.

Gossard, E E, 1960. Spectra of atmospheric scalars, *J Geophys Res,* 65, 3339–3351.

Gossard, E E, 1974. Dynamic stability of an isentropic shear layer in a statically stable medium, *J Atmos Sci,* 31(2), (in press).

Gossard, E E, Richter, J H, and Atlas, D, 1970. Internal waves in the atmosphere from high resolution radar measurements, *J Geophys Res,* 75, 903–913.

Gossard, E E and Hooke, W H, 1974. Waves in the Atmosphere, Elsevier, Amsterdam (in press).

Gossard, E E and Sweezy, W B. Spectra of waves in the atmosphere, (in press *J Atmos Sci*).

Kjelaas, A G, Beran, D W, Hooke, W H, and Bean, B R, 1974. Observation of waves in the boundary-layer using an array of acoustic sounders, (in press *J Atmos Sci*).

Kjelaas, A G and Ochs, G R, 1974. Study of divergence in the boundary layer using optical propagation techniques, *J Appl Meteorol,* 13, no. 2, 242–248.

Lawrence, R S, Ochs, G R, and Clifford, S F, 1972. The use of scintillations to measure average wind across a light beam, *Appl Opt,* 11, no. 2, 239–243.

Mack, H and Smart, E, 1972. Frequency domain processing of digital microbarograph array data, *J Geophys Res,* 77(1), 488–490.

Ramm, P and Warren, F W G, 1963. Gravity-wave dispersion under wind shear in two model atmosphere, *Q J R Meteorol Soc,* 89, 349–359.

WAVES OBSERVED IN THE PLANETARY BOUNDARY LAYER USING AN ARRAY OF ACOUSTIC SOUNDERS[*]

A G Kjelaas[1]
D W Beran[2], W H Hooke[2], and B R Bean[3]

[1] *Norwegian Defence Research Establishment, Kjeller, Norway*

[2] *Wave Propagation Laboratory, NOAA Environmental Research Laboratories, Boulder, Colorado 80302*

[3] *Office of Weather Modification, NOAA Environmental Research Laboratories, Boulder, Colorado 80302*

WAVES OBSERVED IN THE PLANETARY BOUNDARY LAYER USING AN ARRAY OF ACOUSTIC SOUNDERS

A G Kjelaas
D W Beran , W H Hooke , and B R Bean

ABSTRACT

Three acoustic sounders, with antennas having vertically-pointed beams located at the vertices of a triangle about 300 m on a side, have been used successfully to calculate horizontal phase velocities of gravity waves in the lowest 1000 m of the atmosphere. The wave parameters obtained were compared with those obtained by an array of microbarographs. The results from the two independent techniques agreed well in all cases where the waves were detected by both methods. However, the acoustic-sounder array was also able to detect gravity waves propagating in an inversion overlying the convective boundary layer that were undetected by the microbarograph array because of wave attenuation in the convective region.

Wave-associated vertical-velocity fluctuations inside the undulating structure were measured using Doppler techniques to an accuracy of about ± 0.1 m sec^{-1}. Vertical-velocity fluctuations of about ± 0.5 m sec^{-1} were measured inside one wave with displacement amplitude of 120 m and wavelength of 5.5 km. From wave-associated vertical-velocity fluctuations, displacement amplitude, and wave period, we could calculate the wind-speed component along the wave propagation direction. This calculated wind-speed component agreed reasonably well with the value derived independently from radiosonde measurements.

1. Introduction

During the summer of 1972, the staff of NOAA's Wave Propagation Laboratory (WPL) mounted an experimental program at the Haswell field site in Colorado lasting several weeks. During the observing period, this area was characterized by a typical High Plains meteorological regime: strong radiative cooling at night and strong heating and convective activity during the day. The program had the dual objectives of (1) checking the operation of a variety of remote sensing systems and calibrating them against data gathered from a 150-m instrumented meteorological tower, and (2) studying the Haswell atmospheric boundary layer.

Included among the remote-sensing systems and meteorological instruments were three acoustic echo sounders and an array of microbarographs. The acoustic echo sounders operate like sonars; they transmit acoustic pulses and detect the echoes resulting from boundary-layer turbulent wind and temperature fluctuations (Tatarski, 1961; Monin, 1962). In this way, these sounders can measure boundary-layer turbulence intensity (e g Little, 1969; Bean, 1971; Emmanuel et al, 1972; Beran et al, 1973; McAllister, 1968) as a function of height and time, as well as the three components of the boundary-layer wind, which can be determined from the Doppler shift of the acoustic echoes when two of the three antenna beams are directed at angles off the vertical (Beran et al, 1971, 1973; Beran and Clifford, 1972). The microbarographs supported the remote-sensing studies of boundary-layer gravity waves, by measuring wave-associated pressure fluctuations at the earth's surface. From these records we determined wave parameters such as wave period, horizontal wavelength, phase velocity and azimuth of propagation (for illustrations of previous studies see , e g, Hooke et al, 1972, Beran et al, 1973).

During most of the observing period, the acoustic echo sounder data were gathered primarily to evaluate the relative merits of various antenna configurations in Doppler wind measurements. However, we were also interested to see whether we could operate the sounders in a mode analogous to that of the microbarograph array in order to study boundary-layer wave motions. To test this possibility, we operated the sounders for short intervals several hundred meters apart with all beams directed

vertically. Then to determine horizontal wavelengths, wave phase speeds, and propagation directions, we used the cross-correlation between corresponding features of the acoustic echo returns recorded by the three sounders (i e, the cross-correlation between the height—time echo intensity patterns), and the time lags required to maximize this cross correlation. These values were compared with those obtained from the microbarograph cross-correlation analysis as well as with those obtained by using the so-called impedance relation (Gossard and Munk, 1954), which gives the wave phase speed and direction from an analysis of the wave-associated pressure and velocity fluctuations measured at a single point.

In this paper, we summarize the results of using an array of three vertically-pointing acoustic echo sounders in calculating phase velocity, period, and, hence also horizontal wavelength of gravity waves. The results illustrate the advantages and limitations of this application of acoustic echo sounding. In addition, we show that from sounder measurements of (1) wave period, (2) wave-associated vertical-velocity perturbations (as revealed by Doppler shifts of the acoustic echo returns), (3) vertical parcel-displacement perturbations (as revealed by fluctuations in height of the strata of strong echo returns), and (4) horizontal wavelength (calculated from measurements of wave period and phase velocity), we can determine the mean wind speed component in the direction of wave propagation. We can, therefore, check the data still further for consistency by comparing the value of the mean wind speed calculated in this manner with that measured directly from a radiosonde and on the tower. Thus we have demonstrated in principle that acoustic echo sounders can use boundary-layer gravity waves as tracers in wind profiling.

2. The Experiment

The experimental configuration is shown in Fig 1. The points marked A, B, and C are the positions of the three acoustic echo sounders, which form a right triangle with legs roughly 300 m in length. The points marked M1, M2, and M3 denote the positions of the three microbarographs and T the location of the 150 m meteorological tower. This size and configuration was adequate for the gravity-wave studies here; however, to study larger-scale waves with higher phase velocities, we would have needed a larger triangle.
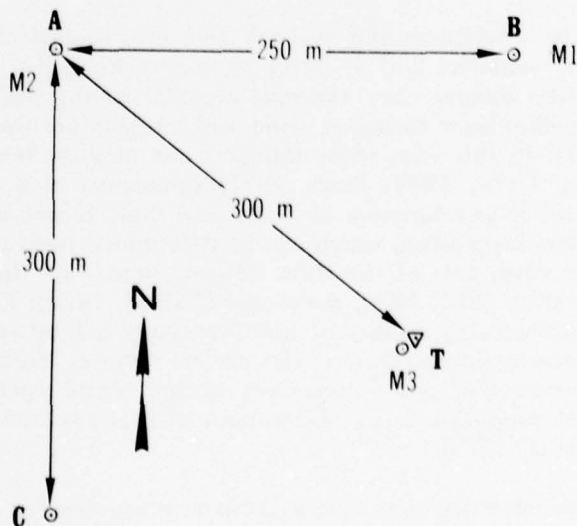

Figure 1 The layout of the experimental configuration. Points marked A, B, C, show the positions of the three acoustic echo sounders, and M1, M2, M3 the microbarographs.

PEAK POWER	10 W (ACOUSTIC)
PULSE WIDTH	100 m sec
PULSE REPETITION FREQUENCY	0.125 sec^{-1}
MAXIMUM RANGE	1360 m
CARRIER FREQUENCY	VARIABLE FROM 1750–2750 Hz
ANTENNA DIAMETER	152 cm
ANTENNA BEAMWIDTH	±5° TO 3 dB POINTS
BEAM DIRECTION	VERTICAL
RECEIVER BANDWIDTH	100 Hz

Table 1   Acoustic Echo Sounder Parameters

The three sounders, A, B, and C, were operated at center frequencies of 2750 Hz, 1750 Hz, and 2250 Hz, respectively, in order to avoid cross talk. The other sounder parameters are given in Table 1. Both the intensity of the backscattered energy and the Doppler frequency shift for each sounder were recorded on analog-tapes and digitized at a sampling rate of 62.5 sec^{-1}. In addition, facsimile recordings were made of the acoustic echo returns as functions of boundary-layer height and time. The tower was instrumented to measure wind and temperature at 30 m, 60 m, 90 m, 120 m, and 150 m; and to measure wave-associated pressure fluctuations at 90 m and 150 m. Radiosonde wind and temperature profiles were also obtained.

3. Theory of Wind Speed Determination from Gravity-Wave Observations

For any fluid motion the vertical parcel velocity w is instantaneously related to the vertical parcel displacement ζ by

$$w = \frac{D\zeta}{Dt} \tag{1}$$

where D/Dt denotes the time derivative following the parcel motion. That is,

$$\frac{D}{Dt} \equiv \frac{\partial}{\partial t} + \vec{u} \cdot \vec{\nabla} \tag{2}$$

so that for a sinusoidal wave of frequency ω (as measured by an observer fixed with respect to the ground) and wave vector $\vec{k}$, and of perturbation amplitude,

$$\frac{D}{Dt} = \omega - \vec{k} \cdot \vec{U}_o \equiv \Omega \tag{3}$$

The frequency Ω is the so-called "intrinsic" wave frequency, i e, the wave frequency that would be measured by an observer moving, relative to the ground, with the background wind velocity U_o. In general $U_o = U_o(z)$ and $\Omega = \Omega(z)$ where z is the height. Thus, at any height z, we have the relation

$$w^*(z) = \Omega(z)\,\zeta^*(z) \tag{4}$$

where the asterisks denote *amplitudes* of the wave-associated fluctuations. We have then that

$$U_{ok}(z) = \frac{\omega}{k} - \frac{w^*(z)}{k\zeta^*(z)}$$

$$= \frac{\omega}{k}\left(1 - \frac{w^*}{\omega\zeta^*}\right) \tag{5}$$

This value of U_{ok} can then be compared with the one obtained from radiosonde.

4. Analysis

Three periods — 0100—0140LT August 8, 1972 (Case I); 0215—0235LT, July 23, 1972 (Case II); and 0820—0850LT, July 23, 1972 (Case III) — were selected for detailed analysis. The facsimile records from each of the three sounders for each of the three cases are shown in Figs 2, 3, and 4. To determine the horizontal wave phase speed and direction of propagation of the waves revealed by the undulating strata of strong echo returns shown in Figs 2, 3, and 4, a simple time-lagged cross-correlation analysis between the intensity patterns of the strong echo return above the nocturnal inversion for the three sounders was performed. In general, the peak in the cross correlations does not occur at zero time lag, but is shifted in time. These shifts correspond to the travel time of a wave from one sounder to another. From this travel time both phase speed and direction of propagation can be derived (Briggs et al, 1950).

Figure 2 *Facsimile records from each of the sounders for 0000—0200LT August 8, 1972: Case I.*

The accuracy in the derived phase velocity depends on the accuracy with which the different travel times can be estimated. Since the pulse repetition frequency, which can be interpret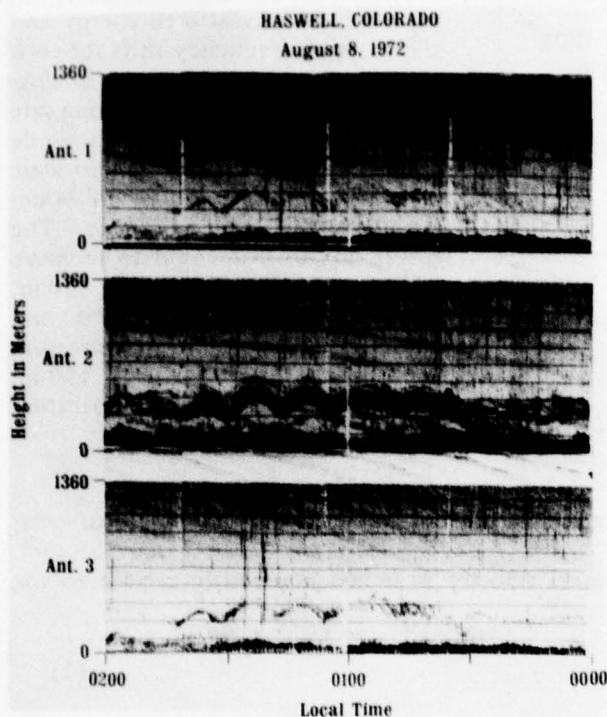ed as the sampling frequency, is 0.125 Hz in our case, the position in time of the peak of the cross correlation cannot be estimated more accurately than ±4 sec. This should give an accuracy in the calculated phase speed of the order of ±1 m sec^{-1} and approximately ±10° on direction for a wave travelling with a speed of 10 m sec^{-1} over the array. An increase in phase speed will increase the estimated errors. For Case I, Doppler data were used to estimate the wave-associated vertical-velocity fluctuations. For this purpose the echo returns from five vertical height intervals totalling about 11 m were time-averaged over 10 consecutive pulses (80 sec.). The vertical velocity resolution, assuming that the signal must be observed for 0.0588 sec. and that one-quarter of the period is needed to track the Doppler, was found to be ±0.1 m sec^{-1}.

Case I: 0100—0140LT August 8, 1972. In Case I (Fig. 2) we have an apparently stable undulating stratum of strong echo returns well separated from the nocturnal surface boundary-layer inversion below. The wave motion appears to be nearly sinusoidal, and the wave parameters for this time interval calculated from both the acoustic-echo-sounder array data and the microbarograph array data are shown in Table 2. Table 2 also gives the horizontal wave phase speed ω/k and propagation direction computed from tower data on the amplitude of the wave-associated pressure fluctuations p′ and horizontal velocity fluctuations $\vec{u}′$, (where prime denotes the wave-associated depar-

WAVE PARAMETERS	ACOUSTIC SOUNDER	MICROBAROGRAPH ARRAY	"IMPEDANCE" RELATION
PERIOD	715 sec	717 sec	
HORIZONTAL PHASE SPEED	7.5 m sec^{-1}	8.0 m sec^{-1}	7.7 m sec^{-1}
HORIZONTAL WAVELENGTH	5.4 km	5.7 km	
DIRECTION OF ARRIVAL	245°	220°	
AVERAGE HEIGHT OF THE WAVE	400 m		
AMPLITUDE OF THE WAVE	120 m		

Table 2 *Wave Parameters for the Events of Case I*
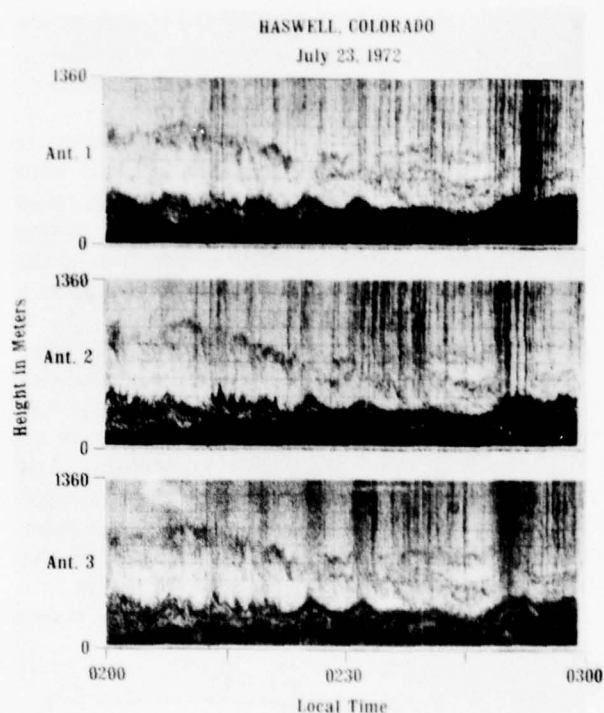
Figure 3 *Facsimile records from each of the sounders for 0200–0300LT July 23, 1972: Case II.*

ture from the background value k), using the "impedance relation" (Gossard and Munk, 1954)

$$\frac{\omega}{k} = \frac{p'(z)}{\rho_O(z)u'(z)} - U_{ok}(z) \quad (6)$$

No significant differences appear between the results obtained from the microbarograph array and the acoustic echo sounder array as far as wave period and horizontal phase speed are concerned; both give a period of about 715 seconds and a phase speed of about 8 m sec^{-1}. The difference in the observed direction of arrival is larger, about 25°; however, because the wavelength is an order of magnitude greater than the dimensions of the array, the direction determined is subject to uncertainties larger than ±10°.

The Doppler-derived vertical velocities for Case I are shown in Fig. 5. The lined portions indicate height–time intervals of positive (i e, upward) vertical velocity, while the dotted portions correspond to areas with negative (i e, downward) velocity. The heavy line is the zero vertical velocity boundary; the ±0.1 and ±0.3 m sec^{-1} contours are also shown. For clarity, the boundaries of the stratum of strong echo return (dotted lines) are also shown.

The Doppler derived vertical velocity for the descending portion of the wave between 0109 and 0115LT was found to average −0.25 m sec^{-1} with a maximum value of −0.35 m sec^{-1}. Between 0123 and 0129LT, the Doppler method gave about −0.35 m sec^{-1} with a maximum of −0.48 m sec^{-1}. This agreement is very good. The low signal-to-noise ratio precluded our deriving the vertical velocity for that part of

HASWELL, COLORADO
July 23, 1972

Figure 4 Facsimile records from each of the sounders for 0800–0900LT July 23, 1972: Case III.

the atmosphere between the stratum of strong echo returns and the nocturnal inversion below; therefore, we were unable to determine whether this part of the atmosphere was oscillating in phase with the wave motion above. However, by examining the vertical velocity fluctuations at the top of the nocturnal inversion, as shown at the bottom of Fig 5, we see that periods with significant upward vertical velocities correspond to the periods of upward vertical velocity inside the stratum of strong echo returns. The facsimile record in Fig 2 also gives evidence that the height of the nocturnal inversion is oscillating in phase with the wave motion.

Using the wave parameters shown in Table 2 together with Eq (5), we obtained a wind component of 6 m sec^{-1} along the propagation direction of the wave. The radiosonde gave a component of about 5.5 m sec^{-1}. Unfortunately, the radiosonde we used was released about two hours before the wave event. During the time between the radiosonde and the wave event, no significant changes in wind speed or direction were observed on the nearby tower. This may indicate that the radiosonde data were representative of values prevailing at the time of the event, at least in the first few hundred meters. Taking into account the difference in time between the radiosonde and the wave event, the agreement between the wind component measured by the radiosonde and the one calculated from acoustic sounder data is quite good. This appears to confirm the potential of acoustic echo sounder observations of boundary-layer gravity waves for measuring boundary-layer wind speeds.

Case II: 0200–0230LT July 23, 1972. In Case II (Fig 3) the wave is clearly within the nocturnal inversion. The wave parameters calculated both from the acoustic sounder and the microbarograph array are shown in Table 3.

WAVE PARAMETERS	ACOUSTIC SOUNDER ARRAY	MICROBAROGRAPH ARRAY
PERIOD	368 sec	365 sec
PHASE SPEED	9.7 m sec^{-1}	10 m sec^{-1}
WAVELENGTH	3.5 km	3.6 km
DIRECTION OF ARRIVAL	330°	322°
AMPLITUDE	~ 100 m	

Table 3   Wave Parameters for the Events in Case II
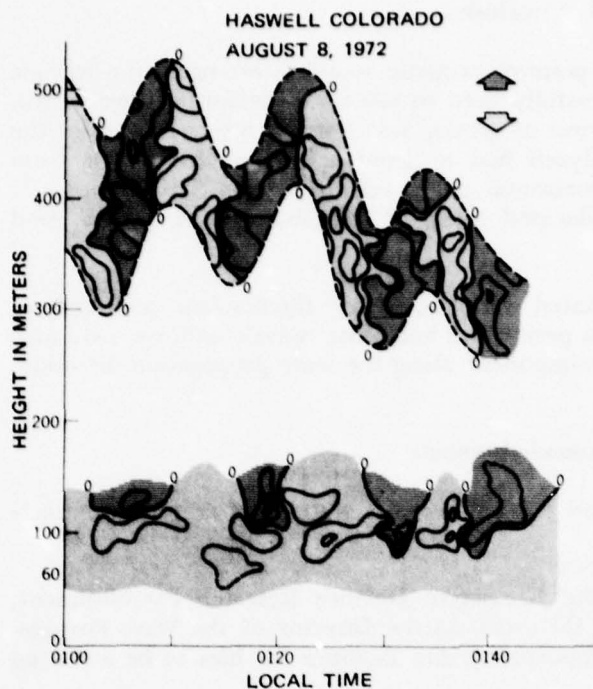
HASWELL COLORADO
AUGUST 8, 1972

Figure 5 Doppler-derived vertical velocities for the case shown in Figure 2.

The darker line-shaded portions indicate upward vertical velocity, while lighter dot-shaded portions correspond to areas with downward vertical velocity. The heavy line is the zero vertical velocity contour; the ± 0.1 and ± 0.3 m sec^{-1} contours are also shown.

The dotted lines are the boundaries of the stratum of strong echo return.

WAVE PARAMETERS	SOUNDER
PERIOD	205 sec
HORIZONTAL PHASE SPEED	5.2 m sec^{-1}
HORIZONTAL WAVELENGTH	1.1 km
DIRECTION OF ARRIVAL	278°
AMPLITUDE OF THE WAVE	~ 50 m

Table 4   Wave Parameters for the Events of Case III

As we see, an excellent agreement exists between the two systems. In this case the wavelength is much shorter, only about 3.5 km, which gives us better accuracy. In addition, even at only 250 m above ground the wave has a relatively large amplitude, giving us a good signal-to-noise ratio in the pressure fluctuations observed on the ground.

Case III: 0820—0845LT July 23, 1972. Case III (Fig 4) is a common morning situation in which the nocturnal inversion is eliminated when a convective layer develops with the onset of solar heating. The rising plumes within this convective layer appear to induce a wave structure at its top. There is some evidence of vertical wave phase variation, indicating a wave-associated vertical energy and momentum transport within the overlaying inversion. These wave parameters are shown in Table 4. For this event, we were only able to calculate the wave parameters from the acoustic sounder array; the wave was not detected by the microbarograph array. The reason for this can be seen from the gravity-wave dispersion equation which, in the Boussinesq and WKB approximations can be written as (e g, Hooke et al, 1973)

$$n^2 = k^2 \left(\frac{N^2}{\Omega^2} - 1 \right) \qquad (7)$$

where we have assumed that the wave-associated velocity and pressure perturbations vary as

$$\exp i(\Omega t - kx - nz)$$

and where $N^2 \equiv gd(\ln \theta)/dz$ is the square of the Brunt–Väisälä frequency N. Since for the most part the temperature structure within the convective planetary boundary layer is adiabatic, $N \doteq 0$, which implies from Eq (7) that $n = \pm ik$.

Thus we find that the wave amplitude at ground level is only a few per cent of what it is in the overlaying inversion; this causes it to be undetectable in the presence of the large pressure fluctuations associated with the thermal plumes.

5. Conclusion

We have shown that three vertically-pointing acoustic sounders arranged in a triangle about 300 m on a side can be successfully used to calculate horizontal wavelengths, phase velocities, and direction of arrival of gravity waves in the lower 1000 m of the atmosphere. The gravity waves analyzed had horizontal wavelengths ranging from about 1 km to almost 6 km with horizontal phase velocities from 5 to 10 m sec^{-1}. Comparing these results with a collocated array of microbarographs gave a good agreement.

Using estimates of the wave-associated vertical-velocity fluctuations and vertical displacements together with the wave period and horizontal wavelength, we were able to determine the mean wind speed component along the wave propagation direction.

Acknowledgements

References

Bean, B R: 1971, 'Comparisons of Remote and In-situ Measurements of Meteorological Parameters and Processes'. *Stat Meth and Instru in Geophys*, Ed A G Kjelaas, Teknologisk Forlag, Oslo, 1971.

Beran, D W, and Clifford, S F: 1972, 'Acoustic Doppler Measurements of the Total Wind Vector'. *Sec Symp on Meteor Obser and Instru*, San Diego.

Beran, D W, Hooke, W H, and Clifford, S F: 1973, 'Acoustic Echo Sounding Techniques and Their Application to Gravity-Wave, Turbulence, and Stability Studies'. *Bound Layer Meteor*, 4, 133–153.

Beran, D W, Little, C G, and Willmarth, B C: 1971, 'Acoustic Doppler Measurements of Vertical Velocities in the Atmosphere'. *Nature*, 23, March, 160–162.

Briggs, B H, Phillips, G S, and Shinn, D H: 1950, 'The Analysis of Observations on Spaced Receivers of Fading Radio Signals'. *Proc Phys Soc*, London B 63, 106–121.

Emmanuel, C B, Bean, B R, McAllister, L G, and Pollard, J R: 1972, 'Observations of Helmholtz Waves in the Lower Atmosphere with an Acoustic Sounder'. *J Atmos Sci*, 29, July, 886–892.

Gossard, E E, and Munk, W H: 1954, 'On Gravity Waves in the Atmosphere'. *J Meteor*, 11, 259–269.

Hooke, W H, Young, J M, and Beran, D W: 1972, 'Atmospheric Waves Observed in the Planetary Boundary Layer Using an Acoustic Sounder and a Microbarograph Array'. *Bound Layer Meteor*, 2, 371–380.

Hooke, W H, Hall, F F, Jr, and Gossard, E E: 1973, 'Observed Generation of an Atmospheric Gravity Wave by Shear Instability in the Mean Flow of the Planetary Boundary Layer'. *Bound Layer Meteor*, 5, 29–41.

Little, C G: 1969, 'Acoustic Methods for the Remote Probing of the Lower Atmosphere'. *Proc IEEE*, 57, 571–578.

McAllister, L G: 1968, 'Acoustic Sounding of the Lower Atmosphere'. *J Atmos Terr Phys*, 30, 1439–1440.

Monin, A S: 1962, 'Characteristics of the Scattering of Sound in a Turbulent Atmosphere'. *Akust Zh*, 7, 457–461 (Sov Phys – *Acoust* 7, 370–373).

Tatarski, V I: 1961, 'Wave Propagation in a Turbulent Medium'. *(R A Silverman, Transl)* New York, McGraw-Hill, 285 p.

Spectral Measurements and Atmospheric Stability

DAG T. GJESSI AND ANTON G. KJELAAS

Norwegian Defence Research Establishment, Kjeller

AND J. NORDØ

Norwegian Meteorological Institute

Spectral Measurements and Atmospheric Stability

Dag T. Gjessing and Anton G. Kjelaas

Norwegian Defence Research Establishment, Kjeller

and J. Nordø

Norwegian Meteorological Institute,

ABSTRACT

The influence of atmospheric stability on the vertical spectra of refractive index and air velocity is studied.

Spectra of refractive index and air velocity are deduced from beam-swinging experiments in the area between Norway and Denmark where a height interval from some 400 m to some 12 km is involved. These spectra are compared with the results of data obtained from radiosondes.

1. Introduction

During the last decade a number of experiments have been performed from which definite conclusions have been drawn regarding the shape of the refractive index fluctuation spectrum. Many of these results are in very poor agreement with the simple turbulence theory based on the Kolmogorov inertial subrange $k^{-5/3}$ law. Although it is probably fair to say that some of the earlier experiments had too few degrees of freedom to yield experimental results having a significant confidence level, others do have a confidence level sufficient to justify a more detailed examination of the findings. It is the purpose of this contribution to compare the results from simple straightforward radio experiments with results from conventional direct atmospheric soundings in the hope of finding a common denominator.

Specifically, we deduce the shape of the refractive index wavenumber and air velocity spectra from radio experiments and we compare these with data obtained by the use of conventional radiosondes.

2. The radio experiment

The radio data were obtained in a bistatic beam-swinging scatter experiment making use of one powerful transmitter and two sensitive receivers located far beyond the horizon relative to the transmitter. The experiment was performed in the geographical area between southern Norway (Kristiansand) and Denmark (Spodsbjerg near Copenhagen) probing the atmosphere in the height range from ~ 500 m to ~ 11 km.

Beam-swinging experiments are based on two theoretically obtained equations, the first of which is

$$P_R \propto \nu(x,y,z)\phi(\mathbf{K}), \qquad (1)$$

where P_R is the received scattered power, $\nu(x,y,z)$ the homogeneity function relating the degree to which the scattering ability (spectral density) varies with position (x,y,z) in space, and $\phi(\mathbf{K})$ the refractive index spectrum. The vector $\mathbf{K}$ is measured in the plane in which the scattering takes place such that $\mathbf{K}$ bisects the angle between the incident and the scattered wave having wavenumbers $\mathbf{k}_1$ and $\mathbf{k}_s$, respectively. Accordingly, $\mathbf{K}$ is given by

$$\mathbf{K} = \mathbf{k}_1 - \mathbf{k}_s, \quad \text{and} \quad |\mathbf{K}| = 2k \sin(\theta/2),$$

where θ is the scattering angle, $k = 2\pi/\lambda$, and λ the radio wavelength. For details see Gjessing (1962).

Whereas the first basic equation relates the time-averaged received power and the spatial distribution of refractive index, the second relates the frequency of the scattered radio waves and the atmospheric pattern of motion. Again referring to Gjessing (1962) for details, we have

$$\delta F = \frac{2}{\lambda}\left[V \sin\beta + \delta V(\gamma) \sin(\theta/2)\right]. \qquad (2)$$

where δF is the width of the received frequency spectrum (speed of fading), V the mean cross path component of the wind velocity, β the radio beam width, δV the fluctuating component in the direction γ (γ is essentially the direction of $\mathbf{K}$ relative to the vertical direction), and θ the scattering angle.

The objective of the current experimental investigation is to determine $\phi(\mathbf{K})$ for vertical $\mathbf{K}$ from (1) and to determine the vertical component of the fluctuating velocity δV_v from (2). This is achieved by two beam-swinging experiments (see Gjessing and Børresen, 1967).

In Experiment A the transmitter and receiver beams are elevated synchronously in the x, z great circle plane, thus keeping the direction of $\mathbf{K}$ constant and vertical, whereas $|\mathbf{K}|$ varies since θ varies (z is the vertical

coordinate whereas x is measured along the path). The received power and the width of the Doppler spectrum (fading spectrum) are measured. From this experiment we obtain $\phi(|\mathbf{K}|)$ from (1) for $\mathbf{K}$ vertical with the effect of the homogeneity function $\nu(z)$ superimposed (z being the vertical coordinate). Furthermore, from (2), we obtain the mean cross path wind velocity V and the fluctuating component of wind velocity δV along the vertical direction since $\mathbf{K}$ is vertical.

In Experiment B the beams are also swung synchronously in the x,z plane, but in this case in such a manner that the elevation angle of one of the antennas increases by the same amount that the elevation angle of the other decreases. Hence, the scattering angle, and thus $|\mathbf{K}|$ are constant. Note that the direction of $\mathbf{K}$ is changed through the small angle $\alpha_{max}-\alpha_{min}$ (some $3°$) only, whereas the position of the scattering volume is lowered and shifted toward the receiver (when the elevation angle of the receiver beam is increasing). For all practical purposes, therefore, dir $\mathbf{K}$ and $|\mathbf{K}|$ can be considered constant while x and z are varied. It is well known that the mean refractive index varies with height, while the properties are generally more constant in a horizontal plane. If the variation in ν [Eq. (1)] is negligible when x varies as in Experiment B, the results of this experiment can be used to compensate for the effect of atmospheric nonhomogeneity on Experiment A. By performing Experiment B in such a way that the scattering volume is shifted to either side of the midpath position, i.e., x is varied from $+\Delta x$ to $-\Delta x$, while z is varied twice between z_1 to z_2, one obtains a measure of the influence of x on ν from symmetry considerations.

Thus, from the two beam-swinging experiments, we obtain information on $\phi(\mathbf{K})$ for $\mathbf{K}$ vertical as well as on the vertical component of the fluctuating air velocity δV_v.

Before we proceed to consider the experimental results, the details of which are given in Gjessing and Børresen (1967), let us briefly discuss the radiosonde experiment.

3. The radiosonde experiment

Conventional radiosondes were used in connection with the beam-swinging experiments over a height interval from 500 m to some 11 km to obtain the mean vertical profiles of temperature, humidity, wind speed and wind direction.

4. Experimental results

As shown earlier, the two experiments give $\phi(\mathbf{K})$ for $\mathbf{K}$ vertical and the vertical component of the fluctuating air velocity δV_v. Fig. 1 shows the variability of the spectrum slope n which is the exponent in the law $\phi(K) \propto K^{-n}$. Note that the median value of n for the total ensemble is very close to $-11/3$ in accordance with what would be expected from theoretical arguments

when the assumption is made that we are dealing with the inertial subrange portion of the spectrum. In our experiment $|\mathbf{K}|$ was varied from $2\pi/1.5$ m to $2\pi/0.5$ m using the most distant receiver (Spodsbjerg) and from $2\pi/3.4$ m to $2\pi/0.7$ m using the Utrup receiver. Fig. 1 also shows that in the height range from 2200–11,000 m, the slope n is quite variable whereas this variability is far less pronounced in the height interval from 600–4700 m.

From meteorological considerations one would expect the degree to which the atmosphere is mixed to be larger in the lower height interval where ground friction should be of importance. It is reasonable, therefore, to expect the results from the spectral measurements to be in closer accord with the classical $-11/3$ law in this height interval than would the results from higher elevations where a significant vertical total stability generally prevails.

To demonstrate this property, a correlation analysis was performed. Specifically, the slope n was correlated with various atmospheric parameters such as the Richardson number Ri, the Väisälä-Brunt frequency ν^2 which is the numerator of Ri, and the Showalter index which is the difference in potential temperature between the 500- and the 850-mb surfaces. These atmospheric parameters were obtained from the conventional radiosonde data, the radiosonde being released so as to pass through the scattering volume of the 200-mi Kristiansand-Spodsbjerg path generally at, or close to, the time when the beam-swinging experiments were performed. Since the radiosonde (conventional U. S. Weather Bureau type) measures the pertinent parameters at discrete height levels, all data obtained at each height were fed into a digital computer (CDC 3600) for further processing. It was found that the Richardson number, in general, was quite variable, drastic changes being generally observed from one height interval to the next as a result of very small but variable vertical wind shears dv/dz which appear in the denominator of the expression for Ri, i.e.,

$$\mathrm{Ri} = \frac{\dfrac{g}{T}\left(\dfrac{dT}{dz} + \dfrac{g}{c_p}\right)}{\left(\dfrac{dv}{dz}\right)^2}.$$

Here g is the gravitational constant, T the mean temperature (for the pertinent height interval) and c_p the specific heat at constant pressure.

The beam-swinging experiment measures the average value of the $\phi(K)$ function in the height interval from 2200–11,000 m (in the case of the Spodsbjerg results). Thus, we get one average value of the exponent n for this height interval. As a result, in order to correlate n with appropriate atmospheric stability parameters, the average value of each such parameter must be com-
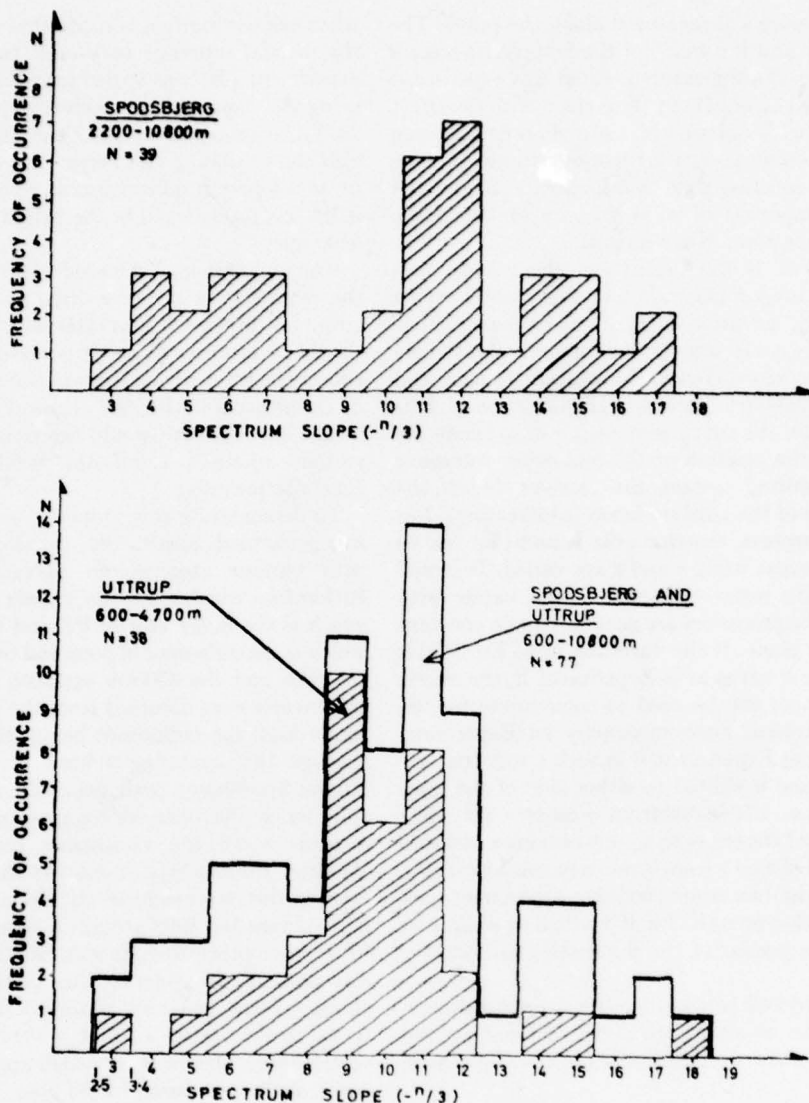
FIG. 1. Histogram of the distribution of $-n$, the exponent in the relation $\phi(K) \propto K^{-n}$, as obtained at two receiving stations some 100 and 200 mi, respectively, from the transmitter. The heavy line is the consolidated results from both stations.

puted for each balloon sounding. Since $Ri \to \infty$ as $dv/dz \to 0$ and since a large number of radiosonde soundings showed height intervals where dv/dz was virtually zero, Richardson's number, as applied, cannot be expected to be a convenient parameter for the correlation analysis.

By using a modified version of Ri, however, where the influence of $(dv/dz)^2$ on Ri was very much reduced, the dynamic term dv/dz did contribute to the correlation between n and the modified stability parameter, but as it was almost negligible it was omitted for the sake of simplicity from the final multiple regression analysis.

The analysis thus involved the new parameter

$$\nu_1^2 = \frac{g}{T}\left(\frac{dT}{dz} + \frac{g}{c_p} + 0.05\,T_{800}\right),$$

where ν_1^2 is a modified version of the Väisälä-Brunt frequency, T the average temperature in the pertinent height interval (from 2.2–11 km for the Spodsbjerg results), dT/dz the corresponding average temperature gradient, and T_{800} the temperature at the 800-mb surface.

Fig. 2 shows the result of the correlation analysis between $-n$ and ν_1^2. Note that the correlation coeffi-

SLOPE OF SPECTRUM $(\emptyset(K) \sim K^{-n})$

CORRELATION COEFFICIENT
R = 0·83
t = 9·79

$$\nu^2 = \frac{q}{T}\left[\frac{dT}{dz} + 0·05\ T_{800}° + \frac{g}{C_P}\right]$$

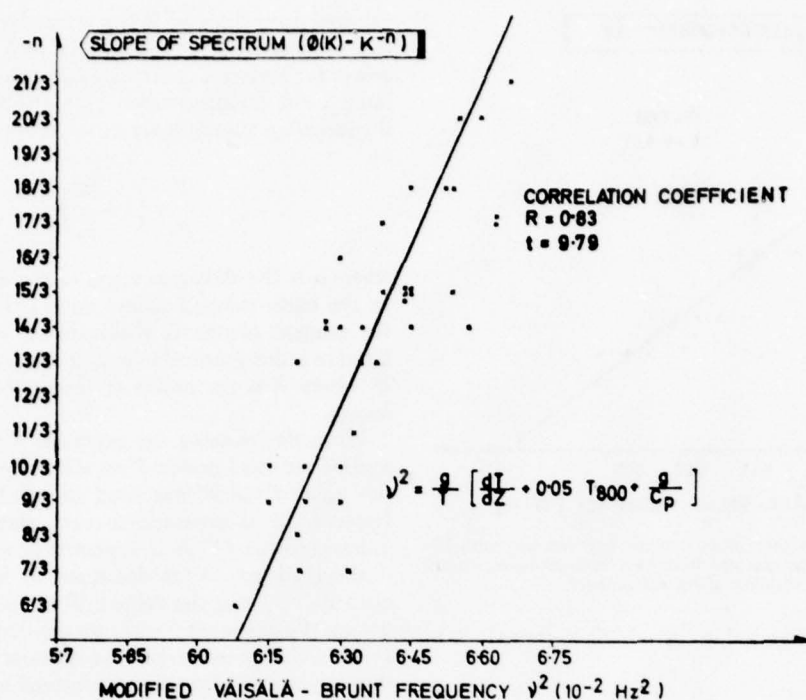MODIFIED VÄISÄLÄ - BRUNT FREQUENCY ν^2 (10^{-2} Hz^2)

FIG. 2. Result of a correlation analysis between the spectrum slope $-n$ as deduced from the beam-swinging experiments and the static stability of the atmosphere.

cient is 0.83% for 37 ensemble pairs. Note also that all the data obtained at the Spodsbjerg station are included except for cases where severe radio ducting saturated the radio receiver, making a beam-swinging experiment meaningless.

Checking the significance of the 0.83 correlation coefficient using the "student's t test," one finds that the probability of obtaining a correlation coefficient of 0.83 from a sample of 37 by pure chance is 1 in 10^6 ($t=9.79$). Our 0.83 correlation coefficient is thus considered as highly significant.

The correlation analysis was repeated on the basis of the Utrup results (height interval from 0.6–4.7 km). For this ensemble of experimental results, however, no significant correlation was observed. There are two obvious practical reasons for this. From an inspection of the histograms of Fig. 1, we first see that the variability (width of histogram) of the spectrum slope n is much smaller for the Utrup results as compared with those from Spodsbjerg. This has a direct influence on the correlation coefficient; indeed, a very small variability of one of the parameters involved in a two-parameter correlation analysis makes such an analysis meaningless. Secondly, in measuring the vertical profile of temperature through the scattering volume it was observed that in the lower part of the height interval involved in the Utrup experiments the temperature gradient dT/dz varied substantially with height. Since we require a mean value of this gradient, this strong

height dependence of dT/dz made it difficult to obtain a representative average profile.

In this brief presentation of the results, the dynamical aspects related to the experimental findings will not be discussed. We now consider another correlation analysis based on the beam-swinging data and on the modified Väisälä-Brunt frequency stability parameter ν_1^2.

From Eq. (2) we see that the slope of the N (speed of fading δF) vs θ curve resulting from measurement of the Doppler spectrum width δF as the scattering angle θ is varied in such a way (Experiment A) as to keep the direction of $\mathbf{K}$ vertical (i.e., $\gamma = 0$), gives us information about the quantity δV_v, the vertical component of the fluctuating air velocity. However, since δV_v can be determined uniquely from this experiment alone only when δV_v is independent of height, we select the cases where Experiment B indicates a homogeneous atmosphere from the point of view of wind motion, i.e., where the speed of fading δF is constant with height. (See Figs. 5 and 6 of Gjessing and Børresen.)

The ensemble of beam-swinging results thus obtained was used as the basis for the correlation analysis between the $\Delta N/\Delta\theta$, which is proportional to δV_v, and the stability parameter ν_1^2, the results being given in Fig. 3. We see that the correlation coefficient is 0.91 and that large values of the vertical fluctuating air velocity δV_v are associated with small values of stability, and conversely, that small values of δV_v are
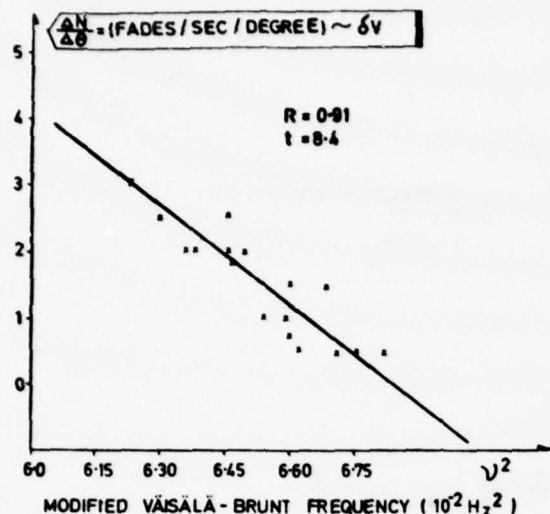
FIG. 3. Result of a correlation analysis between the spread in vertical air velocity as deduced from two beam-swinging experiments and the static stability of the atmosphere.

associated with large values of ν_1^2. This, indeed, is to be expected.

5. Discussion

Having presented the experimental results and having discussed some of the important experimental (engineering) limitation and sources of error, we now consider the manner in which the experimental results are related to the dynamics of the atmosphere.

Referring to Fig. 1, we observe a large variability of the refractive index spectrum slope in the height interval from 2200–11,000 m. Bearing in mind that the $\phi(K)$ spectrum is probed in the wavenumber region from $2\pi/1.5$ m to $2\pi/0.5$ m where the inertial subrange $K^{-11/3}$ law is expected to prevail, this variability is somewhat unexpected. However, if we compare the current results with those obtained using an entirely different technique (Eklund *et al.* 1968; Bolgiano, 1960), we find striking agreement insofar as the variability of the spectrum slope is concerned. Nevertheless, in spite of this experimental support, a critical evaluation of our experimental findings appears to be in order. In particular, it is of interest to know whether the static stability of the atmosphere really does have an effect on the refractive index spectrum (turbulence spectrum) in what is considered as being the high wavenumber end of the spectrum, or if the observed correlation (Fig. 2) is merely a result of the manner in which the shape of the refractive index spectrum is deduced.

We have already observed that the influence of the change in position of the scattering volume has been taken into consideration. What remains to be discussed is the theoretical expression with which the experimental curves are compared in order to obtain a measure of

the spectrum slope n. If the refractive index spectrum can be written in the form $\phi(K) \propto K^{-n}$, the received power for a given scattering angle relative to the maximum value obtained when both the transmitting and the receiving antennas are directed horizontally is given by

$$\frac{P}{P_0} = \left(1 + \frac{2\alpha}{\theta_0}\right)^{-n},$$

where α is the elevation angle of the antennas referred to the earth tangent planes and θ_0 the angle between the tangent planes. If there are no vertical mean refractive index gradients causing refraction, then $\theta_0 = d/R$, where R is the radius of the earth and d the path length.

When determining the exponent n from the experimental received power P vs elevation angle α curves, the value $\theta_0 = d/R$ was used for all the experiments. However, θ_0 is expected to vary since the refractive index gradient dN/dz is expected to vary; specifically, if the gradient dN/dz decreases, θ_0 increases. Consequently, by using the value d/R instead of θ_0 when deducing the exponent $|-n|$, we are deducing a value of $|-n|$ which is too large. The question now is whether this can account for the encountered variability in $-n$ and also for the correlation established in Fig. 2.

Completing our line of argument, we see that if $|dN/dz|$ decreases $|dT/dz|$ must also decrease for a given constant humidity, although the humidity term is not included in the regression analysis shown in Fig. 2. Finally, bearing in mind that the Väisälä-Brunt frequency ν^2 is proportional to the difference in gradient between the adiabatic profile and the measured temperature profile, we see that if $|dT/dz|$ decreases in the stable range, ν^2 must increase. Consequently, on the basis of the above argument, refraction effects are expected to give the same general relationship between ν^2 and n as that observed in the correlation analysis of Fig. 2. As a result of these conclusions, additional analyses were made. The first involves the correlation between the gradient dN/dz as obtained from the radiosonde and the exponent n as deduced from beam-swinging experiments; no significant correlation coefficient resulted.

Secondly, the minimum scattering angle θ_0 was calculated from the known value of dN/dz for each set of beam-swinging experiments. Using this value of θ_0 and the experimental power vs elevation angle relationship, the exponent n was obtained. Finally, n was correlated against ν_1^2 as in Fig. 2. The results of this analysis can be summarized as follows:

1) The correlation coefficient was essentially the same as that obtained previously.

2) Points in Fig. 2 corresponding to high values of $|-n|$ were shifted slightly down the $-n$ axis whereas

points corresponding to low values of $|-n|$ remained essentially fixed.

In conclusion, therefore, it is highly probable that the slope n of refractive index spectrum is affected by the static stability parameter ν_1^2.

If we now inspect the particular form of the current stability parameter ν_1^2, we see that the temperature at the 800-mb surface is involved. Excluding this from the correlation analysis, the correlation coefficient drops from 0.83 to 0.68; we thus see that this parameter is of considerable importance. The question which now arises is whether this T_{800} term constitutes a weighting of the density term g/T such that the stability parameter should be of the form

$$\nu_1^2 = \frac{g}{T + cT_{800}}\left(\frac{dT}{dz} + \frac{g}{c_p}\right),$$

where c is a weighting constant, or if T_{800} is, in fact, a weighting term on the restoring force $(dT/dz + g/c_p)$. This problem is in the process of being investigated.

We now consider the correlation analysis, the results of which are presented in Fig. 3. We see that when the contribution to fading of the vertical fluctuating component of the air velocity is plotted against ν_1^2, a correlation coefficient of 0.91 results. In this context it should be born in mind that δV_v, as deduced from the beam-swinging experiments, measures the variability in the vertical speed of the scattering elements at essentially one given instant. What Fig. 3 tells us, therefore, is that the velocity distribution of the scattering elements becomes narrower as the static stability parameter increases (Gjessing, 1962).

This indeed is to be expected; if the stability is sufficiently high one would expect the scattering elements in a limited spatial region to oscillate vertically in unison, the frequency of oscillation being the Väisälä-Brunt frequency ν^2. Under such conditions one would expect δV_v to approach zero as the spatial region responsible for the scattering is limited.

The fact that we are indeed obtaining a clear correlation between the modified Väisälä-Brunt frequency ν_1^2 and δV_v adds substantially to the confidence level of the $-n$ vs ν_1^2 correlation analysis of Fig. 2. Our confidence in ν_1^2 as a stability parameter, and not merely as a refraction parameter, is improved.

Accepting then, on the basis of the above arguments, that we have established a close relationship between the spectrum slope and the atmospheric stability, the question which arises is how it is possible for the static stability to affect the spectrum slope in a wavenumber region which is expected to fall within the inertial subrange.

Several authors (Bean *et al.*, Kaimal and Haugen, 1967; Panofsky and McCormick, 1960; Panofsky, 1968) have discussed the shape of the low wavenumber end of the spectrum in relation to atmospheric stability and in relation to height above the ground. These contributions, however, do not appear to have any bearing on the high wavenumber end of the spectrum such as we are currently investigating at large distances above the ground. Based on a multi-frequency radio experiment, however, Bolgiano (1960) has observed a variability of the n exponent (from $-6/3$ to $-18/3$) very similar to that encountered in the current experiment. Furthermore, in correlating the exponent n with a dynamic stability parameter (Richardson's number), he obtains a correlation coefficient of 0.80 from a 20-point sample and concludes that there seems to be a strong connection between the viscous cutoff scale and the dynamic stability of the atmosphere.

In this contribution we shall refrain from offering an explanation pertaining to the relationship established between spectrum slope and atmospheric stability; it is the hope that this, in due course, will be given.

6. Conclusions

These conclusions can be summarized as follows. Expressing the static stability of the atmosphere by a modified version of the familiar Väisälä-Brunt frequency ν^2, it is found that both the slope of the refractive index spectrum and the velocity spread of the irregularities (scatterers) causing scattering of radio waves are strongly influenced by the static stability. The fact that the width of the velocity distribution (as determined from a radio experiment) is so well correlated with our stability parameter (correlation coefficient 0.91) is comforting. As has been shown, we have laboriously examined a variety of phenomena that conceivably could influence our interpretation of the experimental results. On the basis of these examinations the conclusion can be drawn that the stability is indeed probably influencing the shape of the refractive index spectrum, and hence the turbulence field. It is unlikely, that the variability of the spectrum slope is determined by refraction effects. The confidence in this statement is very much increased by the fact that there is a strong correlation between stability, as defined, and the degree of irregularity of the air motion.

What remains then is to introduce arguments based on turbulence theory with the aim of explaining the relationships established in this paper; this, however, will be the topic of future work.

REFERENCES

Bean, B. R., C. B. Emmanuel and R. W. Krinks, 1967: Some spectral characteristics of the radio refractivity in the surface layer of the atmosphere. *Radio Sci.*, 2, 503–510.

Bolgiano, Ralph, jr., 1960: A theory of wavelength dependence in ultrahigh frequency transhorizon propagation based on meteorological considerations. *J. Res. NBS*, 64D, 231–237.

Eklund, Folke, and Sture Wickerts, 1968: Wavelength dependence of microwave propagation far beyond the radio horizon. *Radio Sci.*, 3, 1066–1074.

Gjessing, D., 1962: Determination of permittivity variations in the troposphere by scatter-propagation methods. *Proc. Inst. Elec. Engrs.* (*London*), C109, 447–456.

——, and J. A. Børresen, 1967: Beamswinging and supplementary experiments. *Proc. NATO Adv. Study Institute*, Wales, 1–35.

Kaimal, J. C., and D. A. Haugen, 1967: Characteristics of vertical velocity fluctuations observed on a 430 m tower. *Quart. J. Roy. Meteor. Soc.*, 93, 305–317.

Panofsky, H. A., 1968: The structure constant of the index of refraction in relation to the gradient of index of refraction in the surface layer. *J. Geophys. Res.*, 73, 6047–6049.

——, and R. A. McCormick, 1960: Spectra of wind velocity near the ground. *Quart. J. Roy. Meteor. Soc.*, 86, 495–503.

SMALL-SCALE ATMOSPHERIC STRUCTURE DEDUCED
FROM MEASUREMENTS OF TEMPERATURE,
HUMIDITY AND REFRACTIVE INDEX

D. T. GJESSING, A. G. KJELAAS

Norwegian Defence Research Establishment, Kjeller, Norway

and

E. GOLTON

Radio and Space Research Station, Ditton Park, Slough, England

Abstract. Measurements have been made with fast-response multi-channel temperature, humidity and refractive index sensors flown to 2000 m on a tethered balloon to investigate small-scale fluctuations important in radio-wave scattering, their relation to atmospheric parameters, and their spatial variation in both one and three dimensions. Data from the three types of sensors at one point were consistent for frequencies up to about 8 Hz. Power spectra of data at various heights were computed over 0.1 to 10 Hz and generally showed slopes (on a log-log plot) close to $-5/3$ above 1 Hz but ranged from -1.5 to -3.5 at lower frequencies; in this range ($f < 1$ Hz) slopes were close to $-5/3$ for negative Richardson number (Ri), provided temperature gradients were steeper than $-1.1\,°C\,100\,m^{-1}$ and wind shears $> 1.4 \times 10^{-2}\,s^{-1}$ approx. Steeper slopes were generally associated with stable atmospheric conditions but no precise relation to the above parameters was found. Spectral density was a maximum for Ri ~ -0.75.

Cross-correlations of 0.5 were frequently observed between sensors 1 m apart in orthogonal *directions*; in the vertical, examples of negative correlation of vapour pressure were occasionally found over this spacing. Using four sensors spaced in line over 9 m, cross-spectrum phase calculations of drift speeds were found to be consistent with measured wind speeds. The ratio of 'identification distance' (coherence $= 0.6$) to scale size of irregularities ranged from 0.25 to 0.5 with no apparent relation to height or meteorological parameters.

1. Introduction

This paper describes measurements of temperature, humidity and refractive index fluctuations in the troposphere, using fast-response instruments flown on a tethered balloon, which have been made with the object of studying small-scale structure which affects radiowave propagation. The scattering of radio waves in the troposphere depends on the variation, in space and time, of the radio refractive index; the presence of small-scale variations of refractive index, important in this scattering process, results from small-scale fluctuations of temperature and humidity.

Radio scattering experiments designed to measure the three-dimensional spatial spectrum of refractive index variations in the troposphere show that the spectrum varies substantially with the dynamic stability of the troposphere (Gjessing *et al.*, 1969). It is found that whereas the classical Obukhov-Kolmogorov theory predicts a wave-number power spectrum in the inertial subrange of the form $E(k) \sim k^{-n}$ with $n = 5/3$, radio experiments, and indeed direct measurements in the troposphere, show

that *n* may vary from 1 to about 3. Moreover, it is still not clear to what extent the fluctuation characteristics (scale size, spectral slope) of one parameter – for example, humidity – can be predicted from measurements of another parameter. A knowledge of the *instantaneous* small-scale spatial structure is also important. To study these features, a spaced-probe array consisting of a multi-channel refractometer with temperature and humidity sensors attached was flown on a tethered balloon at heights up to 2000 m. The spatial arrangement of the sensors could be varied, and different patterns were used to suit particular objectives. These were primarily to investigate the relation between refractive index, humidity and temperature fluctuations at one point; to measure spatial variations in three dimensions, and to measure the correlation between sensors spaced in one horizontal line. The measurements were made during July and August 1969 in anticyclonic conditions, giving stable and near-neutral lapse rates and low wind speeds. Under these conditions, fluctuations were often small and intermittent. In the following sections, significant and unusual results from an analysis of the various data are described.

2. Experimental Procedure

The experiments were carried out using the tethered balloon facility at Cardington, Bedfordshire, U.K. where it was possible to fly instruments at heights up to 2000 m. The equipment consisted of an X-band microwave refractometer, fine-wire thermometers, fast-response humidity sensors, a cup anemometer and a radio telemetry system. The refractometer had four open sampling cavities and a closed reference cavity in the swept-frequency Birnbaum system (Birnbaum, 1959), and was developed from an earlier model described by Fowler *et al.* (1966). It has a frequency response of 0 to 20 Hz (3-dB point). The temperature sensors were made from $10\text{-}\mu$ platinum wire and were used in a resistance-thermometer circuit, giving a response to 80 Hz. The humidity sensors were of the coated quartz-crystal type capable of giving fast response, to 25 Hz approximately. Both the temperature and humidity sensors have been described in detail by Gjessing *et al.* (1968).

One each of the thermometers and humidity sensors was placed close to a refractometer cavity so that consistent fluctuation measurements might be expected up to some 20 Hz at normal wind speeds. Three different arrangements of the sensor groups were used; these were, firstly, an orthogonal array with one group of sensors at the origin and one on each axis at equal distances of 1 m; secondly, the sensor groups were placed in line on a 9-m boom, flown so as to be in line with the mean wind as determined by a wind sock attached to the end of the boom. The spacings were in order 1.5, 4.4, 3.2 m, which gave six different spacings between pairs for spatial correlation measurements. The third arrangement had sensors placed on a 4.5-m boom cross-wind, with spacings of 0.75, 2.3 and 1.5 m.

The data were telemetered to the ground using a standard IRIG multiplex FM subcarrier system modulating a 1500-MHz FM transmitter. The multiplex was recorded on magnetic tape and analog signals were recorded on paper charts.

The data were analysed by standard digital computer techniques; selected data were digitised at 40 samples per second after the signals had been filtered to the required bandwidth; using the methods of Blackman and Tukey (1958) the auto- and cross-correlations of the signals were calculated, together with power spectra $S(f)$ and cross-spectral properties. These included co-spectra (P_{12}) and quadrature spectra (Q_{12}), coherence $COH_{12} = (P_{12}^2 + Q_{12}^2)/S_1 S_2$, i.e., the normalised magnitude squared of the cross-spectrum between channels 1 and 2, and the associated phase shift $\theta_{12} = \tan^{-1} Q_{12}/P_{12}$. Prewhitening and recolouring processes were used in computing spectra. Digital filtering techniques were also used to remove dc and low frequency components which can give rise to errors in analysis, and to eliminate high frequencies and reduce the number of data points when studying low-frequency components.

3. Sensor Performance

The first point of interest is to compare the fluctuations measured simultaneously by each type of sensor at one location and to see if they are consistent. Figure 1 shows such fluctuations at each of four locations and illustrates the mutual consistency of the recorded data. These were recorded at 1500-m height with the 9-m in-line array and show small fluctuations and occasional large changes, intermittency typical of stable conditions; the cross-correlations between sensors of the same type exceeded 0.95 for all channels.

In Figure 2a small-scale measured refractive-index fluctuations typical of more uniform turbulence near the ground are compared with those calculated from the humidity and temperature fluctuations; the agreement is clear and the cross-correlation is 0.92 over a 2-min sample. The correlation is thought to be limited mainly by non-linearity of the humidity sensors particularly at large relative humidity (Gjessing *et al.*, 1968). The calculated values were obtained using the equation

$$\delta N = \alpha \delta e + \beta \delta T, \tag{1}$$

where δe (mb) is the fluctuation in water vapour pressure and $\delta T(^\circ C)$ the fluctuation in temperature. This equation is obtained by differentiation of the Debye equation in the reduced form

$$N = \frac{77.6}{T}\left(P + \frac{4810\, e}{T}\right), \tag{2}$$

where N is one million times the amount by which the radio refractive index exceeds unity. P (mb) is the total pressure, T (K) is the temperature and e (mb) is the water vapour pressure (e.g., Bean and Dutton, 1966). Typically $\alpha \sim 4.5$ mb and $\beta \sim -1.2$ °C.

Figure 2b shows the power spectra to be similar to at least 6 Hz. The root coherence, representing the cross-correlation in each frequency band of the spectrum, is shown in Figure 2c and is greater than 0.7 up to some 6 Hz. The dip at 7 Hz is thought to
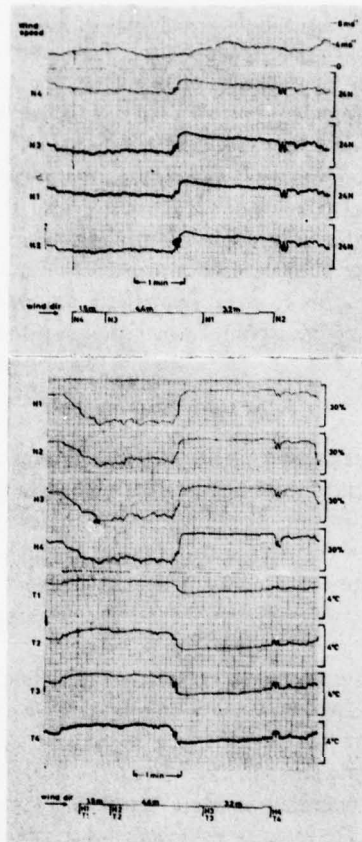
Fig. 1. Examples of refractivity N, relative humidity H and temperature T fluctuation, 9-m in-line array, 1500 m, 1969 July 30 at 1448.

be caused by a weak 7-Hz noise component present in the refractometer output. Above this frequency, the decrease in coherence may be due to fluctuations in wind direction, and to finite sensor spacings of about 20 cm. However, the general agreement between sensor measurements is considered acceptable.

4. Single-Point Measurements

Before considering the results from spaced-array measurements, much information can be deduced from the observations at one point in relation to atmospheric structure. Samples of atmospheric fluctuations were over periods of 5 to 10 min at heights up to 2000 m, often at 150-m intervals, and from these we have sought answers to our particular questions:
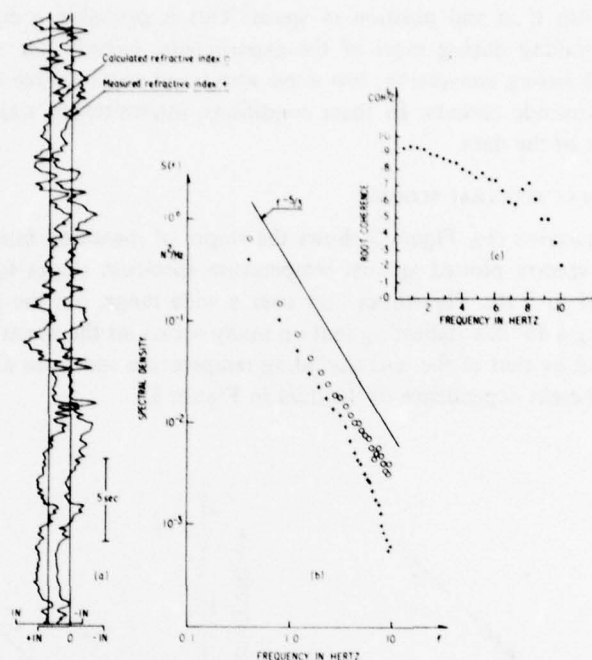
Fig. 2. (a) Comparison between measured refractivity fluctuation and that calculated from temperature and humidity fluctuations at one point. Test data 2 m above ground. – (b) Corresponding power spectra. – (c) Coherence between measured and calculated fluctuations.

(a) To what extent do the spectra $S(f)$ of the N, T and e fluctuations, as measured directly, vary with time and position?

(b) To what extent do the slopes n (on a log-log plot) of spectra $S(f) \alpha f^{-n}$ vary in unison?

(c) To what extent do the standard deviations σ_e, σ_T, σ_N correlate?

(d) To what extent do n and σ correlate with conventional parameters describing the stability of the atmosphere, such as the Richardson number Ri, temperature gradient dT/dz, and wind shear dV/dz?

4.1. VARIATION OF SPECTRA IN SPACE AND TIME

Typical e and T power spectra (e.g., Figure 8) show that the high-frequency end of the spectrum from 1 to 10 Hz nearly always follows a $-5/3$ power law irrespective of the position in space at which the measurements are made. This also applies to the N spectra since the fluctuations are linearly related. However, the N, e, T spectrum slopes are found to vary considerably for frequencies below some 1 Hz, usually being steeper than $-5/3$, and the frequency at which the spectrum slope changes varies with time and position in space. When reduced to scale size using the mean wind speed, this point varies over 1 to 10 m. The spectrum slopes are also found to vary

considerably with time and position in space. This is probably a consequence of
conditions prevailing during most of the experiments, namely fine weather often
associated with strong convection, low wind speed and some degree of layering as
shown by radiosonde ascents. In these conditions, intermittency was frequently a
marked feature of the data.

4.2. Variation of spectral slopes

In answer to question (b), Figure 3 shows the slopes of measured humidity and re-
fractive index spectra plotted against temperature spectrum slopes for frequencies
in the range 0.1 to 1 Hz. The slopes vary over a wide range, but the plotted points
tend to lie along a 45° line indicating that on many occasions the spectrum slopes are
well represented by that of the corresponding temperature spectrum alone. There is
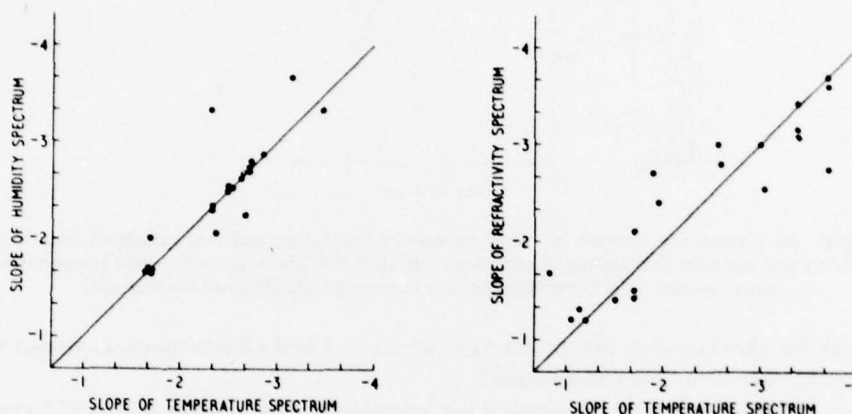no systematic height dependence of the data in Figure 3.

Fig. 3.   Slopes of measured humidity and refractive index spectra against temperature spectrum
slope in the range 0.1 to 1.0 Hz. Heights: 0 to 1500 m.

4.3. Correlation of standard deviations

There was some evidence of a weak correlation between the standard deviations
σ_T, σ_e but instrumental shortcomings prevented more positive conclusions from
being reached. This arises as follows. The contribution to σ is largely from the low
frequency end of the spectrum where the spectral density is large. Therefore in order
to get an accurate estimate of σ_e, one must know the calibration curve for the humidity
sensor very accurately over the whole range of humidities. Since this curve is non-
linear, with the slope increasing substantially with relative humidity (Gjessing *et al.*,
1968), small variations in the calibration during an experiment will have a large effect
on the $\sigma_e - \sigma_T$ correlation.

It is also of interest to examine the standard deviations of the three measured

parameters under conditions when the temperature and humidity contributions to refractive index fluctuations are of similar magnitude. On many occasions, particularly on the large scale, the humidity fluctuations dominate but some examples were obtained where the small-scale fluctuations, equivalent to frequencies greater than 0.1 Hz, fulfilled the former requirement. While these are related linearly (Equation (1)) their instantaneous relative magnitudes depend upon physical processes causing the fluctuations. If the parameters are considered as independent and passive, carried in the turbulent field, then σ_T and σ_e contribute randomly to σ_N; but if the fluctuations are related, the variances are correlated, and from Equation (1) we derive

$$\sigma_N^2 = \alpha^2 \sigma_e^2 + \beta^2 \sigma_T^2 + 2\alpha\beta C_{eT}, \tag{3}$$

where C_{eT} is the covariance; similarly in deriving spectra, the cospectrum must be included as has been done by Gossard (1960). Of the samples studied, generally of 2- to 5-min duration, in no case did T and e fluctuate in such a way as to cancel or greatly reduce their combined contribution to the variance of N. However this possibility in atmospheric data is not ruled out and can certainly occur in surface measurements, as indicated by the data of Swinbank and Dyer (1967) obtained under conditions of strong surface evaporation.

4.4. RELATION OF SPECTRAL SLOPE AND VARIANCE TO STABILITY PARAMETERS

To investigate the relation between N, e, T and the dynamic state of the troposphere, the Richardson number Ri, wind shear dV/dz and temperature gradient dT/dz were first evaluated using data from routine Balthum meteorological soundings and radiosondes which gave mean temperature and wind at 150-m intervals near the time of the observations. Then the average was taken of the parameters in the two height intervals above and below the point of observation before an attempt was made to relate these rather large-scale quantities to the spectral measurements. Of these data the wind shear was the most uncertain, but encouragement was given by some similarity between wind profiles at 6-h intervals, and the emergence of significant correlations parameters as shown below.

The relation between wave-number spectrum $S(k)$ for $k = 2\pi/3 \mathrm{m}^{-1}$ and Ri is shown in Figure 4. The spectral density peaks at Ri ~ -0.75 both for e and T and the curve is similar in shape to that found by Bean et al. (1967) obtained at larger wave numbers using tower data and attributed by them to convective mixing. For large positive Ri, the turbulence is damped by static stability and as Ri $= 0$ is approached, mixing in a region of small potential gradient produces little enhancement of scalar fluctuations. For increasing negative Ri, fluctuation intensity increases and the effect of thermals may be important. Note that in Figure 4 the peak corresponds to measurements taken at 8-m height and that the mean lapse rate from ground to 15 m was 2.8 °C 100 m^{-1}; however, there is no systematic height variation of the plotted points.

Plotting the slope n of the temperature spectrum at the lower frequencies, 0.1 to 1 Hz, against Ri as illustrated in Figure 5a, shows that n remains close to 5/3 for negative Ri. When Ri becomes positive, n increases substantially, varying somewhat
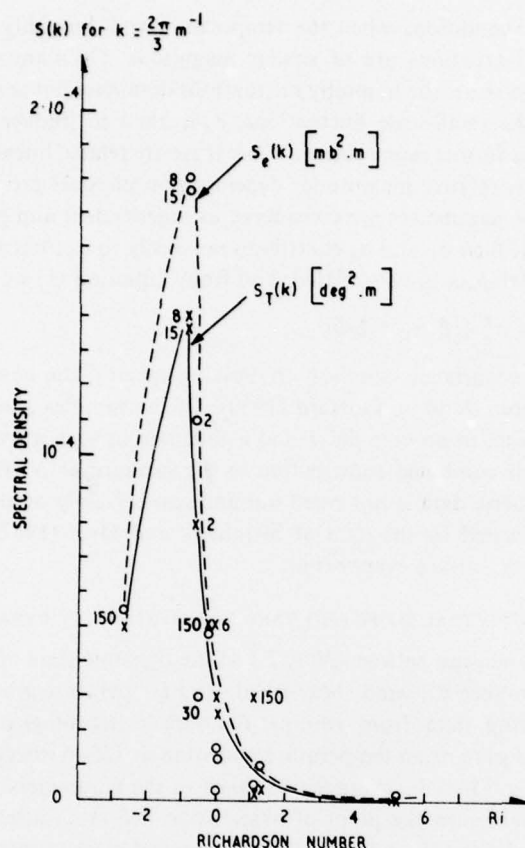
Fig. 4. Variation of spectral density of temperature and humidity fluctuations with Richardson number Ri at $k = 2\pi \, 3 \, m^{-1}$. Heights are shown in metres for larger densities. Smaller densities were measured between 30- and 1500-m height.

unsystematically between 2 and 3.5. It can be inferred therefore that large negative exponents in the spectrum power law are associated with stable atmospheric conditions, but no precise relationship between n and Ri can be deduced for such cases. Steep slopes were also found by Lane and Paltridge (1968, Figure 6) under low wind-speed conditions.

If instead, n is plotted against dT/dz, again for $f < 1$ Hz as shown in Figure 5b, it is found that n lies close to 5/3 for temperature gradients that are steeper than -1.1 °C $100 \, m^{-1}$, that is, slightly steeper than the adiabatic lapse rate. For smaller gradients, n varies unsystematically again between 2 and 3.5. The relation of n to wind shear follows a similar pattern, with $n \sim 5/3$ for shears greater than $1.4 \times 10^{-2} \, s^{-1}$ and with n variable under conditions of weak shear, in broad agreement with the conclusions of Bardeau and Mismé (1969) using radiosonde observations. These variations are
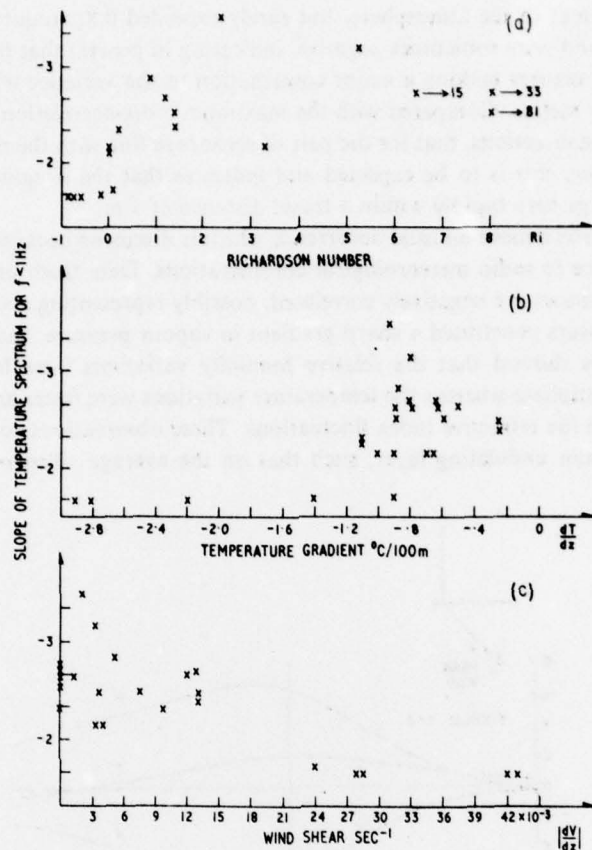
Fig. 5. Variation of slope of temperature spectrum ($f < 1$ Hz) with (a) Richardson number, (b) temperature gradient and (c) wind shear.

generally consistent with the behaviour of n with Ri and we may conclude that, to the extent that values of Ri, dT/dz, dV/dz averaged over 150 m are descriptive of the dynamic stability in the region of observation, they give an indication of the conditions under which $-5/3$ law turbulence exists.

An investigation of the behaviour of standard deviation and spectrum slope has failed to show any clear relation between the two, and this implies that spectral density plots $S(f)$ do not in general converge at either the low or high frequency ends of the spectrum.

5. Results from the Three-Dimensional Orthogonal Array

Time-lagged cross-correlations were calculated between pairs of sensors in the 1-m spacing array. In general the maximum correlations covered a wide range at different

heights and times in the atmosphere, but rarely exceeded 0.8; frequently they were less than 0.5 and were sometimes negative, indicating in general that the scale size of irregularity structures making a major contribution to the variance was often of the order of a few metres. Compared with the maximum cross-correlation in the vertical and cross-wind directions, that for the pair of sensors in line with the mean wind was generally larger; this is to be expected and indicates that the irregularity structure does not change very rapidly within a travel distance of 1 m.

Figure 6 shows a more unusual occurrence which is discussed because of its interest and importance to radio meteorological considerations. Data from the vertical pair of humidity sensors are negatively correlated, possibly representing a situation where one of the sensors penetrated a sharp gradient in vapour pressure. Inspection of the original charts showed that the relative humidity variations were large-scale and generally in antiphase whereas the temperature variations were faster and generally in phase, as were the refractive index fluctuations. These observations could have been caused by a thin undulating layer, such that on the average when one of the two
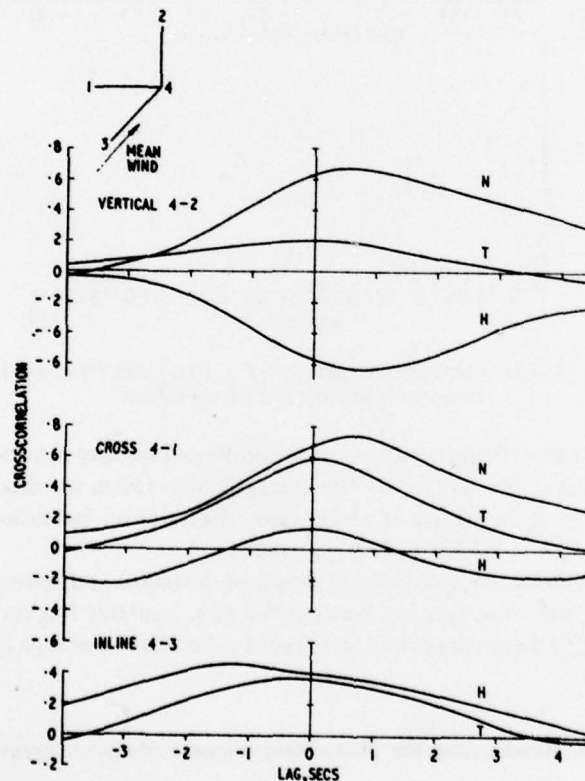

Fig. 6. Lagged cross correlations between pairs of sensors in a three-dimensional array, 1-m spacing, 900 m, 1969 July 18 at 1443.

vertically spaced sensors was inside the layer, the other was outside; it would be very desirable to have more information on the structure of the atmosphere to help explain these observations. However, of the available data, the mean wind shear and the temperature gradient averaged over 150-m intervals (used earlier) are of too large a scale to be very useful, while the records obtained from the balloon ascent with the equipment contain mixed height and time variations, apart from changes in the height of the fine atmospheric layer structure with time. The only general conclusion reached is that all cases of negative vertical vapour-pressure correlation occurred when the larger scale (150 m) parameter indicated stable atmospheric conditions. To obtain adequate information in the future to help explain this type of phenomenon, it would seem necessary to make measurements of wind and temperature at least at a number of points spaced vertically about the main instrumentation, perhaps spaced over some 50 m.

Figure 7 shows maximum cross-correlations between pairs of sensors in the three-dimensional array at various heights during one ascent. Two height regions where the vertical humidity sensors show negative correlation are evident, and although the various correlations cover a wide range, there is some systematic height variation in the data. If we apply Equation (1) to the sensors at each of two spaced points 1 and 2, and assume the coefficients α, β apply at both points, then the covariance C_N between refractometer cavities is given by:

$$C_N = \alpha^2 C_e + \beta^2 C_T + \alpha\beta(C_{e1T2} + C_{e2T1}), \tag{4}$$

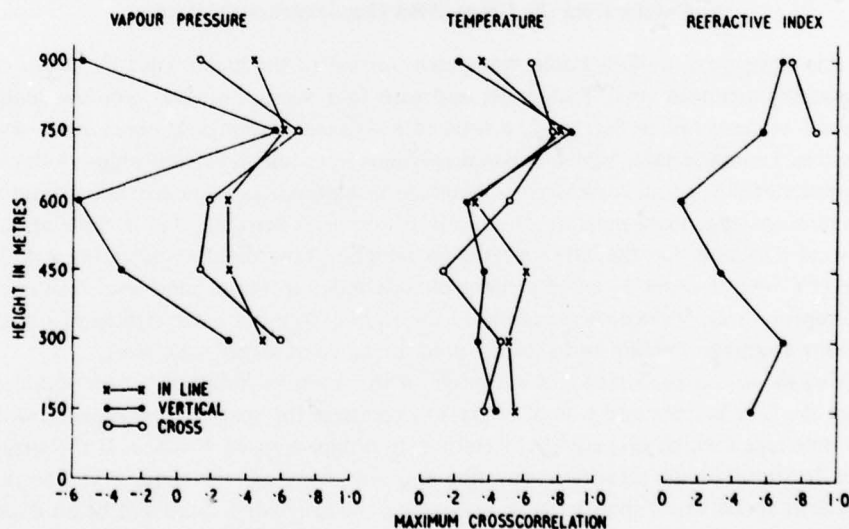where the C_{eT} are now crossed covariances between the humidity and temperature

Fig. 7. Maximum cross-correlations between pairs of sensors in a three-dimensional array, 1-m spacing, at various heights. 1969 July 18.

sensors. Replacing covariances by cross-correlations e.g., $C_e = \sigma_e^2 : CC_e$, etc., we obtain

$$\sigma_N^2 \cdot CC_N = C_N = \alpha^2 \sigma_e^2 CC_e + \beta^2 \sigma_T^2 CC_T + \alpha\beta\sigma_e\sigma_T (CC_{e1T2} + CC_{e2T1}) \quad (5)$$

This equation indicates that, within bounds determined by the relevant standard deviations, the correlations between sensor pairs can vary widely. In particular, for the data of Figure 6 the positive CC_N and negative CC_e are consistent for a range of negative CC_{eT} cross-correlations, but as the coefficients in Equation (5) involve the sensor calibrations which it has been explained are somewhat uncertain, a more precise comparison is not possible.

A study of the time lags for maximum cross-correlations between sensors indicates that the direction of general air movement through the array varied widely, often over $\pm 45°$ both in the vertical and horizontal, expecially under low wind conditions $(1-5 \text{ m s}^{-1})$. In particular, vertical velocity components of $\frac{1}{2}$ to 1 m s^{-1} over periods of minutes both upward and downward on different occasions were observed. It is thought that these movements are associated with rising thermal structure and the order of measured velocity agrees well with measurements of the ascent rate of large convective cells by sensitive radar methods (Ottersten, 1969). These movements are of some consequence in that it is common practice to make use of a mean wind speed v to convert frequency spectra $S(f)$ into wave-number spectra $S(k)$ by $k = 2\pi f/V$; a steady deviation of wind direction from that assumed could lead to errors of up to 50% in k. Also because of these movements a simple interpretation of the correlations in terms of characteristic blob shape and size does not seem easy and other interpretations are being sought.

6. Results from the Cross-Wind One-Dimensional Array

In this experiment a $4\frac{1}{2}$-m boom was flown normal to the mean wind by means of a specially arranged small parachute, and with four sensors of each type unequally spaced, as described in Section 2, a total of 6 different spacings between pairs was possible. From the data, lagged cross-correlations were calculated and Figure 8 shows examples of the spatial correlograms obtained using the maximum cross-correlations for each spacing; these maxima do not always occur at zero lag, due to fluctuations in wind direction. On the left (8 m), the correlogram falls rapidly, indicating a scale size $(CC = \frac{1}{2})$ of order $1\frac{1}{2}$ m near the ground, similar to the ground-level results of Thompson *et al.* (1968); the example to the right (150 m) is more typical of observations at greater heights and shows a predominance of larger scale sizes.

Also shown on each plot is the average of the 4 autocorrelation curves obtained from the four sensors and it is of interest to compare the spatial separations L with the time lags t which give equal correlation, to obtain a speed $V = L/t$. If the structure drifting past the sensors is isotropic and not changing with time, V will be the true drift speed, but if the structure is changing, the calculated speed will be an overestimate of the true velocity. Doing this computation for each point on the spatial correlograms, the speeds shown at the top of Figure 8 were obtained.
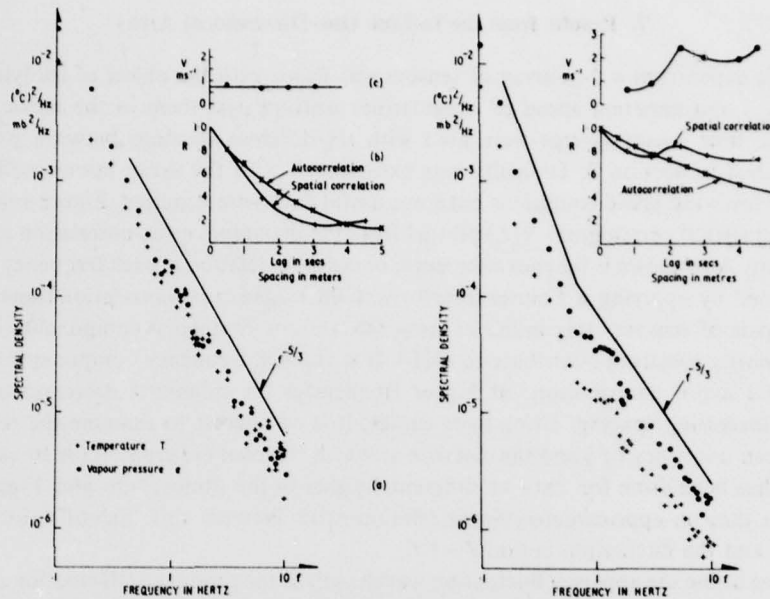
Fig. 8. (a) Typical examples of humidity and temperature spectra. – (b) Temperature auto and spatial correlograms. Cross-wind array 1969 August 1. – (c) Apparent wind speed derived from (b) using $V = L/t$ where $R(L) = R(t)$. – The left-hand curves correspond to 8-m height and the right-hand curves to 150-m height.

At 8 m above the ground for correlations greater than 0.2, the speeds obtained are nearly all equal with a mean of 0.75 m s^{-1} while records of the wind speed, measured with a cup anemometer showed a large variation ranging from 1 to 5 m s^{-1} with a mean of $1\frac{1}{2}$ m s^{-1}. Thus the agreement is poor, the correlation method under-estimating the mean speed, and could be caused by anisotropy or by a vertical wind. At 150 m calculated speeds are more scattered but with several about 2 m s^{-1}; the measured speed again varied greatly, from $1\frac{1}{2}$ to 5 m s^{-1} with a mean of $2\frac{1}{2}$ m s^{-1} giving more satisfactory agreement. It is clear that conditions of small and very variable wind speed are unsatisfactory for attempting measurements of spatial structure using spaced arrays of sensors, but unfortunately these conditions occurred frequently at the time of our field experiments.

Also shown in the lower part of Figure 8 are the corresponding spectra which were mentioned earlier. Of some 24 spectra from this series of measurements, all but 3 exhibited a $-5/3$ power law at frequencies above approximately 1 Hz, and at lower frequencies the slope was variable, except when measured close to the ground where it was again $-5/3$ (e.g., Figure 8); the steeper slopes were in all cases associated with large spatial correlation distances. This conclusion was also reached in the case of the three-dimensional array measurements. There was some evidence that the correlation distances of water vapour pressure were smaller than those of temperature.

7. Results from the In-Line One-Dimensional Array

In this experiment a 9-m array of sensors was flown with the object of studying the changes and apparent speed of irregularities drifting past them in the mean wind. Again, four sensor groups were used with six different spacings between pairs as described in Section 2. Difficulty was experienced with the array boom oscillating under low wind-speed conditions but some useful data were acquired. Figure 9 shows a typical spatial correlogram $R(L)$ plotted from the maximum cross-correlation at each spacing. Also shown is the root coherence, or cross-correlation in each frequency band, obtained by applying a Fourier transform to the lagged cross-correlation function of each pair of sensors; this indicates how the various frequency components in the irregularity spectrum contribute to $R(L)$. It is the low-frequency components which make a major contribution: at higher frequencies the coherence decreases rapidly with increasing spacing. Using these curves, it is of interest to examine the relation between frequency (f) and the distance at which the root coherence falls to say 0.6. This has been done for data at different heights in the atmosphere and Figure 10 shows that an approximately linear relation exists between this 'identification' distance and the fluctuation period $T = 1/f$.

If we define the apparent fluctuation wavelength as the product of fluctuation period and mean wind speed, the ratio, F, of identification distance to scale size can then be calculated from the mean slopes of Figure 10. These ratios are shown in the figure and range from 0.24 to 0.50 with no apparent relation to height or meteorological parameters. A similar calculation was made by Thompson et al. (1968) who obtained a ratio $F = 0.4$ for an array of sensors near ground level.
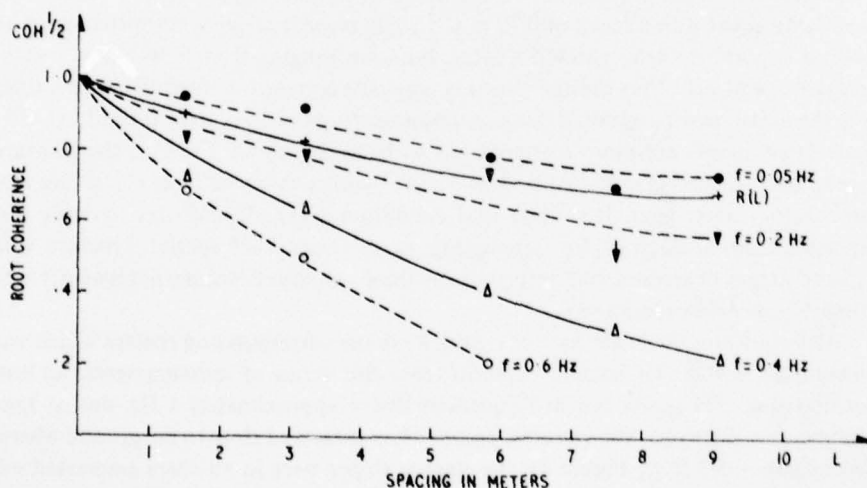

Fig. 9.   Spatial correlation $R(L)$ derived from maximum cross correlations between pairs of sensors, and the contribution from each frequency band (coherence). In-line array 300 m, 1969 July 30 at 1116, with humidity sensors.
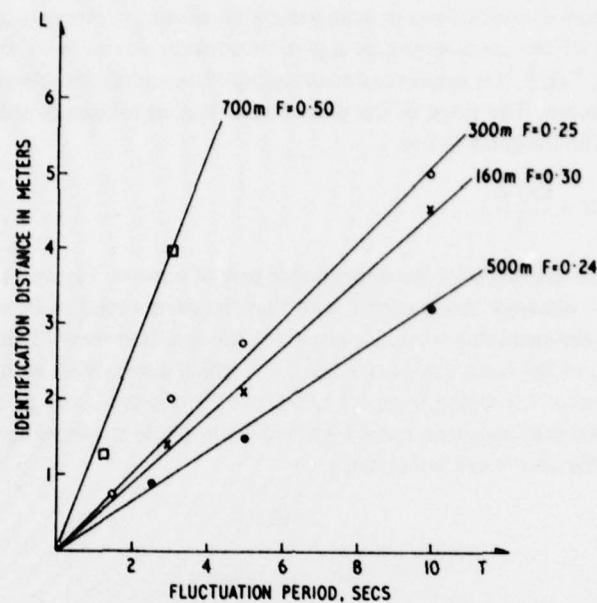
Fig. 10. Variation of identification distance, within which $\sqrt{COH} > 0.6$, with fluctuation period.
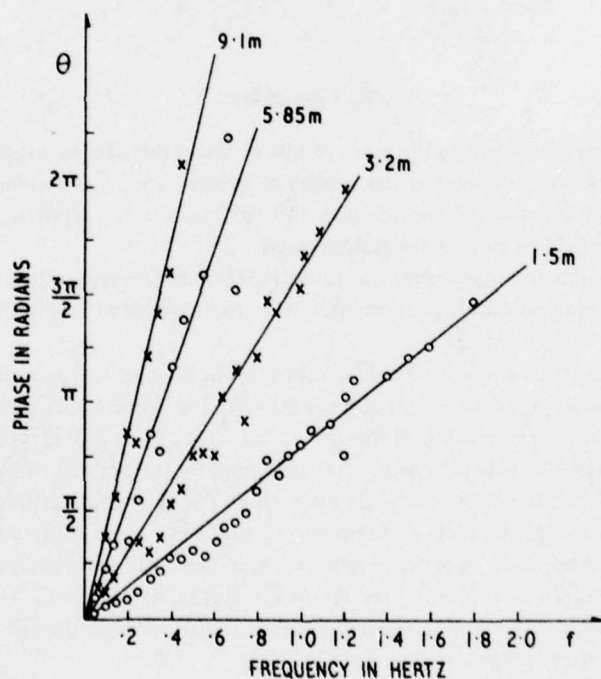

Fig. 11. Phase of cross-spectrum against frequency for various sensor spacings. Data as in Figure 9.

Another way in which one can examine the movement of irregularities is to plot the phase $\theta(f)$ of the cross-spectrum against frequency for each of the sensor pairs; since $\theta = \tan^{-1} Q/P$, it is subject to an ambiguity of $n\pi$ and this is selected so as to make $\theta(f)$ continuous. The slope of the plot should then be related to the apparent mean speed V of the irregularities as:

$$V = \frac{2\pi f\, d}{\theta},\tag{6}$$

where d is the separation of the appropriate pair of sensors. Figure 11 shows one such plot for four spacings and it can be seen that the points tend to lie on straight lines. Substituting the mean slopes into Equation (6), the speeds shown in Table I are obtained. The average of the four speeds is 3.78 m s^{-1} which agrees well with the mean wind speed of 3.5 m s^{-1}, ranging from 2.5 to 5.0 m s^{-1} measured with a cup anemometer. This indicates that apparent speeds derived from phase measurements give a useful measure of the true mean wind speed.

TABLE I

Apparent speeds derived from cross-spectral phase measurements

Spacing d (m)	1.5	3.2	5.75	9.1
Speed V (m s^{-1})	3.6	3.8	3.8	3.9

8. Conclusions

We conclude by summarizing the main results of this series of measurements, which in some cases confirm and extend the results of ground-level measurements to greater heights, and in other cases provide new information on atmospheric parameters of interest in the field of radiowave propagation.

(1) It is possible to compute the refractive index from fast-response temperature and humidity sensors and obtain agreement with refractive index measurements, to 10 Hz at least.

(2) Generally the slopes of refractive index, humidity and temperature spectra vary over a wide range (-1.5 to -3.5) at frequencies below some 1 Hz, and tend to vary in unison. At higher frequencies, slopes are often close to $-5/3$ as predicted by the theory of local isotropic turbulence, and occasionally steeper, up to -2.0.

(3) It is difficult to choose the scale over which parameters describing the dynamic state of the atmosphere such as temperature gradient, wind shear and Richardson number should be taken in order to relate them to fluctuations observed at one point. Averages over 150 m indicate that spectrum slopes are close to $-5/3$ when the Richardson number is negative, the temperature gradient steeper than $-1.1\,°\text{C}\,100\,\text{m}^{-1}$ and the wind shear greater than $1.4 \times 10^{-2}\,\text{s}^{-1}$.

Steep spectrum slopes are frequently associated with stable atmospheric conditions

but there is no precise relation between slope and the parameters mentioned above. Thus, under stable conditions the parameters cannot be used to indicate the nature of small-scale structure.

There is no apparent relation between spectrum slope and fluctuation intensity, but intensity reaches a maximum for a Richardson number of the order -0.75.

(4) Cross-correlation measurements with vertically-spaced sensors show that the atmosphere is sometimes composed of layers of order 1-m in thickness, which on occasion are more marked in vapour pressure than in temperature, and sometimes give rise to negative cross-correlations in vapour pressure.

(5) Well above ground the horizontal spatial correlation distances are often large and are associated with steep spectrum slopes at frequencies below some 1 Hz.

(6) The cross-correlations between sensors spaced along the mean wind direction are larger than for those set cross-wind, horizontally or vertically. Orthogonal array measurements indicate large and persistent fluctuations in wind direction which may be associated with thermals; this suggests taking caution in using mean wind speeds to derive wave numbers from frequencies in spectral applications.

(7) It is shown that, with cross-spectral techniques, irregularities can be used as tracers to obtain a measurement of the mean wind speed which agrees with direct measurements.

(8) The identification distance, defined as the distance within which the coherence of spaced sensor measurements is greater than 0.6, varies both in time and space. Also the ratio of identification distance to wavelength, given by the product of wind speed and fluctuation period, varies over a range from 0.25 to 0.5 in time and space and shows no simple relation to wind speed or other meteorological parameters.

Acknowledgements

References

Bardeau, H. and Mismé, P.: 1969, 'Pente de densité spectrale de la température en fonction de l'altitude entre 0 et 1500 m', *Compt. Rend Acad. Sci. Paris* **269**, 273.

Bean, B. R. and Dutton, E. J.: 1966, 'Radio Meteorology', *NBS Monograph* **92**, U.S. Dept. of Commerce, pp. 1–21.

Bean, B. R., Emmanuel, C. B., and Krinks, R. W.: 1967, 'Some Spectral Characteristics of the Radio Refractivity in the Surface Layer of the Atmosphere', *Radio Sci.* **2**, 503–510.

Birnbaum, G.: 1950, 'A Recording Microwave Refractometer', *Rev. Sci. Inst.* **21**, 169–198.

Blackman, R. B. and Tukey, J. W.: 1958, *The Measurement of Power Spectra*, Dover, New York.

Fowler, C. S., Champion, R. J. B., and Tyler, J. N.: 1966, 'A Three-Cavity Refractometer and Associated Telemetry Equipment', *Radio Elec. Eng.* **32**, 186.

Gjessing, D. T., Holm, C., Lanes, T., and Tangerud, A.: 1968, 'A Simple Instrument for the Measurement of Fine Scale Structure of Temperature and Humidity, and Hence also the Refractive Index, in the Troposphere', *J. Sci. Instr.* **1**, 107–112.

Gjessing, D. T., Kjelaas, A. G., and Nordø, J.: 1969, 'Spectral Measurements and Atmospheric Stability', *J. Atmospheric Sci.* **26**, 462–468.

Gossard, E. E.: 1960, 'Power Spectra of Temperature, Humidity and Refractive Index from Aircraft and Tethered Balloon Measurements', *IRE Trans. Ant. Prop.* **AP8**, 186–201.

Lane, J. A. and Paltridge, G. W.: 1968, 'Small-Scale variations of Radio Refractive Index in the Troposphere', *Proc. IEE London* **115**, 1227–1239.

Ottersten, H.: 1969, 'Atmospheric Structure and Radar Backscattering in Clear Air', *Radio Sci.* **4**, 1179–1193.

Swinbank, W. C. and Dyer, A. J.: 1967, 'An Experimental Study in Micro-Meteorology', *Quart. J. Roy. Meteorol. Soc.* **93**, 494–500.

Thompson, M. C., Kirkpatrick, A. W., and Grant, W. B.: 1968, 'Measurement of Radio Refractive Index Microstructure of the Near-Ground Atmosphere', *J. Geophys. Res.* **73**, 6425–6433.

Acknowledgement